

RICE UNIVERSITY

**Design, Characterization, and Validation of the  
OpenWrist Exoskeleton**

by

**Evan Pezent**

A THESIS SUBMITTED  
IN PARTIAL FULFILLMENT OF THE  
REQUIREMENTS FOR THE DEGREE

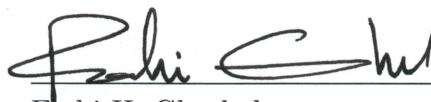
**Master of Science**

APPROVED, THESIS COMMITTEE:



---

Marcia K. O'Malley, Chair  
Professor of Mechanical Engineering



---

Fathi H. Ghorbel  
Professor of Mechanical Engineering



---

Lydia E. Kavvaki  
Professor of Computer Science

Houston, Texas

April, 2017

## ABSTRACT

Design, Characterization, and Validation of the OpenWrist Exoskeleton

by

Evan Pezent

Robotic devices have been clinically verified for use in long duration and high intensity rehabilitation needed for motor recovery after neurological injury. Targeted and coordinated hand and wrist therapy, often overlooked in rehabilitation robotics, is required to regain the ability to perform activities of daily living. To this end, a new coupled hand-wrist exoskeleton has been designed. This thesis details the design of the wrist module and several human-related considerations made to maximize its potential as a coordinated hand-wrist device. The serial wrist mechanism has been engineered to facilitate donning and doffing for impaired subjects and to insure compatibility with the hand module in virtual and assisted grasping tasks. Several other practical requirements have also been addressed, including device ergonomics, clinician-friendliness, and ambidextrous reconfigurability. The wrist module's capabilities as a rehabilitation training device are quantified experimentally in terms of functional workspace and dynamic properties. Finally, the device is validated as an rehabilitation assessment tool by considering its impact on commonly used assessment metrics. The presented wrist module's performance and operational considerations support its use in a wide range of future clinical investigations.

## Acknowledgments

I would like to begin by thanking my wonderful advisor Dr. Marcie O'Malley for being courageous enough to let a country boy from Alabama join the MAHI Lab. I could not have asked for a more knowledgeable and supportive advisor to guide me through this process (even when she's 4,600 miles away in Scotland). Of my fellow MAHI Lab members, undoubtedly Chad Rose has been the most instrumental to my success. Despite being a dirty Auburn graduate, Chad has shown no bounds in his willingness to help inside and outside of the lab. Janelle Clark, who joined in the same year as I, has grown to be much more than just a friend, but also the annoying sister I never had, providing a healthy sibling-like rivalry throughout our Master's program (beat you to it!). I also want to thank Andrew Erwin for collaborations on OpenWrist pointing tasks and general discussions about robotics, rehabilitation, and of course, sports. Dylan Losey, Craig McDonald, and Jenny Sullivan have answered more dumb questions from me than anyone deserves, and for that I am grateful. There is also Mikaela Juzswik and Claudia Kann, two of the sharpest undergraduates I've ever known, who played instrumental roles in the fabrication and experimentation of the OpenWrist, respectively. I would be remiss not to mention my parents and brothers, who have provided so much support over the years. Last, but definitely not least, I thank my beautiful wife and best friend, Krystin, for her constant love, devotion, support, encouragement, and understanding. Thank you for joining me on this journey and allowing me to pursue my dreams!

# Contents

Abstract	i
Acknowledgments	ii
List of Figures	v
List of Tables	xiv
<b>1 Introduction</b>	<b>1</b>
1.1 Background	1
1.2 Review of Upper-Extremity Rehabilitation Robots	2
1.3 Hand and Wrist Robotic Rehabilitation	3
1.4 Design Requirements for Hand-Wrist Rehabilitation Robots and READAPT	4
1.5 Characterization and Validation of Rehabilitation Robots	6
1.6 Thesis Outline	7
<b>2 Design</b>	<b>9</b>
2.1 Mechanical Design	9
2.1.1 Joint 1: Pronation/Supination	11
2.1.2 Joint 2: Flexion/Extension	12
2.1.3 Joint 3: Radial/Ulnar Deviation	13
2.1.4 Practical Considerations	14
2.2 Kinematic Structure	20
2.3 Dynamic Model	21
2.4 Mechatronics and Controls	23
2.5 Comparisons and Discussion	25

<b>3</b>	<b>Characterization as a Training Device</b>	<b>28</b>
3.1	Experimental Setup . . . . .	28
3.2	Step Input Experiment: Inertia, Viscous Damping, and Kinetic Friction	29
3.3	Ramp Input Experiment: Static Friction . . . . .	34
3.4	Schroeder Multisine Input Experiment: Closed-Loop Position Bandwidth . . . . .	36
3.5	Comparisons and Discussion . . . . .	37
<b>4</b>	<b>Validation as an Assessment Device</b>	<b>42</b>
4.1	Pilot Study: RiceWrist-S vs. OpenWrist in Wrist Pointing Velocity Profiles . . . . .	43
4.2	Subject Study A: Wrist Pointing Movements for Robot vs. No Robot Conditions . . . . .	45
4.2.1	Methods . . . . .	45
4.2.2	Results . . . . .	51
4.2.3	Discussion . . . . .	52
4.3	Subject Study B: The Effect of Robot Dynamics on Wrist Pointing Smoothness . . . . .	58
4.3.1	Methods . . . . .	58
4.3.2	Results . . . . .	63
4.3.3	Discussion . . . . .	67
<b>5</b>	<b>Conclusions</b>	<b>71</b>
<b>A</b>	<b>OpenWrist Kinematic and Dynamic Equations</b>	<b>73</b>
	<b>Bibliography</b>	<b>83</b>

# Figures

1.1	(a) The MIT-MANUS (InMotion ARM) end-effector based rehabilitation robot. (b) MAHI-Exo II exoskeleton based rehabilitation robot. . . . .	3
1.2	The Maestro hand exoskeleton developed by the ReNeu Lab at the University of Texas in Austin uses remotely located actuators and a Bowden cable style transmission to actuate the thumb, index, and middle fingers. . . . .	4
1.3	A preliminary implementation of the READAPT utilized a heavily modified version of the existing RiceWrist-S wrist exoskeleton and an early iteration of the Maestro hand exoskeleton. [1] . . . . .	5
2.1	MAHI OpenWrist – 3 DOF forearm and wrist exoskeleton for pathology agnostic rehabilitation in a standalone, wrist-only configuration. . . . .	10

- 2.2 Joint 1: Pronation/Supination – **(a)** The fixed elbow support assembly includes: a bolt-plate for rigidly securing device to a mechanical breadboard; the curvilinear slider mechanisms; the actuator for joint 1 (PS); and the adjustable elbow cuff. **(b)** The components that contribute to the mass and inertial properties of the PS link. The curvilinear rails, not visible, are mounted behind the central hub. Note that the actuator for joint 2 (FE) is also mounted to the hub. This sub-assembly is conceptual and never independently realized; link 1 is instead assembled as in **(c)** where the hub is mounted to the fixed elbow support assembly via the curvilinear rails, and front portion containing the joint 2 (FE) bearings is contained within the FE sub-assembly (Fig. 2.3)-b. This configuration is referred to as the “PS Module”. . . . . 11
- 2.3 Joint 2: Flexion/Extension – **(a)** The components that contribute to the mass and inertial properties of th FE link. Note the placement of the joint 3 (RU) actuator in the center of the FE axis. **(b)** The actual assembly of the “FE Module”. Here, components contained within the RU module (see Fig. 2.4-b) are removed and the assembly containing the FE bearings in Fig. 2.2-b is added. This configuration allows for rapid ambidextrous reconfiguration discussed later in the this chapter (Fig. 2.7). . . . . 13
- 2.4 Joint 3: Radial/Ulnar Deviation – **(a)** The components that contribute to the mass and inertial properties of the RU link. **(b)** The actual “RU Module” assembly houses the RU capstan and spool, 3 idler pulleys, and an Oldham quick-connect coupler. **(c)** The “Grip Module” detached from the RU capstan. Note the passive linear degree of freedom at the base of the grip. . . . . 14

2.5	Foam padded elbow support – <b>(a)</b> Hand knobs can be loosened to adjust the support laterally. <b>(b)</b> Small size cuff assembly can be quickly swapped with a large size cuff assembly. . . . .	15
2.6	In-line cable tensioning mechanisms for each joint. All tensioners are adjustable with a standard 1/4 inch wrench when provided with pre-made cable sections and crimped on copper fittings. <b>(a)</b> Tensioner mechanism for PS joint (panel removed), <b>(b)</b> tensioner mechanism for FE joint (panel removed), <b>(c)</b> tensioner mechanism for RU joint. . . . .	15
2.7	Device modularity and ambidextrous reconfiguration – <b>(a)</b> The device assembled in a right-handed configuration. <b>(b)</b> The device undergoing reconfiguration. First, the device is disassembled into five sub-assemblies – the PS Module (i), the FE Module (ii), the FE actuator (iii), the RU Module (iv), and the Grip Module (v). Next, the FE actuator is translated to the opposite side and secured in a custom “+” shaped socket. The FE Module is then rotated 180° and reattached to the PS Module. The RU Module is translated to the opposite side and reattached to the now rotated FE Module. Finally, the Grip Module is rotated 180° and reattached to the RU Module. <b>(c)</b> The device assembled in a left-handed configuration. . . . .	16
2.8	Other considerations – <b>(a)</b> Ceramic hybrid ball bearings feature ceramic balls in steel races, providing reduced friction. <b>(b)</b> Electrical wire routing through joint axes reduces wire draping and drag. . . . .	17



- 2.9 Demonstration of the polymer-ceramic coating applied to the OpenWrist when used under passive marker motion capture – **(a)** the motion capture volume as captured by a hand-held digital camera. The RiceWrist-S (left) and OpenWrist (right) are placed in the background, and a motion capture “rigid body” featuring five markers is placed in the foreground. **(b)** The same environment as captured by the motion capture system’s infrared camera. **(c)** The processed black-and-white version of (b) to be used for marker position extraction. Ideally, only the markers should be visible (seen in the bottom half of the frame); however, the uncoated RiceWrist-S produces false marker readings (seen in the upper half of the frame). The polymer-ceramic coating on the OpenWrist completely eliminates its infrared signature, making it suitable for motion capture studies. 17
- 2.10 **(a)** A traditional vertical grip (i) was initially tested and was found to prohibit full range of motion in radial deviation. Angled grips of 25° (ii) and 35° (iii) regained the lost range, but caused the wrist to pivot and draw the linear slider rearward, resulting in collisions with the FE Module. The final grip (iv), angled at 30° positions the linear slider attachment point forward and has a contoured underside to minimize collision with the FE Module. **(b)** User interfacing with the OpenWrist via the final 30° modified grip. . . . . 19
- 2.11 ROM in the RU joint as a function of FE joint angle for the multiple grip styles evaluated. Shaded regions place emphasis on the workspace of the vertical grip and the final 30° angled grip that was chosen. . . . . 19
- 2.12 The chosen assignment of each joint Z-axis for the proximal Denavit Hartenberg convention. PS (red), FE (green), and RU (blue) links are highlighted to match their respective axes. . . . . 20

2.13	(a) Quanser Q8-USV data acquisition device. (b) Quanser VoltPAQ-X4 linear voltage amplifier. . . . .	23
2.14	First order current controller with feed forward. Controller gains are listed in Table 2.3 and the plant $G(s)$ is defined in Eq. 2.8. . . . .	24
2.15	Major design changes between the RiceWrist-S (left) and the OpenWrist (right) – (a) PS joint now open, (b) padded elbow support introduced, (c) FE actuator moved to palmar side, (d) RU actuator moved closer to PS axis, (e) RU bridge eliminated to minimize interference with Maestro, (f) RU module moved to dorsal side. . . . .	26
2.16	MAHI OpenWrist exoskeleton module shown with the ReNeu Maestro hand exoskeleton module in the combined READAPT configuration. . . . .	26
3.1	Characterization experimental setups. In each case, the joint in question is parallel to gravity and the remaining joints are locked in their neutral position with a PD controller. For FE and RU experiments, the PS joint was also pinned with a dowel rod. (a) Setup for PS joint experiments. (b) Setup for FE joint experiments. (c) Setup for RU joint experiments. . . . .	29
3.2	Representative step input responses for PS (top), FE (middle), and RU (bottom), when starting about $0^\circ$ . Note that only one cycle from the response is shown; all three cycles are shown in the inlaid plot. . . . .	31
3.3	Representative simulated responses compared with the actual responses for PS (top), FE (middle), and RU (bottom). Here, each response is taken from the upper response of the first square wave cycle when starting from $0^\circ$ (see Fig. 3.2). . . . .	33
3.4	Ramp input position and velocity responses for PS (top), FE (middle), and RU (bottom). . . . .	35

3.5 Static friction of the PS, FE, and RU joints taken during the ramp test and plotted along their respective workspaces. . . . . 36

3.6 Schroeder multisine input responses for PS (top), FE (middle), and RU (bottom). The input excites the joint through a range of increasing frequencies. . . . . 39

3.7 Bode plots obtained by estimating the transfer function of Fig 3.6. Bandwidth values, defined by the -3 dB cutoff, are 4.7, 7.0, and 9.8 Hz for the PS, FE, and RU joints, respectively. . . . . 40

4.1 Velocity profiles for the RiceWrist-S (left) and OpenWrist (right) in the four task-space directions tested. . . . . 44

4.2 Conditions of subject study A. **(a)** Subject in the no-robot condition. The forearm was secured through a rigid splint that could be compressed with a tied lace. **(b)** Subject in the robot condition. The forearm is secured to the adjustable forearm rest of the OpenWrist, itself secured to the platform below it. . . . . 46

4.3 The real-time visual display used during the task of subject study A. The small black dot is the subject’s cursor and current position, and the large gray dots are the targets. The subject moves to a new target when it turns green, at a speed suggested by the closing of a rectangular gate around the target. . . . . 47

4.4 The presented joint angle visualization (left) and the actual joint angle mapping (right) that was chosen to reflect a constant portion of the ROM. Target locations were chosen by reducing the average wrist ROM defined in [2] by 40% and distributing targets around the perimeter in 45° increments. . . . . 47

4.5 Two rigid bodies (red) defined by the motion capture markers. . . . . 49

4.6	Illustration of the 3D calibrated, anatomically inspired axes. Anatomical and robot axes are indicated with ‘a’ and ‘r’ subscripts, respectively, while the orthogonally imposed anatomical RU axis is indicated with ‘a’. The axes used for joint measurement are indicated by the solid black lines. . . . .	49
4.7	Representative plots of the task space movement paths generated by a single subject. Units on the horizontal and vertical axes correspond with those in the visualization (see Fig. 4.4). . . . .	52
4.8	Mean normalized velocity profiles with standard deviation for all subjects during the slow trials. . . . .	53
4.9	Mean normalized velocity profiles with standard deviation for all subjects during the fast trials. . . . .	54
4.10	The mean smoothness correlation coefficient, $\rho$ , for all subjects during the slow trials. Difference is defined as $\rho_{\text{robot}} - \rho_{\text{no robot}}$ . Error bars are for a 95% confidence interval (1.96 times the standard error). . . . .	55
4.11	The mean smoothness correlation coefficient, $\rho$ , for all subjects during the fast trials. Difference is defined as $\rho_{\text{robot}} - \rho_{\text{no robot}}$ . Error bars are for a 95% confidence interval (1.96 times the standard error). . . . .	55
4.12	Spectral arc length for all subjects during the slow trials. Difference is defined as $\text{SAL}_{\text{robot}} - \text{SAL}_{\text{no robot}}$ . Error bars are for a 95% confidence interval (1.96 times the standard error). . . . .	56
4.13	Spectral arc length for all subjects during the fast trials. Difference is defined as $\text{SAL}_{\text{robot}} - \text{SAL}_{\text{no robot}}$ . Error bars are for a 95% confidence interval (1.96 times the standard error). . . . .	56

4.14 The real-time visual display of the user’s cursor (small orange circle) and nine targets shown to subjects during the experiment (note text and dashed lines shown here for reference only). In this trial, the diagonal target requiring an equal combination of radial deviation and extension has turned green, indicating a movement should be made to it. When a target becomes active, a virtual tunnel is implemented (light blue) to aid the user in making movements along the desired axis. The text next to the targets correspond to: extension (E), flexion (F), radial (R) deviation, ulnar (U) deviation, and diagonal (D). 60

4.15 (Left) Subject’s neutral posture in conditions 1, 3 and 4 as determined by the intended use of the robot. (Right) Subject’s neutral posture in condition 2 where wrist FE is aligned with joint 3, and RU is aligned with joint 2. A rotated grip was used in this condition. . . . . 61

4.16 Velocity profiles for FE and RU for all four conditions. For visualization, movements were normalized with respect to time and amplitude. Movements made on the robot’s second joint are in green, while movements made on the robot’s third joint are in blue. The red dots indicate the average peak time for a given movement direction and condition. For reference, a vertically dashed line is shown at  $t=0.5$  which is the peak time for the minimum jerk trajectory. . . . . 64

4.17 Plot of the minimum jerk trajectory against representative velocity profiles from C1 for FE, RU, and D. Representative velocity profiles were selected with  $\rho$  and peak time values approximately that of the group mean. Time and amplitude were normalized for comparison purposes. . . . . 65

4.18	Movement smoothness correlation coefficient $\rho$ for all FE and RU conditions. Error bars are for a 95% confidence interval (1.96 times the standard error) of all movements for a given condition and movement axis. Statistical significance is indicated by *. (a) Comparison of C1 and C2. (b) Comparison of C1, C3, and C4. . . . .	66
4.19	Movement smoothness correlation coefficient $\rho$ for all diagonal axes and conditions. Error bars are for a 95% confidence interval (1.96 times the standard error) of all movements for a given condition. . . . .	67

# Tables

2.1	Proximal Denavit Hartenberg Parameters . . . . .	21
2.2	Actuator and Sensor Details . . . . .	23
2.3	Current Controller Details . . . . .	25
2.4	Range of motion (ROM) and torque output of the OpenWrist compared with activities of daily living (ADL) and other wrist devices including the MIT-Manus (MIT) [3], RiceWrist (RW) [4], RiceWrist-S (RW-S) [5], Wrist Gimbal (WG) [6], and IIT Wrist Robot (IIT) [7]. . . . .	27
3.1	Step Input Experiment PD Control Gains . . . . .	30
3.2	Step Input Experiment Results . . . . .	34
3.3	Ramp Input Experiment PD Control Gains . . . . .	36
3.4	Ramp Input Experiment Results . . . . .	37
3.5	Schroeder Wave Input Experiment PD Control Gains . . . . .	38
3.6	Average device characteristics for the MAHI RiceWrist (RW) [4], RiceWrist-S (RW-S) [8], and OpenWrist wrist exoskeletons. . . . .	41
4.1	Experimental Conditions for Subject Study B. . . . .	62
4.2	Group Mean $\rho$ Values for Subject Study B. . . . .	66

# Chapter 1

## Introduction

### 1.1 Background

As the fifth leading cause of death in the United States and the leading cause of long-term disability, cerebrovascular accidents (CVAs or strokes) impact approximately 795,000 individuals each year. The related costs are projected to rise above the 2012 estimate of \$316.6 billion as survival rates continue to increase [9]. In addition, nearly 17,000 individuals per year will experience a Spinal Cord Injury (SCI) with yearly direct and indirect costs totaling \$20 billion. While CVA typically affects an older population, the average age of injury for SCI is under the age of 41. As such, SCI sufferers often live decades past their date of injury and incur a much heavier economic burden due to their disabilities [10]. Improving the rehabilitative outcomes for individuals with disabling neuromuscular conditions will have large social and economic impacts.

Of the 7 million stroke survivors, over 90% will require rehabilitation of the hand and wrist before they can perform activities of daily living (ADL) such as self-feeding, dressing, and bathing [9]. For SCI, approximately 50% of all sufferers will also require similar rehabilitation [11]. Rehabilitation regimes typically employ task-oriented movements to strengthen muscles and coordination in these patients [12], and intensive therapy with high repetition numbers and long duration has been shown to improve functional outcomes by recovering lost brain plasticity [13]. As a result, re-



habilitation sessions are labor intensive, expensive, and consequentially often shorter than they should be [14]. Furthermore, the clinician’s ability to deliver high quality and consistent training also affects the therapeutic outcome of the patient.

Robotic rehabilitation devices have been proposed as a tool for clinicians in meeting the rising demand for training sessions. In addition to their ability to provide accurate and repeatable movements over long durations and high repetitions, robotic devices can also be leveraged to record objective, quantitative performance data for tracking the therapeutic progress of patients. These devices have been clinically verified as a path forward for both CVA and SCI rehabilitation in a number of clinical studies [3, 15–22].

## 1.2 Review of Upper-Extremity Rehabilitation Robots

Rehabilitation robots are typically classified as being either end-effector based robots or exoskeletons (see Fig. 1.1). An end-effector rehabilitation robot is one which only the robot’s most distal link, or end-effector, interacts with the user. The most historically significant upper-extremity end-effector rehabilitation robot designs include: the 2 degree of freedom (DOF), planar MIT-MANUS [3, 16, 23] (commercially known as the InMotion ARM/WRIST); the Mirror Image Movement Enabler (MIME) [24], a modification of the industrial 6-DOF PUMA robot; and the 3-DOF ARM Guide [15]. End-effector rehabilitation robots typically allow for large functional workspaces, but do not mirror human anatomy and are thus unable to apply torques directly to human joints.

Exoskeletons, on the other hand, are anthropomorphically designed where robot joint axes are typically collocated with human joints axes. They allow for the direct application of torque to individual joints. This mapping between robot and human

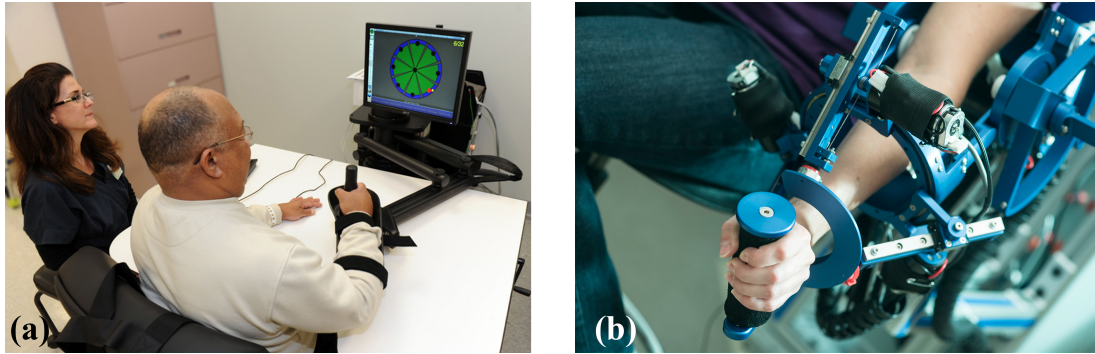


Figure 1.1 : (a) The MIT-MANUS (InMotion ARM) end-effector based rehabilitation robot. (b) MAHI-Exo II exoskeleton based rehabilitation robot.

movement makes exoskeletons more attractive than end-effector designs for rehabilitation robotics. Exoskeletons may be either worn by the user or grounded. Worn (or ungrounded) devices enable the user to engage in more natural movements in large workspaces, but are weight limited, primarily by their actuators, and cannot offer the torque capabilities that grounded robots do. Notable examples of upper-extremity exoskeletons include: the 6-DOF ARMin III [14], the 7-DOF CADEN-7 [25], the 5-DOF Rupert [26], 4-DOF MAHI-Exo II [27], and the 14-DOF X-Arm 2 (ungrounded). Specifically for wrist-only rehabilitation are the RiceWrist [28, 29], the RiceWrist-S [5, 8, 30], the HWARD [31], the WristGimbal [6], and the IIT Wrist Robot [7]. A more comprehensive survey of upper-extremity devices can be found in [32].

### 1.3 Hand and Wrist Robotic Rehabilitation

While many devices have been developed for the wrist and hand [33–37] separately, few allow for coordinated hand and wrist movement. This separated approach overlooks the kinematic and dynamic linkings of the hand and wrist due to tendon and muscle anatomy [38], as well as their position-dependent passive properties [39–42].

Furthermore, muscles, tendons, and ligaments exert forces across multiple DOF and give rise to complex synergies. Implementing separate hand and wrist devices precludes the ability to exploit or retrain these synergies. Therefore, integrated hand and wrist therapy has the potential to improve the rehabilitative outcomes [1].

The READAPT (Robotic Exoskeleton to Assist Distal Arm Physical Therapy), the coupling of a wrist exoskeleton developed in Rice University’s MAHI Lab and the Maestro hand exoskeleton (Fig. 1.2) developed in University of Texas’ ReNeu Lab, was proposed to enable the coordinated hand and wrist movements required in ADL as suggested by the interconnected nature of hand-wrist musculature [1]. However, the requirements for designing coordinated hand-wrist exoskeletons remains relatively unknown due the sparse landscape of such devices.

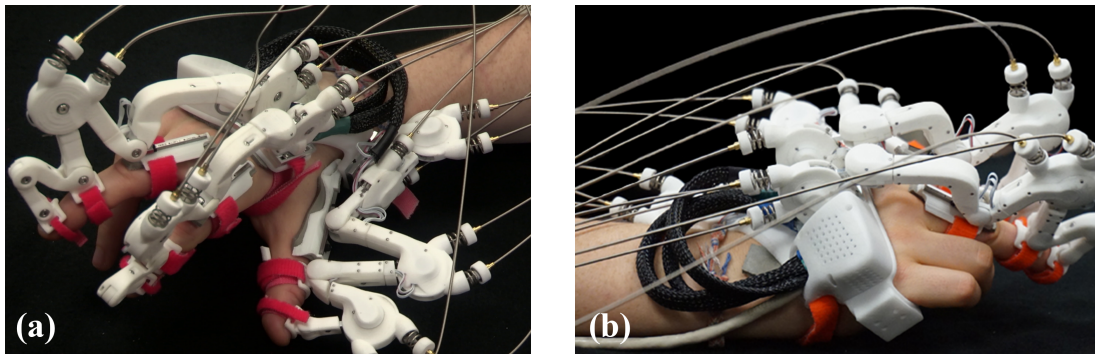


Figure 1.2 : The Maestro hand exoskeleton developed by the ReNeu Lab at the University of Texas in Austin uses remotely located actuators and a Bowden cable style transmission to actuate the thumb, index, and middle fingers.

## 1.4 Design Requirements for Hand-Wrist Rehabilitation Robots and READAPT

Rehabilitation robots must generally possess several key properties: (1) the ability to apply ergonomically appropriate torques directly to human joints [43, 44]; (2) a

functional workspace meeting the requirements for activities that will be trained [43]; (3) high backdravability with zero backlash [45], (4) quantitative evaluation of treatment [44]; and (5) the means to implement advanced control algorithms [46].

Requirements specific to coordinated hand-wrist rehabilitation robots have also been identified. A preliminary implementation of the READAPT, which utilized the existing RiceWrist-S exoskeleton [5], identified finger metacarpalphalangeal (MCP) flexion/extension range of motion (ROM) limits (subsequently addressed in [47]), wrist static friction and inertia, and undesired interactions between the hand and wrist modules as key contributors to hand-wrist discoordination in redundant MCP and wrist flexion/extension pointing tasks [1]. Additionally, pre-clinical trials with the RiceWrist-S in a standalone mode [5], as well as experience and clinician feedback from other clinical studies [48], highlighted the necessity of the user’s ability to easily don/doff devices. This is especially true during studies with fragile skinned subjects where donning/doffing closed-design exoskeletons (e.g. [5, 6, 27]) is not only difficult and time consuming, but also potentially hazardous.

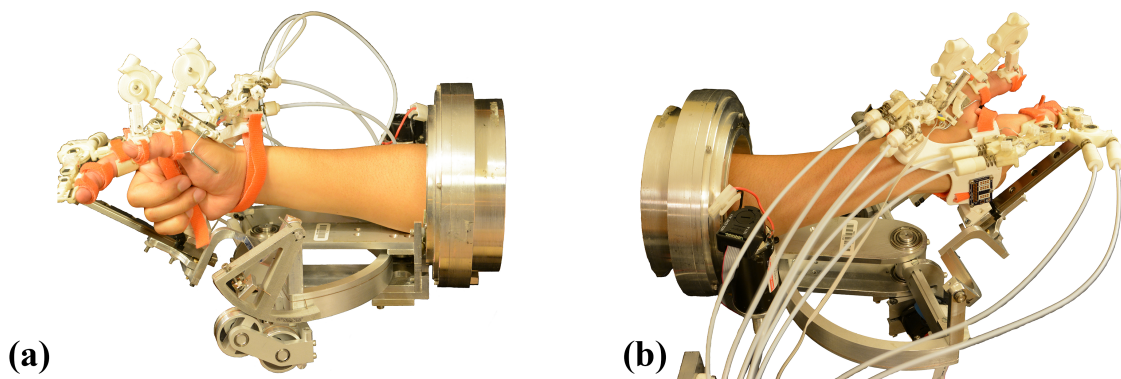


Figure 1.3 : A preliminary implementation of the READAPT utilized a heavily modified version of the existing RiceWrist-S wrist exoskeleton and an early iteration of the Maestro hand exoskeleton. [1]

In order of importance, future hand-wrist exoskeletons, including the READAPT, would need to (6) provide a harmonious interface between the the hand and wrist modules, (7) enable don/doff of impaired individuals with an easily accessed open design, (8) address ergonomics and user comfort, (9) and minimize the discoordinating effects of friction and inertia. Further increasing dynamic performance over previous devices and enabling compatibility with surface electromyography (sEMG) and passive marker motion capture were also included as design requirements specific to the READAPT. Following the guidelines of (1-9), this thesis details the design of the OpenWrist, the new wrist module of the READAPT.

## 1.5 Characterization and Validation of Rehabilitation Robots

Characterization of rehabilitation robots generally falls into one of two categories. The first category involves properties that may indicate how well the robot will perform as a *training* device. The two most important properties, given by the design requirements (1) and (2), are torque output and ROM. The device must be able to provide interaction forces and a workspace sufficient to train desired activities. Following torque and ROM are dynamic properties of the robot such as inertia, viscous damping, and static and kinetic friction. Together, these properties indicate how transparent a device may be. Highly transparent devices, ones in which passive interaction forces between the human and robot are small, are desired for robotic rehabilitation since we would like to preserve natural human motion as much as possible. Intuitively, lower values of inertia, damping, and friction will give rise to a more transparent device.

The second category, often overlooked in the development of rehabilitation robots, includes analyses that may indicate how accurately the device will perform as an *as-*

*essment* or measurement tool. Several metrics exist for assessment, however one of the most prominent is movement smoothness. It is well known that healthy individuals generate smooth movements during pointing or reaching tasks [49–51]. As such, tracking the improvement of movement smoothness during stroke rehabilitation may be indicative of therapeutic outcomes. The same robots that are employed for rehabilitation training are often used as assessment tools, usually through an unpowered back-drive [18] mode, or, if necessary, a “zero-impedance” mode where robot dynamics are canceled in the control implementation. A non-trivial assumption is usually made during assessment: that the robot has minimal effect on the measurements used to compute assessment metrics. This assumption has been shown to be invalid [1, 52, 53]. A direct comparison between movement in the presence of the rehabilitation robot and the same movement in a no-robot condition is required to characterize and validate the device as an accurate assessment tool.

While the second category is intimately tied with the first (specifically through device transparency), to what extent remains an open question in the field. Specifically, what properties of the robot give rise to unnatural movements? Portions of this thesis attempt to provide some answers to this question.

## 1.6 Thesis Outline

This thesis is structured as follows: Chapter 2 details the design and development of the OpenWrist, the new wrist exoskeleton module to be used for coordinated hand-wrist rehabilitation in conjunction with the ReNue Maestro hand-exoskeleton, collectively known as the READAPT. Each of the nine design requirements for hand-wrist exoskeletons in Section 1.4 are addressed. Chapter 3 provides the characterization of performance properties of the OpenWrist as a training device, including joint iner-

tia, viscous damping, static and kinetic friction, and closed-loop position bandwidth. Both Chapters 2 and 3 conclude with a comparison between the OpenWrist and other wrist-exoskeletons. Chapter 4 validates the OpenWrist as an assessment device, while also providing some insight into the effects that robot dynamic properties have on assessment smoothness metrics.

## Chapter 2

### Design

This chapter presents the mechanical design of the OpenWrist (Fig. 2.1), a 3 degree of freedom (DOF) robotic exoskeleton for rehabilitation of the wrist and hand following spinal cord injuries and cerebrovascular accidents (CVA). The device incorporates several major improvements over those previously developed in the Mechatronic and Haptic Interfaces (MAHI) Lab, and allows for compatibility with the ReNeu Maestro Hand Exoskeleton (see Fig. 2.16). The kinematic structure and mechatronic implementation are also discussed. The chapter concludes with quantitative comparisons of capabilities between the OpenWrist and other wrist exoskeletons. A preliminary coupling with the ReNue Maestro hand exoskeleton is also presented.\*

#### 2.1 Mechanical Design

The OpenWrist is the evolution of the RiceWrist-S, previously presented in [5] and shown in Fig. 2.15, with major refinements to each degree of freedom (DOF) to increase performance, functionality, and most importantly, compatibility with the Maestro hand exoskeleton. Like its predecessor, it employs a serial RRR mechanism for manipulation of the user's wrist and forearm in favor of the parallel RPS mechanism found on the RiceWrist [29]. While a parallel RPS mechanism offers extremely

---

\*Portions of this chapter originally appeared in a paper submitted by Pezent, Rose, Desphande, and O'Malley in April 2017 [54]. Here, the work is expanded to include new commentary and additional figures.



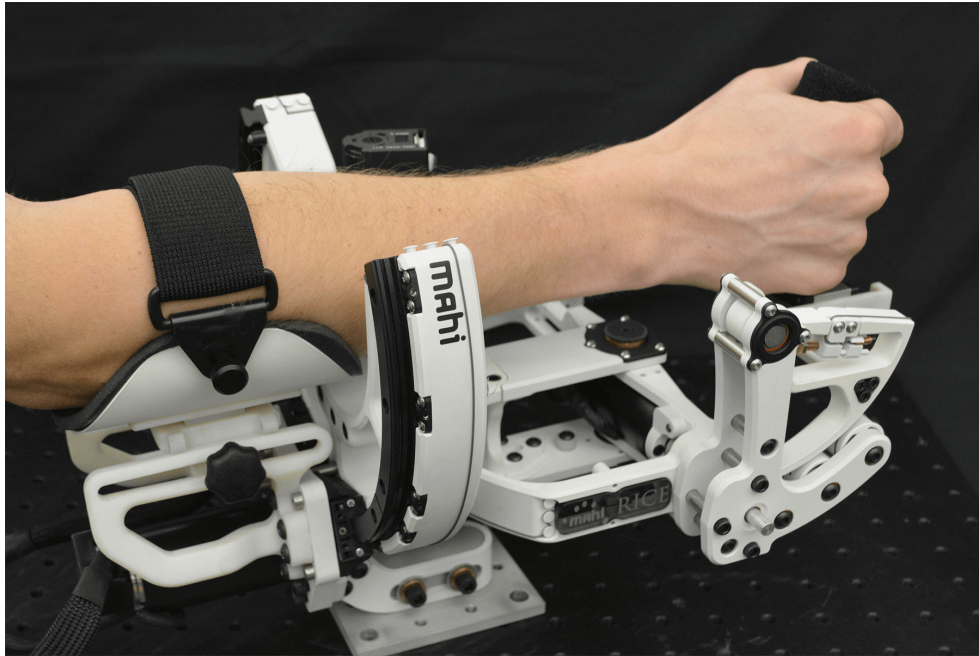


Figure 2.1 : MAHI OpenWrist – 3 DOF forearm and wrist exoskeleton for pathology agnostic rehabilitation in a standalone, wrist-only configuration.

low inertia and friction at the wrist, its range of motion (ROM) and torque capabilities cannot satisfy the requirements for training activities of daily living (ADL). The serial RRR mechanism solves this issue, but introduces increased inertia and friction. The first rotational joint actuates pronation/supination (PS) of the forearm, while the second and third actuate flexion/extension (FE) and radial/ulnar deviation (RU) of the wrist, respectively. A fourth passive linear degree of freedom between the third joint and the point of human interface (i.e. the Maestro hand exoskeleton or the optional hand grip discussed in Section 2.1.4) allows for small misalignments between the user's and robot's joints. Each actuated DOF is powered by a brushed DC motor (see Table 2.2). To ensure backlash free operation, power is transmitted through capstan-cable drives, which involves winding a high tensile strength cable around a small diameter threaded spool and terminating the cable on the ends of a

larger diameter capstan arc. The overall design and novel features of each individual DOF and the entire unit are detailed in the subsections that follow, and device capabilities are provided in Table 2.4.

### 2.1.1 Joint 1: Pronation/Supination

The PS joint has been designed to address a major concern for robotic exoskeletons: donning and doffing. All MAHI Lab designs thus far have required that the user insert their hand through an ring encompassing the PS joint. This task, trivial for non-impaired users, proves challenging for impaired subjects with reduced motor control and spasticity. Furthermore, a closed design requires that the Maestro hand exoskeleton be awkwardly donned after the user has inserted their arm into the wrist

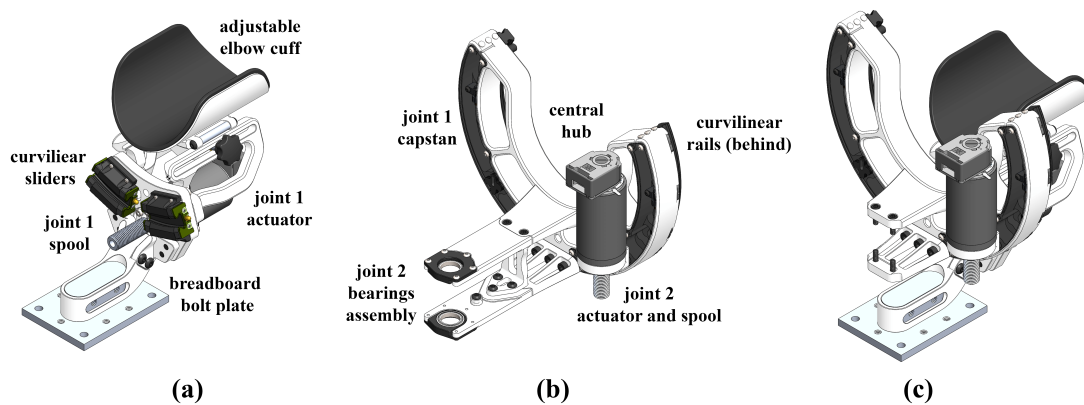


Figure 2.2 : Joint 1: Pronation/Supination – (a) The fixed elbow support assembly includes: a bolt-plate for rigidly securing device to a mechanical breadboard; the curvilinear slider mechanisms; the actuator for joint 1 (PS); and the adjustable elbow cuff. (b) The components that contribute to the mass and inertial properties of the PS link. The curvilinear rails, not visible, are mounted behind the central hub. Note that the actuator for joint 2 (FE) is also mounted to the hub. This sub-assembly is conceptual and never independently realized; link 1 is instead assembled as in (c) where the hub is mounted to the fixed elbow support assembly via the curvilinear rails, and front portion containing the joint 2 (FE) bearings is contained within the FE sub-assembly (Fig. 2.3)-b. This configuration is referred to as the “PS Module”.

exoskeleton. Eliminating this shortcoming was accomplished by switching from a traditional closed radial bearing to an open curvilinear rail and slider solution (seen in Fig. 2.1 and Fig. 2.2). Four  $60^\circ$ , 100mm radius rail sections are mounted to a hub to provide  $240^\circ$  of rail space. To support expected moment loads, two slider mechanisms are used, each mounted to a fixed frame and elbow support assembly, as shown in Fig. 2.2-a. Thus, it is the rails and hub that move instead of the sliders themselves. The spacing of the sliders is such that approximately  $170^\circ$  of motion is achievable in the PS joint. The decision to have the rail hub rotate was made so that it could simultaneously serve as a capstan arc in the transmission system. Unlike the RiceWrist-S, which used a direct drive motor, the PS joint in the OpenWrist employs a capstan-cable transmission. As a result, the new device more than doubles torque output from 1.69 Nm to 3.50 Nm.

### **2.1.2 Joint 2: Flexion/Extension**

With the addition of the relatively heavy rails and hub, significant changes to distal joints were necessary to offset the added inertia to the PS joint. First, the distance from the PS joint to the center of the FE axis was shortened. This change not only removed unnecessary material and weight, but also allowed for the elimination of an idler pulley mechanism present in the RiceWrist-S. It is worth noting that the FE actuator was also relocated from the dorsal side of the hand to the palmer side as shown in Fig. 2.2-b and Fig. 2.15-c. Second, the RU actuator was moved approximately 2 inches closer to the PS axis by creating a gap in the FE capstan and shaft for the motor (Fig. 2.3 and Fig. 2.15-d).

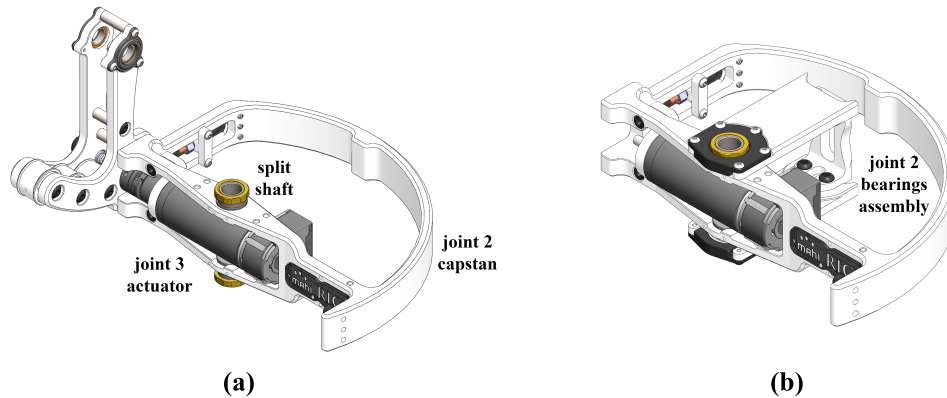


Figure 2.3 : Joint 2: Flexion/Extension – **(a)** The components that contribute to the mass and inertial properties of the FE link. Note the placement of the joint 3 (RU) actuator in the center of the FE axis. **(b)** The actual assembly of the “FE Module”. Here, components contained within the RU module (see Fig. 2.4-b) are removed and the assembly containing the FE bearings in Fig. 2.2-b is added. This configuration allows for rapid ambidextrous reconfiguration discussed later in this chapter (Fig. 2.7).

### 2.1.3 Joint 3: Radial/Ulnar Deviation

Due to the placement of the RU actuator, the point of contact between the actuator shaft and capstan arc requires relocation so that an appropriate range of motion is achievable. Previously, the RiceWrist-S accomplished this via a method described in [5], which involved spanning and tensioning cable between a threaded motor shaft and a second threaded aluminum shaft. Issues with robustness and maintaining cable tension led to a modification which introduced two idler pulleys as a means to relocate the point of contact, as seen in Fig. 2.15. Further improvements to this idler pulley method were made with the OpenWrist. To reduce overall form-factor, three smaller pulleys were substituted for the two large pulleys. In addition, the threaded spool was doubly supported to prevent deflection in the spool as the cable is tensioned, thus reducing binding and friction.

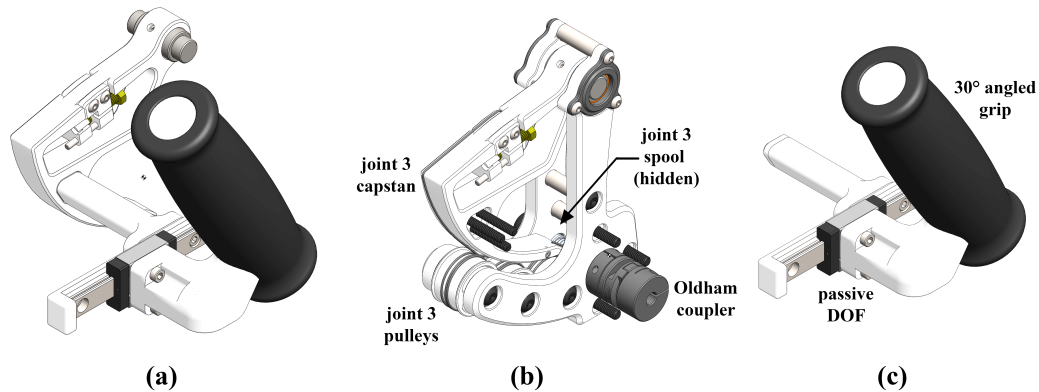


Figure 2.4 : Joint 3: Radial/Ulnar Deviation – (a) The components that contribute to the mass and inertial properties of the RU link. (b) The actual “RU Module” assembly houses the RU capstan and spool, 3 idler pulleys, and an Oldham quick-connect coupler. (c) The “Grip Module” detached from the RU capstan. Note the passive linear degree of freedom at the base of the grip.

To maximize compatibility with the Maestro hand exoskeleton, two additional key changes were made. First, the overhanging bridge coupling the RU DOF to the hand, which would have made interfacing with the Maestro impossible, was eliminated (Fig. 2.15-e). Second, the RU capstan and transmission assembly was relocated from the palmar side of the hand to the dorsal side (Fig. 2.15-f) to prevent interference with the hand exoskeleton during grasping motions.

#### 2.1.4 Practical Considerations

Several features have been introduced to make the device more functional for users, clinicians, and researchers alike. A foam padded elbow support (Fig. 2.5) addresses an ergonomic downfall of previous devices. The support can be adjusted laterally and vertically and fitted with small and large sized cuffs. The support preserves the integral assumption of exoskeletons by reducing user movement with respect to the exoskeleton, and avoids an oversight present in previous devices whereby subjects with fragile skin would come into contact with bare metal surfaces, pinch points, and exposed fasteners.

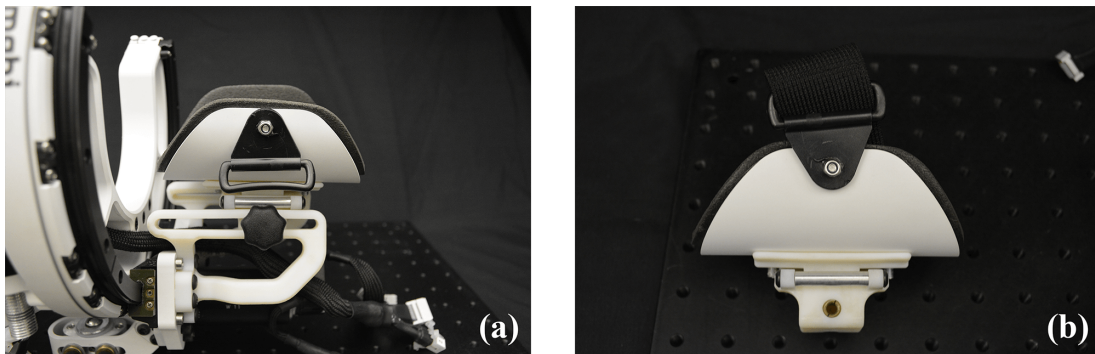


Figure 2.5 : Foam padded elbow support – (a) Hand knobs can be loosened to adjust the support laterally. (b) Small size cuff assembly can be quickly swapped with a large size cuff assembly.

Each joint integrates an in-line cable tensioning mechanism (Fig. 2.6). With clinicians in mind, all joints can be quickly re-wrapped and tensioned when provided with a 1/4" wrench and pre-made cable sections. It is worth noting that the choice of cable was also upgraded to pre-stretched, ultra-flexible 7x19 strand core stainless steel which further reduces friction and prevents loosening with continued use.

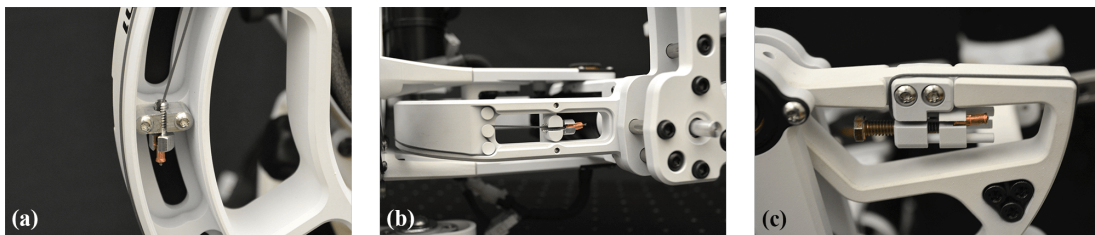


Figure 2.6 : In-line cable tensioning mechanisms for each joint. All tensioners are adjustable with a standard 1/4 inch wrench when provided with pre-made cable sections and crimped on copper fittings. (a) Tensioner mechanism for PS joint (panel removed), (b) tensioner mechanism for FE joint (panel removed), (c) tensioner mechanism for RU joint.

Since ROM in the FE joint is asymmetrical, the ability to change between left-handed and right-handed configurations was implemented. The process for changing configurations is detailed in Fig. 2.7. Note that because the PS and RU modules' cable windings are self-contained, only the FE joint would require rewinding in the event of a configuration change.

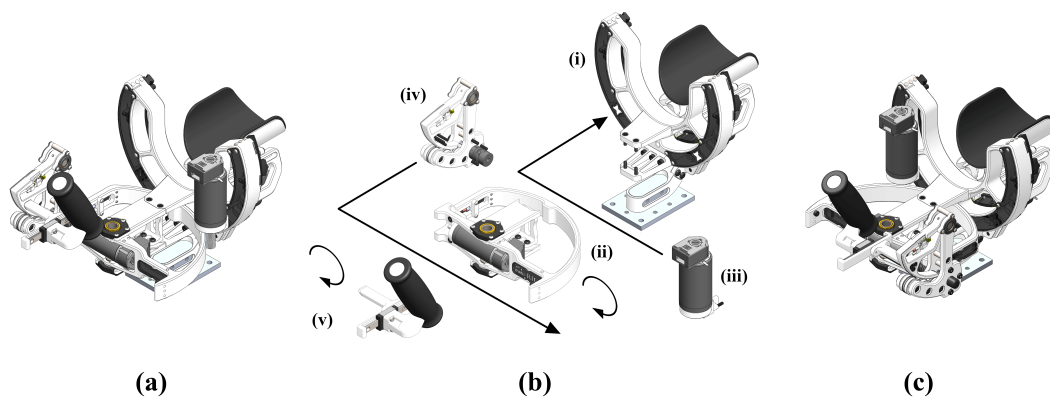


Figure 2.7 : Device modularity and ambidextrous reconfiguration – **(a)** The device assembled in a right-handed configuration. **(b)** The device undergoing reconfiguration. First, the device is disassembled into five sub-assemblies – the PS Module (i), the FE Module (ii), the FE actuator (iii), the RU Module (iv), and the Grip Module (v). Next, the FE actuator is translated to the opposite side and secured in a custom “+” shaped socket. The FE Module is then rotated 180° and reattached to the PS Module. The RU Module is translated to the opposite side and reattached to the now rotated FE Module. Finally, the Grip Module is rotated 180° and reattached to the RU Module. **(c)** The device assembled in a left-handed configuration.

Other improvements include: an upgrade from 6061-T6 to 7075-T6 aluminum alloys, allowing for reductions in thickness in multiple areas; the use of hybrid-ceramic ball bearings with  $\text{Si}_3\text{N}_4$  balls in the FE and RU joints, offering decreased friction and requiring no lubrication; and routing of electrical wires through joint axes to eliminate wire draping and drag (Fig. 2.8-b). Of particular interest is the application of a white polymer-ceramic coating, brand named Cerakote<sup>®</sup>. The coating, typically used for military small arms, reduces infrared signature, making passive marker motion

capture studies feasible (see Fig. 2.9), and has a high dielectric strength that enhances compatibility with sEMG.

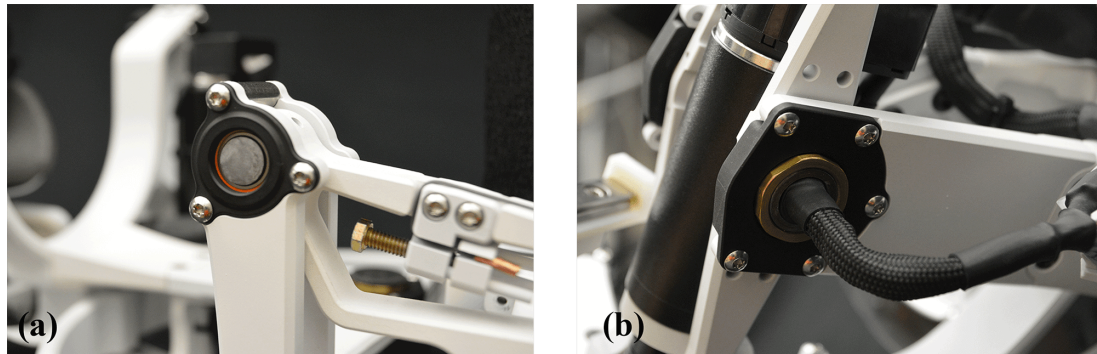


Figure 2.8 : Other considerations – (a) Ceramic hybrid ball bearings feature ceramic balls in steel races, providing reduced friction. (b) Electrical wire routing through joint axes reduces wire draping and drag.

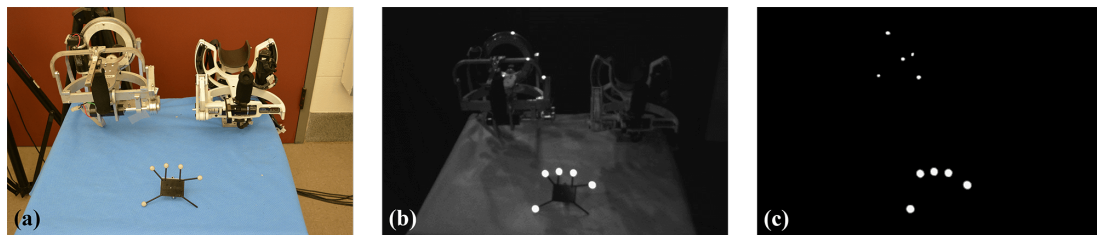


Figure 2.9 : Demonstration of the polymer-ceramic coating applied to the OpenWrist when used under passive marker motion capture – (a) the motion capture volume as captured by a hand-held digital camera. The RiceWrist-S (left) and OpenWrist (right) are placed in the background, and a motion capture “rigid body” featuring five markers is placed in the foreground. (b) The same environment as captured by the motion capture system’s infrared camera. (c) The processed black-and-white version of (b) to be used for marker position extraction. Ideally, only the markers should be visible (seen in the bottom half of the frame); however, the uncoated RiceWrist-S produces false marker readings (seen in the upper half of the frame). The polymer-ceramic coating on the OpenWrist completely eliminates its infrared signature, making it suitable for motion capture studies.



## Safety

A primary concern for developing rehabilitation robots to be used in a clinical setting is user safety. Several safety features were implemented on the OpenWrist to ensure safe operation. To prevent overextension of human joints, each joint of the OpenWrist integrates a mechanical hardtop at the ends of its ROM. Rate limiting blocks in the control implementation can be used to limit velocity, if desired, and current saturation blocks prevent over-torquing joints. Finally, an easily accessible emergency stop button, which must be connected for the system to initiate, can be used to deactivate all amplifiers in the case of an unexpected behavior.

## Hand Grip

Although users are primarily intended to interface the OpenWrist via the Maestro hand exoskeleton, a hand grip was developed should wrist-only studies be conducted. Virtually all wrist exoskeletons, including those developed by our group, feature a grip that is vertically oriented when the exoskeleton is in its neutral position. An overlooked flaw with this style of grip is that it puts the wrist in an orientation that is already significantly radially deviated. Thus, the neutral orientations of the robot and user do not coincide. To address this, multiple grip angles (see Fig. 2.10) were evaluated during the design phase. Fig. 2.11 maps the achievable ROM in the RU joint workspace as FE is varied in  $5^\circ$  increments for the four grips tested. Note the significant increase in the upper workspace limits from the vertical grip to the angled grips. However, simply including an angle, as with the  $25^\circ$  and  $35^\circ$  grips, also resulted in the misalignment of joint axes and collision with the exoskeleton before reaching the lower workspace limits. The final grip (depicted in Fig. 2.10-b), has an altered geometry at its attachment point to regain this lost lower workspace and is angled

at  $30^\circ$  based on user feedback for the the  $25^\circ$  and  $35^\circ$  grips. Compared with the traditional vertical grip, the new angled grip offers an increase of approximately 51% in FE-RU workspace area.

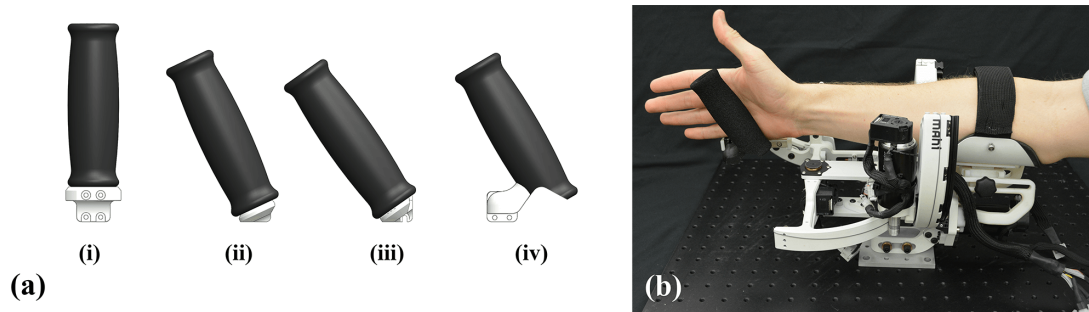


Figure 2.10 : **(a)** A traditional vertical grip (i) was initially tested and was found to prohibit full range of motion in radial deviation. Angled grips of  $25^\circ$  (ii) and  $35^\circ$  (iii) regained the lost range, but caused the wrist to pivot and draw the linear slider rearward, resulting in collisions with the FE Module. The final grip (iv), angled at  $30^\circ$  positions the linear slider attachment point forward and has a contoured underside to minimize collision with the FE Module. **(b)** User interfacing with the OpenWrist via the final  $30^\circ$  modified grip.

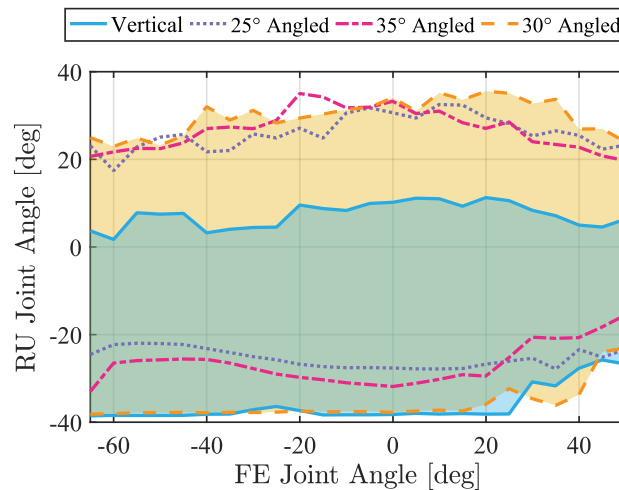


Figure 2.11 : ROM in the RU joint as a function of FE joint angle for the multiple grip styles evaluated. Shaded regions place emphasis on the workspace of the vertical grip and the final  $30^\circ$  angled grip that was chosen.

## 2.2 Kinematic Structure

The device's kinematic structure was modeled using the proximal Denavit Hartenberg (DH) parameter conventions detailed in [55] and differentiated from other DH conventions in [56]. Fig. 2.12 shows each joint's axis of rotation and the chosen direction of positive Z with regard to DH notation. Since all joint axes intersect, the origins of the base frame and each joint frame were placed coincidentally at the intersection point in an effort to keep as many parameters in the DH table as possible equal to zero. Note that the axes assignment detailed here differs from that presented in [5]. The new assignment was chosen such that a positive rotation about each axis, conventionally C.C.W when viewed from above, would correspond with the first letter in the joint's acronym, i.e., rotation in the direction of flexion (F) is positive and rotation in the direction of extension (E) is negative for the FE axis.

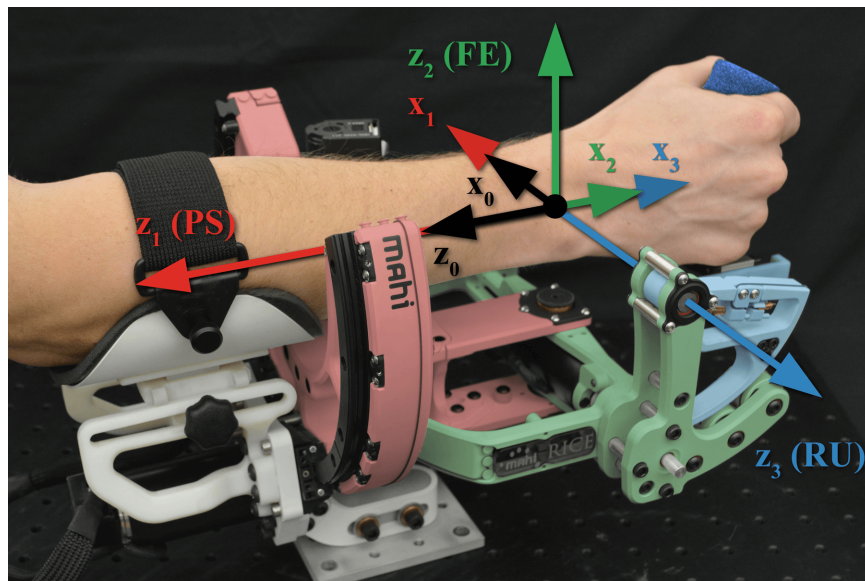


Figure 2.12 : The chosen assignment of each joint Z-axis for the proximal Denavit Hartenberg convention. PS (red), FE (green), and RU (blue) links are highlighted to match their respective axes.

The DH parameters  $a$ ,  $\alpha$ ,  $d$ , and  $\theta$  for joints 1, 2, and 3 are given in Table 2.1. Note that  $\pi/2$  is subtracted from  $\theta_2$  so that the FE joint is in its designed neutral position when  $\theta_2 = 0$ .

Table 2.1 : Proximal Denavit Hartenberg Parameters

i	$a_{i-1}$	$\alpha_{i-1}$	$d_i$	$\theta_i$
1	0	0	0	$\theta_1$
2	0	$\pi/2$	0	$\theta_2 - \pi/2$
3	0	$\pi/2$	0	$\theta_3$

Using Table 2.1, the transforms from  $\{i-1\}$  to  $\{i\}$  is can be computed with

$${}^i_{i-1}T = \begin{bmatrix} c\theta_i & -s\theta_i & 0 & a_{i-1} \\ s\theta_1 c\alpha_{i-1} & c\theta_1 c\alpha_{i-1} & -s\alpha_{i-1} & -s\alpha_{i-1}d_i \\ s\theta_1 s\alpha_{i-1} & c\theta_1 s\alpha_{i-1} & c\alpha_{i-1} & c\alpha_{i-1}d_i \\ 0 & 0 & 0 & 1 \end{bmatrix} \quad (2.1)$$

Finally, chaining together successive transforms yields the transform from  $\{3\}$  to  $\{0\}$ :

$${}^0_3T = {}^0_1T {}^1_2T {}^2_3T = \begin{bmatrix} s\theta_1 s\theta_3 + c\theta_1 c\theta_3 s\theta_2 & c\theta_3 s\theta_1 - c\theta_1 s\theta_2 s\theta_3 & -c\theta_1 c\theta_2 & 0 \\ c\theta_3 s\theta_1 s\theta_2 - c\theta_1 s\theta_3 & -c\theta_1 c\theta_3 - s\theta_1 s\theta_2 s\theta_3 & -c\theta_2 s\theta_1 & 0 \\ -c\theta_2 c\theta_3 & c\theta_2 s\theta_3 & -s\theta_2 & 0 \\ 0 & 0 & 0 & 1 \end{bmatrix} \quad (2.2)$$

### 2.3 Dynamic Model

The equations of motion (EOM) for the OpenWrist were computed symbolically in MATLAB (see Appendix A) using the iterative Newton-Euler dynamics algorithm described in [55]. First, velocities and accelerations are computed iteratively for each

link starting at link 1 and ending at link 3. Second, joint torques and interaction forces and torques are computed recursively from link 3 back to link 1. The effects of gravity are included simply by giving  $\{0\}$  an initial fictitious upward acceleration equal to  $[0, -g, 0]^T$ . The resulting output can be conveniently refactored in the form

$$\mathbf{T} = M(\Theta)\ddot{\Theta} + V(\Theta, \dot{\Theta}) + G(\Theta) \quad (2.3)$$

where  $M(\Theta)$  is the  $3 \times 3$  mass matrix,  $V(\Theta, \dot{\Theta})$  is the  $3 \times 1$  vector of centrifugal and Coriolis terms, and  $G(\Theta)$  is the  $3 \times 1$  vector of gravity terms. Torques due to reflected actuator rotor inertias and nonrigid body effects are included:

$$\mathbf{T}_{m,\text{ref}} = J_{m,\text{ref}} \circ \ddot{\Theta} \quad , \quad \mathbf{T}_B = B \circ \dot{\Theta} \quad , \quad \mathbf{T}_{F_K} = F_K \circ \text{sign}(\dot{\Theta}) \quad (2.4)$$

where

$$J_{m,\text{ref}} = [J_{m_1}\eta_1^2 \quad , \quad J_{m_2}\eta_2^2 \quad , \quad J_{m_3}\eta_3^2]^T, \quad (2.5)$$

$B$  is the  $3 \times 1$  vector of viscous damping coefficients,  $F_k$  is the  $3 \times 1$  vector kinetic friction parameters, and  $\circ$  denotes the Hadamard, or element-wise, product. Adding 2.4 to 2.3 yields the final EOM for the OpenWrist:

$$\mathbf{T} = M(\Theta)\ddot{\Theta} + V(\Theta, \dot{\Theta}) + G(\Theta) + J_{m,\text{ref}} \circ \ddot{\Theta} + B \circ \dot{\Theta} + F_k \circ \text{sign}(\dot{\Theta}) \quad (2.6)$$

or

$$\begin{bmatrix} \tau_1 \\ \tau_2 \\ \tau_3 \end{bmatrix} = \begin{bmatrix} m_{11} & m_{12} & m_{13} \\ m_{21} & m_{22} & m_{23} \\ m_{31} & m_{32} & m_{33} \end{bmatrix} \begin{bmatrix} \ddot{\theta}_1 \\ \ddot{\theta}_2 \\ \ddot{\theta}_3 \end{bmatrix} + \begin{bmatrix} v_1 \\ v_2 \\ v_3 \end{bmatrix} + \begin{bmatrix} g_1 \\ g_2 \\ g_3 \end{bmatrix} + \begin{bmatrix} J_{m_1}\eta_1^2\ddot{\theta}_1 + b_1\dot{\theta}_1 + f_{k1}\text{sign}(\dot{\theta}_1) \\ J_{m_2}\eta_2^2\ddot{\theta}_2 + b_2\dot{\theta}_2 + f_{k2}\text{sign}(\dot{\theta}_2) \\ J_{m_3}\eta_3^2\ddot{\theta}_3 + b_3\dot{\theta}_3 + f_{k3}\text{sign}(\dot{\theta}_3) \end{bmatrix} \quad (2.7)$$

Symbolic formulations of all  $m$ ,  $v$ , and  $g$  terms in 2.7 can be found in Appendix , and all  $b$  and  $f_k$  terms can be found in the experimental characterization presented in Chapter 3.

## 2.4 Mechatronics and Controls

All actuators are Maxon RE-series DC motors, each fitted with a Broadcom/Avago HEDL-5540 A11 optical encoder capable of 500 counts per revolution. Specific actuator details as well as transmission ratios and sensor resolutions at the joint are listed in Table 2.2. Power is supplied from a Quanser VoltPAQ-X4 amplifier (Fig. 2.13-b), and up to 4.16 A of continuous current can be provided to each actuator. The amplifier and encoders interface with MATLAB and Simulink through a Quanser Q8-USB data acquisition device (Fig. 2.13-a) and Quanser’s Quarc control software. The system is capable of operating at rates of up to 2 kHz depending on the complexity of the controller.



Figure 2.13 : (a) Quanser Q8-USB data acquisition device. (b) Quanser VoltPAQ-X4 linear voltage amplifier.

Table 2.2 : Actuator and Sensor Details

Joint	Actuator (PN)	Transmission	Sensor (Joint Resolution)
PS	Maxon RE-40 (148877)	1:18.7	Broadcom HEDL-5540 (0.0096°)
FE	Maxon RE-40 (148877)	1:19.2	Broadcom HEDL-5540 (0.0094°)
RU	Maxon RE-30 (310009)	1:25.6	Broadcom HEDL-5540 (0.0070°)

While the VoltPAQ-X4 is a linear voltage-controlled amplifier by default, experimental settings within the Quanser's Quarc control software allow the amplifier to be run in a closed-loop current control mode. A first order controller with feed forward, shown in Fig. 2.14, was chosen as the method of current control.

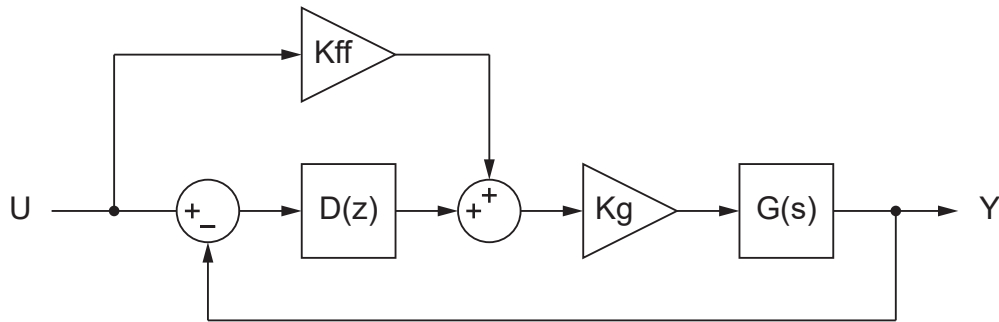


Figure 2.14 : First order current controller with feed forward. Controller gains are listed in Table 2.3 and the plant  $G(s)$  is defined in Eq. 2.8.

The actuator plant  $G(s)$  is given by the transfer function:

$$G(s) = \frac{I_a(s)}{V_a(s)} = \frac{J_m s + B_m}{L J_m s^2 + (R J_m + L B_m) s + (R B_m + K_t K_b)} \quad (2.8)$$

where  $J_m$  is the motor rotor inertia,  $B_m$  is the motor viscous damping,  $L$  is the terminal inductance,  $R$  is the terminal resistance,  $K_t$  is the torque constant, and  $K_b$  is the back-EMF constant. The transfer function  $D(z)$  was chosen to be a Proportional-Integral (PI) controller. The controller was designed by simulating the step input response of a continuous-time version of Fig. 2.14 and using MATLAB's `pdtune` function to achieve a critically damped response. The continuous-time  $D(s)$  was then converted to the discrete-time  $D(z)$  using a bilinear approximation (Tustin) discretization method. The feed forward term  $Kff$  was set to 0, and the post-scale factor  $Kg$  was set to 1000 per Quanser's recommendation. The control gains for each joint are listed in Table 2.3.

Table 2.3 : Current Controller Details

<b>Joint</b>	<b>D(z)</b>	<b>Kff</b>	<b>Kg</b>
PS	$\frac{8.03z-1.382}{z-1}$	0	1000
FE	$\frac{18.43z+1.912}{z-1}$	0	1000
RU	$\frac{18.43z+1.912}{z-1}$	0	1000

## 2.5 Comparisons and Discussion

The OpenWrist satisfies all design goals previously outlined for coordinated hand-wrist exoskeletons. A comprehensive comparison between the OpenWrist and other wrist devices as compared to ADL (values taken from [25]) is given in Table 2.4 at the end of the chapter. The OpenWrist exceeds the requirements of ADL in both ROM and torque output. Additionally, ROM for each joint is comparable with other devices, all of which (except the RiceWrist) would be considered highly dexterous robots. Torque output is slightly higher than all other devices for all joints.

Fig. 2.15 summarizes the major improvements the OpenWrist makes over its predecessor the RiceWrist-S. The introduction of an open PS design makes donning and doffing for impaired users feasible and ergonomics are also addressed with the addition of an adjustable foam padded elbow support (Fig. 2.15-b) and 30° angled grip for standalone mode. Additional practical improvements allowing for rapid maintenance and ambidextrous reconfiguration enhance its effectiveness in a clinical setting.

Compatibility with the Maestro hand-exoskeleton is insured by eliminating obtrusive geometry present in the RiceWrist-S (Fig. 2.15-e), and relocating the RU module (2.15-f) so that grasping motions can occur. A preliminary coupling of the devices



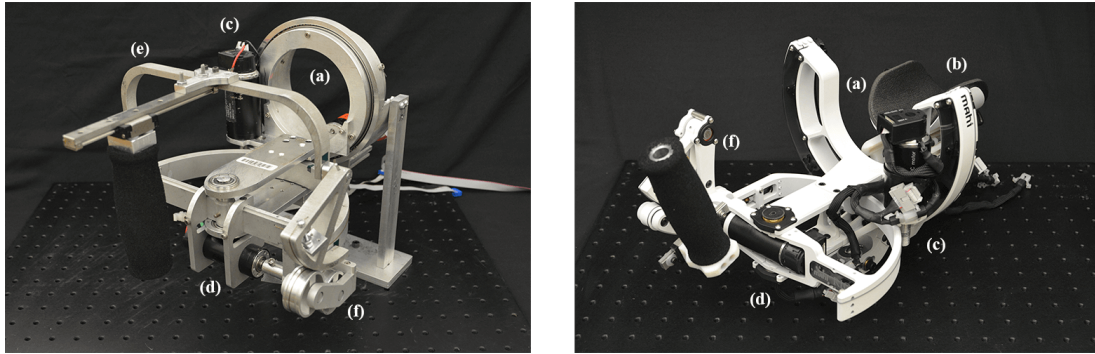


Figure 2.15 : Major design changes between the RiceWrist-S (left) and the OpenWrist (right) – (a) PS joint now open, (b) padded elbow support introduced, (c) FE actuator moved to palmar side, (d) RU actuator moved closer to PS axis, (e) RU bridge eliminated to minimize interference with Maestro, (f) RU module moved to dorsal side.

is shown in Fig. 2.16. In reference to Fig. 2.16-a, no geometry of the OpenWrist interferes with the Bowden cable transmission of the Maestro. Furthermore, the new open design of the PS module allows for the Maestro to be donned before entering the OpenWrist. Fig. 2.16-b illustrates how the relocation of the RU module (top) will enable grasping motions. Also note the ample clearance between the Maestro finger links and the RU module.

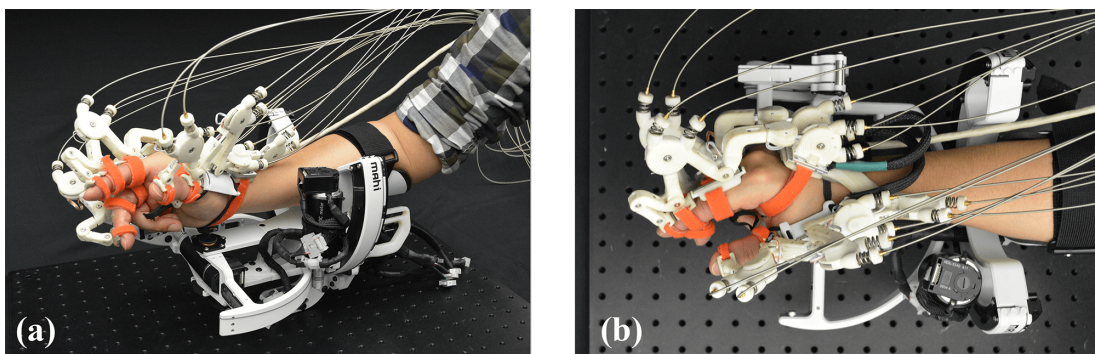


Figure 2.16 : MAHI OpenWrist exoskeleton module shown with the ReNeu Maestro hand exoskeleton module in the combined READAPT configuration.

Table 2.4 : Range of motion (ROM) and torque output of the OpenWrist compared with activities of daily living (ADL) and other wrist devices including the MIT-Manus (MIT) [3], RiceWrist (RW) [4], RiceWrist-S (RW-S) [5], Wrist Gimbal (WG) [6], and IIT Wrist Robot (IIT) [7].

<b>Range of Motion [deg]</b>							
<b>Joint</b>	ADL	MIT	IIT	WG	RW	RW-S	OpenWrist
PS	150	140	160	180	180	180	170 (85 P, 85 S)
FE	115	120	144	180	65	130	135 (70 F, 65 E)
RU	70	75	72	60	63	75	75 (35 R, 40 U)
<b>Max Continuous Torque [Nm]</b>							
<b>Joint</b>	ADL	MIT	IIT	WG	RW	RW-S	OpenWrist
PS	0.06	1.85	2.77	2.87	2.75	1.69	3.50
FE	0.35	1.43	1.53	1.77	1.45	3.37	3.60
RU	0.35	1.43	1.63	1.77	1.45	2.11	2.30

## Chapter 3

# Characterization as a Training Device

In this chapter, I present the experimental characterization of the OpenWrist including estimates of position bandwidth, static and kinetic friction, viscous damping coefficients, and inertial elements. Three separate experiments were performed: a position step input experiment, a position ramp input experiment, and a Schroeder multisine excitation signal experiment. Each of the experiments was performed on all three joints. For consistency, the specific characterization experiments conducted match those previously used for our group’s devices [4, 5, 57] with some slight modifications.\*

### 3.1 Experimental Setup

To eliminate gravitational disturbances, a custom fixture was used to orient the device such that the axis of the joint in question was parallel with the direction of gravity (see Fig. 3.1). The levelness of the joint axis was ensured using a precision electronic level. The remaining two joints were locked in their neutral position with a physical pin and/or high proportional gain PD controller. The passive linear DOF at the base of the grip was secured in the center of its ROM.

---

\*Portions of this chapter originally appeared in a paper submitted by Pezent, Rose, Desphande, and O’Malley in April 2017 [54]. Here, the work is expanded to include new commentary and additional figures.

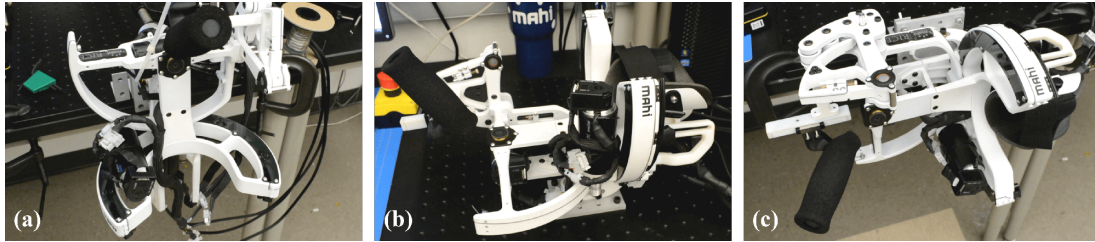


Figure 3.1 : Characterization experimental setups. In each case, the joint in question is parallel to gravity and the remaining joints are locked in their neutral position with a PD controller. For FE and RU experiments, the PS joint was also pinned with a dowel rod. (a) Setup for PS joint experiments. (b) Setup for FE joint experiments. (c) Setup for RU joint experiments.

### 3.2 Step Input Experiment: Inertia, Viscous Damping, and Kinetic Friction

The dynamic properties of the device were investigated by adopting the model and logarithmic decrement techniques first described in [58], and subsequently used in the characterization of other rehabilitation robotic devices [4, 8, 57, 59]. The translational mass-spring-damper system described in [58] is first recast as its rotational equivalent:

$$J\ddot{\theta} + b\dot{\theta} + k\theta + f(\dot{\theta}) = 0 \quad (3.1)$$

where  $f(\dot{\theta})$  is the dry friction, or kinetic Coulomb friction, modeled as

$$f(\dot{\theta}) = f_k \text{sign}(\dot{\theta}) \quad (3.2)$$

By examining the step response of the underdamped system and having prior knowledge of the mechanical stiffness  $k$ , the inertial ( $J$ ), viscous damping coefficient ( $b$ ), and dry friction ( $f_k$ ) contributions to exponential decay can be isolated.

Since each joint in the OpenWrist displays effectively zero mechanical stiffness, the joint actuator's PD controller was set to behave as a relatively soft spring, i.e.  $K_p > 0$  and  $K_d = 0$  (exact gain values used are provided in Table 3.1). Thus, the

equivalent stiffness and viscous damping of each joint was:

$$k = k_{\text{mech}} + K_p = K_p \quad (3.3)$$

$$b = b_{\text{mech}} + K_d = b_{\text{mech}} \quad (3.4)$$

Table 3.1 : Step Input Experiment PD Control Gains

Joint	Joint Free		Joint Locked	
	$K_p$ [ $\frac{\text{Nm}}{\text{rad}}$ ]	$K_d$ [ $\frac{\text{Nm}\cdot\text{s}}{\text{rad}}$ ]	$K_p$ [ $\frac{\text{Nm}}{\text{rad}}$ ]	$K_d$ [ $\frac{\text{Nm}\cdot\text{s}}{\text{rad}}$ ]
PS	15	0	450	0.75
FE	5	0	450	0.75
RU	8	0	50	0.25

For each joint, a square wave position input with a step-to-step amplitude of  $20^\circ$  was commanded, and 3 complete cycles were recorded. To cover most of the joint workspace, the test was conducted about starting joint angles of  $-50^\circ$ ,  $0^\circ$ ,  $50^\circ$  for PS;  $-30^\circ$ ,  $0^\circ$ ,  $30^\circ$  for FE; and  $-5^\circ$ ,  $0^\circ$ ,  $5^\circ$  for RU. Representative plots of the responses for each joint when starting at  $0^\circ$  are shown in Fig. 3.2. Note that the responses for the non-zero starting angles are essentially identical to the  $0^\circ$  starting angle in all cases.

Peaks and valleys were extracted from the underdamped response separately for both the top and bottom response of each cycle for each starting angle. Each set of successive peaks and valleys define a vector of extrema

$$Y = \begin{bmatrix} Y_0 & Y_1 & \cdots & Y_{n_p+n_v-2} & Y_{n_p+n_v-1} \end{bmatrix} = \begin{bmatrix} p_1 & v_1 & \cdots & p_{n_p} & v_{n_v} \end{bmatrix} \quad (3.5)$$

where  $p_i$  and  $v_i$  are the  $i$ th peak and valley, respectively, and  $n_p$  and  $n_v$  are the number of peaks and valleys, respectively. Next, an intermediate quantity  $\beta$  is estimated for

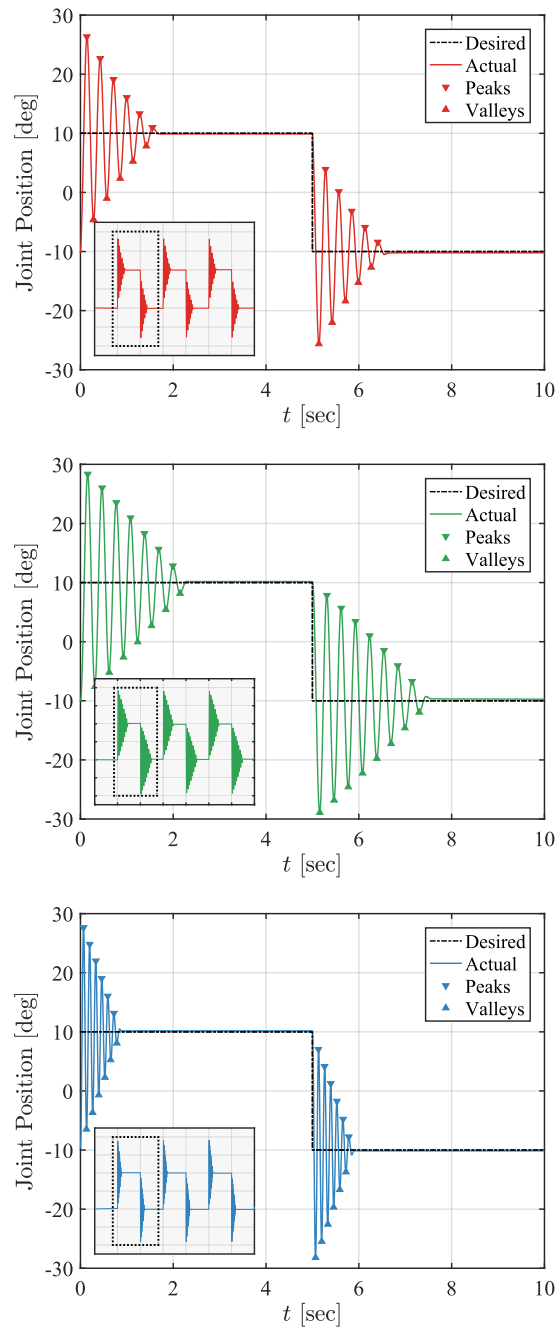


Figure 3.2 : Representative step input responses for PS (top), FE (middle), and RU (bottom), when starting about  $0^\circ$ . Note that only one cycle from the response is shown; all three cycles are shown in the inlaid plot.

each set of four consecutive extrema using the decrement equation

$$\beta = -\frac{1}{\pi} \log\left(-\frac{Y_{i+1} - Y_{i-1}}{Y_i - Y_{i-2}}\right) \quad (3.6)$$

Once  $\beta$  is calculated, an estimate of the system's damping ratio  $\zeta$  is given by:

$$\zeta = \sqrt{\beta^2/(\beta^2 + 1)} \quad (3.7)$$

Equating 3.1, substituted with 3.3 and 3.4, with the typical characteristic equation for a second-order system yields equations for estimating the joint inertia and viscous damping coefficient:

$$J = K_p/\omega_n^2 \quad (3.8)$$

$$b_{mech} = 2J\zeta\omega_n \quad (3.9)$$

where  $\omega_n = w_d/\sqrt{1 - \zeta^2}$ ,  $\omega_d = 2\pi/T$ , and  $T$  is the period between successive peaks (or successive valleys). Finally, the dry kinetic friction is estimated with:

$$f_k = x_k K_p \quad (3.10)$$

where

$$x_k = \frac{Y_{i+1} - Y_i + e^{-\beta\pi}(Y_i - Y_{i-1})}{2(-1)^i(e^{-\beta\pi} + 1)} \quad (3.11)$$

Values for the joint's inertia  $J$ , viscous damping coefficient  $B$ , and kinetic dry friction  $f_k$  were averaged across all responses and starting angles, as reported in Table 3.2.

To validate the accuracy of the model, a Simulink model of 3.1 with the averaged parameters and proportional gain constant was used to simulate the response of each joint when input with the same square wave. A representative simulated response for each joint is shown in Fig. 3.3.

Additionally, the estimated inertia values were cross checked with theoretical values from SolidWorks. The theoretical values were obtained by considering the components of the joint in question and all distal joints, i.e, Fig. 2.2-b + Fig. 2.3-a +

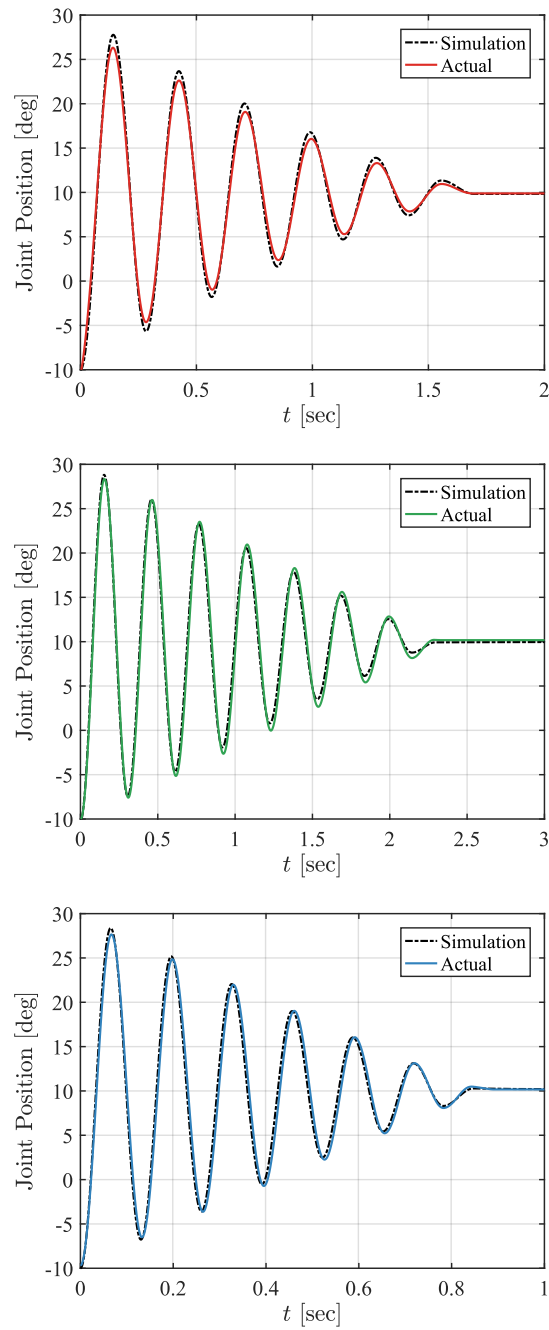


Figure 3.3 : Representative simulated responses compared with the actual responses for PS (top), FE (middle), and RU (bottom). Here, each response is taken from the upper response of the first square wave cycle when starting from  $0^\circ$  (see Fig. 3.2).



Fig. 2.4-a for the PS joint; Fig. 2.3-a + Fig. 2.4-a for the FE joint; and Fig. 2.4-a for the RU joint. The rotor inertia (as obtained from the motor data sheet) that is reflected from each joint’s actuator through the capstan transmission was calculated and added to the inertia values obtained from Solidworks. The theoretical inertia values are provided in Table 3.2.

Table 3.2 : Step Input Experiment Results

<b>Joint</b>	<b>Inertia (Exp.)</b>	<b>Inertia (SW)</b>	<b>Viscous Coeff.</b>	<b>Kinetic Friction</b>
	[kg · m <sup>2</sup> ]	[kg · m <sup>2</sup> ]	[ $\frac{\text{Nm}\cdot\text{s}}{\text{rad}}$ ]	[Nm]
PS	0.0305	0.0301	0.0252	0.1891
FE	0.0119	0.0123	0.0019	0.0541
RU	0.0038	0.0038	0.0029	0.1339

### 3.3 Ramp Input Experiment: Static Friction

To investigate static friction, multiple position ramps were commanded across the workspace of each joint. The input ramps up or down 5° over 2 seconds, pauses for an additional 2 seconds, and then continues ramping in this manner until the extreme points of the workspace have been reached (see Fig. 3.4). Since subtle changes in velocity were more important than accurate position control, a soft proportional controller was used (see Table 3.3). Static friction is inferred from the commanded torque when movement is initiated, i.e., one time step before the instant the backwards-differentiated velocity becomes non-zero near the beginning of each ramp. Static friction as a function of joint workspace is shown in Fig. 3.5, with average and max values highlighted in Table 3.4.

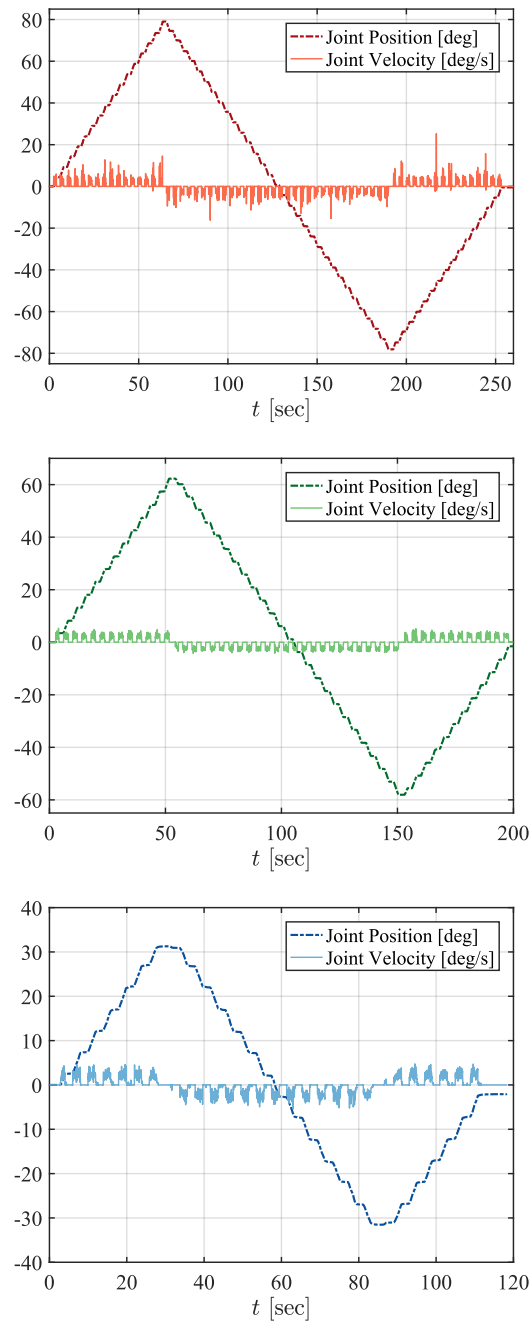


Figure 3.4 : Ramp input position and velocity responses for PS (top), FE (middle), and RU (bottom).

Table 3.3 : Ramp Input Experiment PD Control Gains

Joint	Joint Free		Joint Locked	
	$K_p$ [ $\frac{Nm}{rad}$ ]	$K_d$ [ $\frac{Nm\cdot s}{rad}$ ]	$K_p$ [ $\frac{Nm}{rad}$ ]	$K_d$ [ $\frac{Nm\cdot s}{rad}$ ]
PS	5	0	450	0.75
FE	3	0	450	0.75
RU	2	0	50	0.25

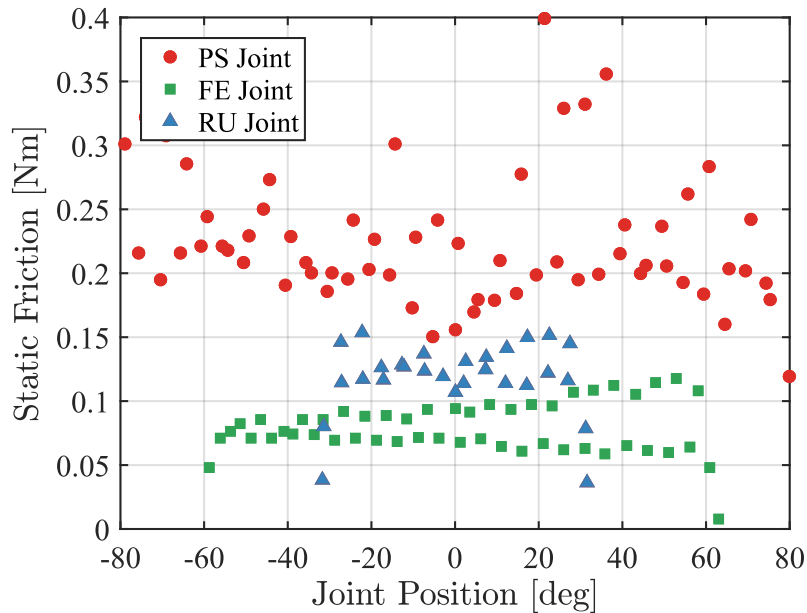


Figure 3.5 : Static friction of the PS, FE, and RU joints taken during the ramp test and plotted along their respective workspaces.

### 3.4 Schroeder Multisine Input Experiment: Closed-Loop Position Bandwidth

It is important to determine the closed-loop position bandwidth since the device may employ a position control strategy in the future. A critically damped PD controller was implemented, and a Schroeder multisine excitation signal conditioned between

Table 3.4 : Ramp Input Experiment Results

<b>Joint</b>	<b>Avg. Static Friction [Nm]</b>	<b>Max Static Friction [Nm]</b>
PS	0.2250	0.3990
FE	0.0720	0.1042
RU	0.1180	0.1537

-10° and 10° was used as the position input. A Schroeder-phased multisine is the sum of sinusoids where phases are chosen to minimize peak-to-peak amplitudes [60]. The input signal is defined by

$$u_m(t) = \sum_{k=1}^N A_m \cos(2\pi\omega_k t + \phi_k) \quad (3.12)$$

where

$$N \triangleq \frac{\omega_{max} - \omega_{min}}{\eta} + 1, \quad (3.13)$$

$A_m \in \mathbb{R}$  and, for  $k = 1, \dots, N$ ,

$$\phi_k \triangleq \frac{-k(k-1)\pi}{N}, \quad (3.14)$$

$$\omega_k \triangleq \omega_{min} + \eta(k-1) \quad (3.15)$$

Fig. 3.6 shows the plots of the commanded versus actual positions for all three joints, with attenuation beginning around the 10 second mark for each. Fig. 3.7 provides the Bode plot for each DOF with the bandwidth cutoff of 3 dB clearly shown.

### 3.5 Comparisons and Discussion

A comprehensive comparison between the OpenWrist and previous MAHI devices is provided at the end of this chapter in Table 3.6. Characterization of the OpenWrist

Table 3.5 : Schroeder Wave Input Experiment PD Control Gains

Joint	Joint Free		Joint Locked	
	$K_p$ [ $\frac{Nm}{rad}$ ]	$K_d$ [ $\frac{Nm\cdot s}{rad}$ ]	$K_p$ [ $\frac{Nm}{rad}$ ]	$K_d$ [ $\frac{Nm\cdot s}{rad}$ ]
PS	25	1.15	450	0.75
FE	24	0.80	450	0.75
RU	11.5	0.25	50	0.25

underscores the significance of the numerous design considerations likely to improve its potential as a rehabilitative device. The model from [58] captures the dynamic properties with reasonable accuracy despite its simplicity (Fig. 3.3). Furthermore, the estimated inertia for each joint agrees with values taken from the Solidworks model (Table. 3.2). Compared with its predecessor, the RiceWrist-S, inertia reductions of 12% and 21% are achieved in the FE and RU joints, respectively, as a result of lower weight components and strategically placed actuators. Hybrid-ceramic ball bearings and improved capstan-cable windings contribute to decreases in maximum static friction by 47% in FE and 27% in RU. The separation of FE static friction measurements shown between 40° and 60° in Fig. 3.5 suggests that the test was affected by gravity. The effect remained repeatable despite multiple attempts to eliminate it and is likely an outcome of the FE module’s asymmetric design. The inconsistent static friction at the extremes of the RU workspace are explained by a build-up and release of cable tension during directional changes near the edges.

Although the curvilinear rails resulted in increased inertia and static friction in the PS joint, the open design is of far greater importance. Note the periodic spikes in PS static friction shown in Fig. 3.5; these spikes roughly correlate with the gaps

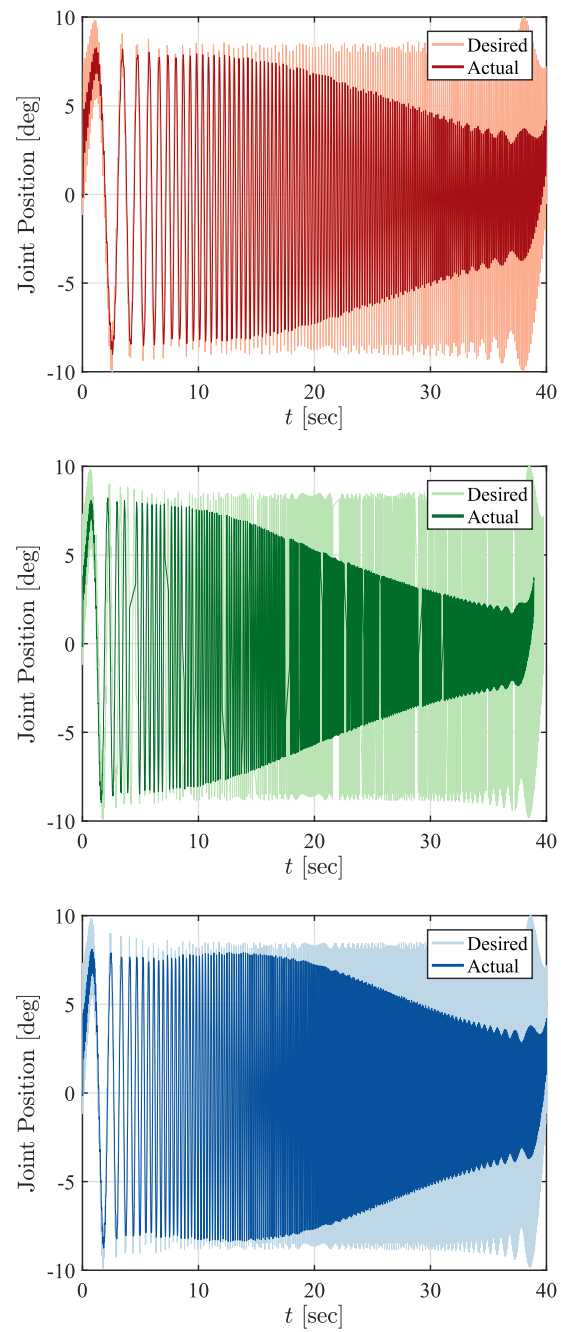


Figure 3.6 : Schroeder multisine input responses for PS (top), FE (middle), and RU (bottom). The input excites the joint through a range of increasing frequencies.

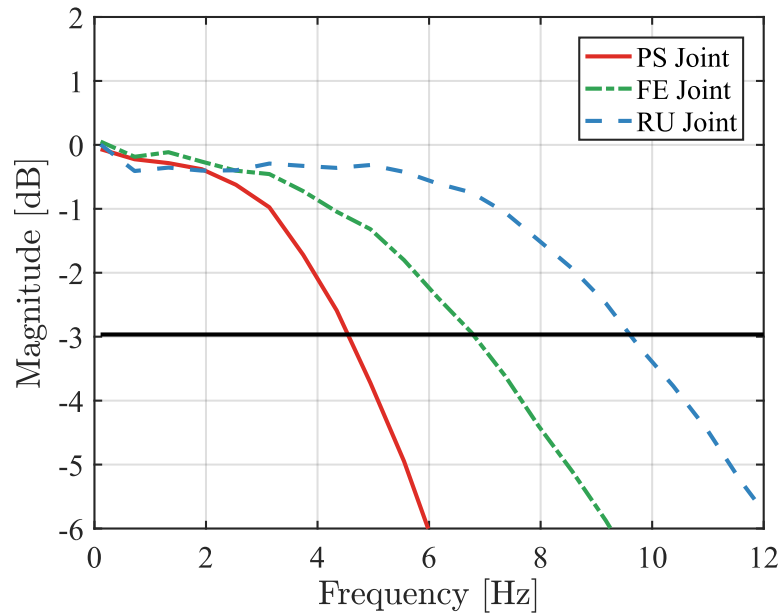


Figure 3.7 : Bode plots obtained by estimating the transfer function of Fig 3.6. Bandwidth values, defined by the -3 dB cutoff, are 4.7, 7.0, and 9.8 Hz for the PS, FE, and RU joints, respectively.

between the four rail segments. Thus, the high static friction value is likely due to a slight misalignment of the rails. This issue can be expected to improve with continued adjustment and break-in. Furthermore, because torque output on the PS joint has been doubled, any undesired effects of increased inertia and friction can be compensated for in control implementation.

Kinetic friction values measured for the OpenWrist consume a maximum of only 6% of the continuous torque output in any joint. Closed-loop position bandwidth is increased over the RiceWrist-S across the board and either exceeds or is slightly less than the 5 Hz achievable by humans in uncontrolled motions [61].

Table 3.6 : Average device characteristics for the MAHI RiceWrist (RW) [4], RiceWrist-S (RW-S) [8], and OpenWrist wrist exoskeletons.

<b>Joint</b>	<b>Inertia</b> [kg · m <sup>2</sup> ]			<b>Viscous Coefficient</b> [ $\frac{\text{Nm}\cdot\text{s}}{\text{rad}}$ ]		
	RW	RW-S	OpenWrist	RW	RW-S	OpenWrist
PS	0.0257	0.0258	0.3050	0.0167	0.428	0.0252
FE	0.0020	0.0134	0.0119	0.0283	0.085	0.0019
RU	0.0033	0.0048	0.0038	0.0225	0.135	0.0029
<b>Joint</b>	<b>Kinetic Friction</b> [Nm]			<b>Static Friction (Max)</b> [Nm]		
	RW	RW-S	OpenWrist	RW	RW-S	OpenWrist
PS	n/a	n/a	0.1891	n/a (0.139)	n/a (0.221)	0.2250 (0.3990)
FE	n/a	n/a	0.0541	n/a (0.109)	n/a (0.198)	0.0720 (0.1042)
RU	n/a	n/a	0.1339	n/a (0.112)	n/a (0.211)	0.1180 (0.1537)
<b>Joint</b>	<b>Bandwidth</b> [Hz]					
	RW	RW-S	OpenWrist			
PS	4.2	3.5	4.6			
FE	13.3	6.0	7.0			
RU	10.6	8.3	9.8			



## Chapter 4

### Validation as an Assessment Device

Often, rehabilitation robots that are used as training devices are also used as assessment devices. Typically it is assumed that the robot has a negligible impact on the measurements required to compute assessment metrics such as movement smoothness. However, this has been shown to not always be true [1]. To validate a rehabilitation robot as an assessment device, a direct comparison between movements performed in the device and movements in a no-robot condition must be performed.

The chapter is divided into three separate studies. The first, a small single-subject pilot study, compares velocity profiles between the OpenWrist and its predecessor, the RiceWrist-S, to investigate the impact of the numerous design upgrades made (see Chapter 2). The second study, a larger multi-subject study, compares metrics for movement smoothness between robot and no-robot conditions in an effort to validate the OpenWrist as an assessment device. Finally, the third study, similar in scope to the second, seeks to understand what impact dynamic properties, particularly inertia and friction, have on movement smoothness. I would like to acknowledge my collaborators Andrew Erwin, Josh Bradley, Chad Rose, and Claudia Kahn, each of whom played an instrumental role in the two subject studies.\*

---

\*Portions of this chapter originally appeared in a paper submitted by Erwin, Pezent, Bradley and O'Malley in April 2017 [52].

## 4.1 Pilot Study: RiceWrist-S vs. OpenWrist in Wrist Pointing Velocity Profiles

A pilot investigation sought to compare the velocity profiles of wrist pointing movements performed in both the OpenWrist and its predecessor, the RiceWrist-S. Given the numerous design changes introduced to increase device transparency in the OpenWrist, one would expect smoother and more uniform velocity profiles in the OpenWrist. A single male subject was instructed to make wrist pointing movements along the traditional anatomical axes (FE and RU) as well as in two "diagonal" directions, D1 and D2, that required coordinated movements along both the FE and RU axis. It is important to note that D1 and D2 are not exactly midway between the FE and RU axes; D1 is composed of slightly more FE movement, while D2 is composed of slightly more RU movement. Twenty-four movements were performed along each of the four axes. While the OpenWrist has the ability to record joint velocity directly from encoders, the RiceWrist-S does not. Therefore, joint velocities for both robots were estimated by taking the approximate derivative of joint positions and filtering with a first-order Butterworth filter. The estimated velocity in the FE and RU axes were used to calculate the task space tangential velocity of each movement. Velocities, normalized in both magnitude and duration, are shown in Fig. 4.1. Irrespective of computing smoothness metrics, it is clear that the OpenWrist makes drastic improvements toward decreasing the device's affect on wrist pointing smoothness. This is especially true for the RU and D2 axes where the expected bell-shaped profile is barely visible for the RiceWrist-S.

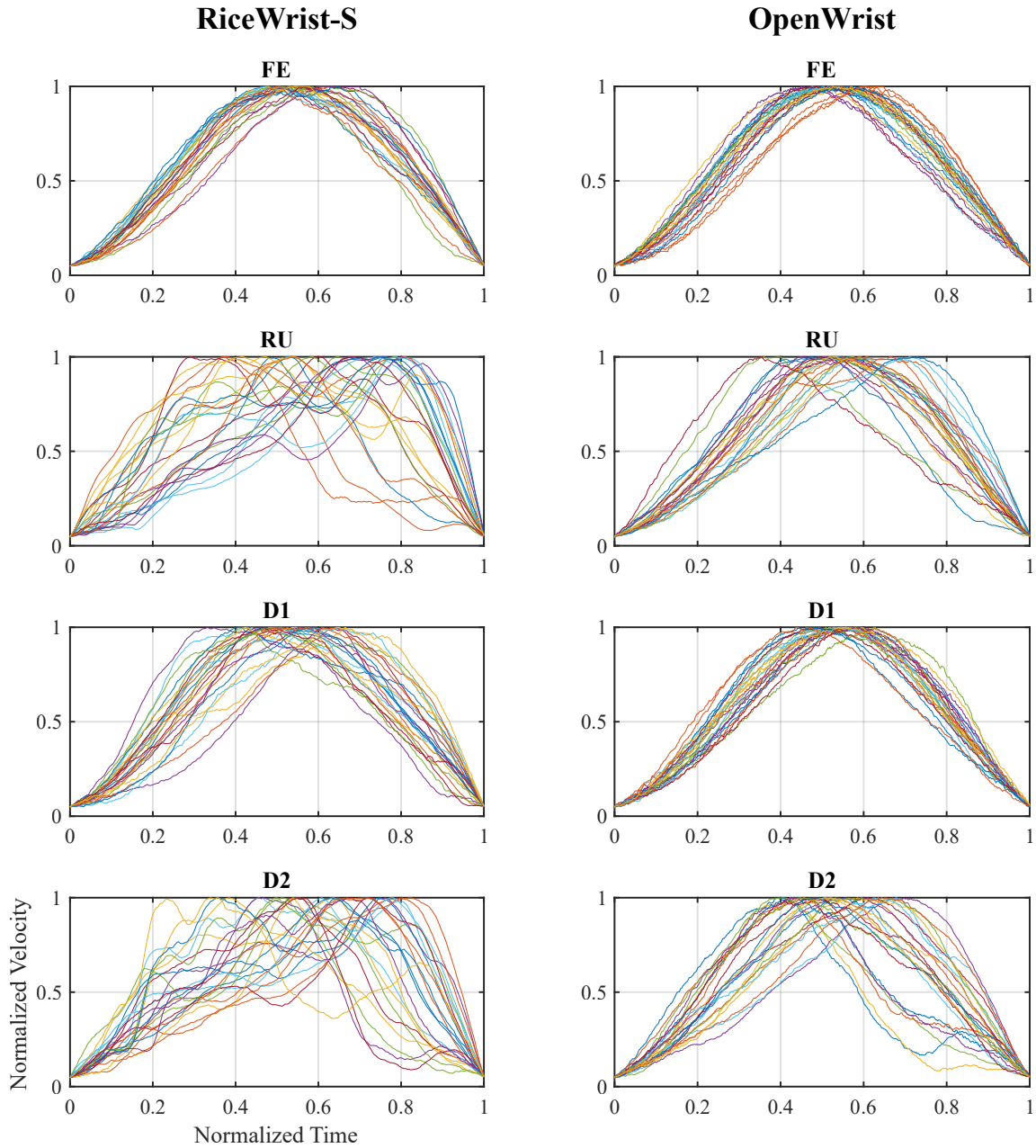


Figure 4.1 : Velocity profiles for the RiceWrist-S (left) and OpenWrist (right) in the four task-space directions tested.

## **4.2 Subject Study A: Wrist Pointing Movements for Robot vs. No Robot Conditions**

The improvement of movement smoothness over the course of therapy is one of the positive outcomes observed during robotic rehabilitation and is widely used as an assessment metric for evaluating therapeutic progress. To validate a rehabilitation robot as an accurate assessment device, a direct comparison between movements performed with and without the robot must be considered. In this section, two smoothness metrics are evaluated in a no-robot and robot condition to see what impact the robot has on these metrics. Since the no-robot condition obviously lacks the convenience of robotic joint encoders, passive marker motion capture was used to record anatomical joint angles for both the robot and no-robot conditions.

### **4.2.1 Methods**

#### **Subjects**

Nine subjects (2 female, 7 male), ages 20-28 years old participated in the experiment. All subjects were right hand dominant with no current injury or known history of neuromuscular injury in their wrist. Approval for the experiment was obtained through the Rice University Institutional Review Board.

#### **Task Description**

The experiment consisted of two blocks. The task performed in both blocks was identical except in the first block the subject performed the task in the no-robot condition (Fig. 4.2-a), and in the second block the subject performed the task in the robot condition (Fig. 4.2-b).

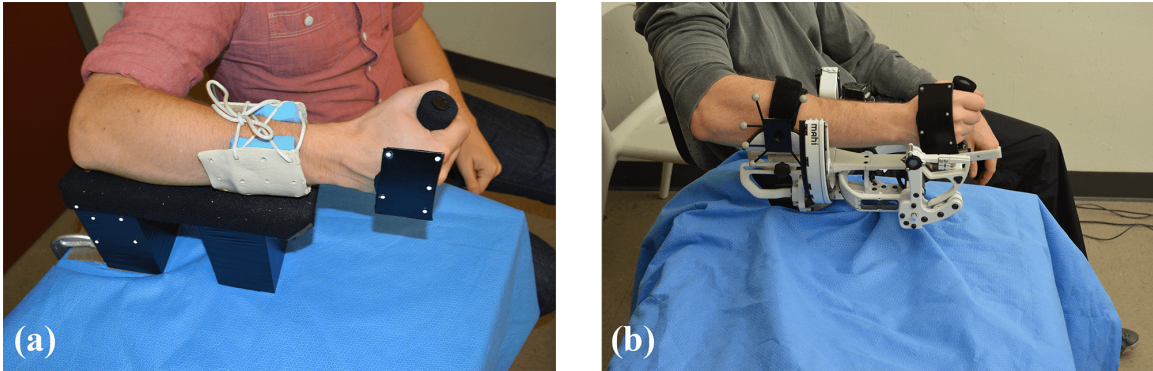


Figure 4.2 : Conditions of subject study A. **(a)** Subject in the no-robot condition. The forearm was secured through a rigid splint that could be compressed with a tied lace. **(b)** Subject in the robot condition. The forearm is secured to the adjustable forearm rest of the OpenWrist, itself secured to the platform below it.

Subjects performed a wrist pointing task, similar to the tasks presented in [46, 62]. The task required wrist pointing to nine targets – one centrally placed and 8 radially placed, shown in Fig. 4.3. Starting at the central target, subjects were instructed to reach an indicated outer target before a gate closed around it (as in Fig 4.3-b). Upon reaching the outer target, the subject was then directed back to the central target, and the process was repeated for a new outer target. Three sessions occurred: 1) a practice session with 5 reaches per outer target, 2) a "slow" (0.6 s gate closing time) session with 15 reaches per outer target, and 3) a "fast" (0.4 s gate closing time) session with 15 reaches per outer target. Targets were presented in a pseudo-random order, and subjects were instructed to pause on all targets for one second to improve velocity based segmentation in post-processing.

While the visualization indicated an evenly spaced circular mapping, the true mapping was chosen to reflect a constant portion of the ROM, not a constant angular distance (see Fig. 4.4). Target locations were chosen by reducing the average wrist ROM defined in [2] by 40% and distributing targets around the perimeter in  $45^\circ$  increments. The robot was used purely in an underpowered backdrive mode.

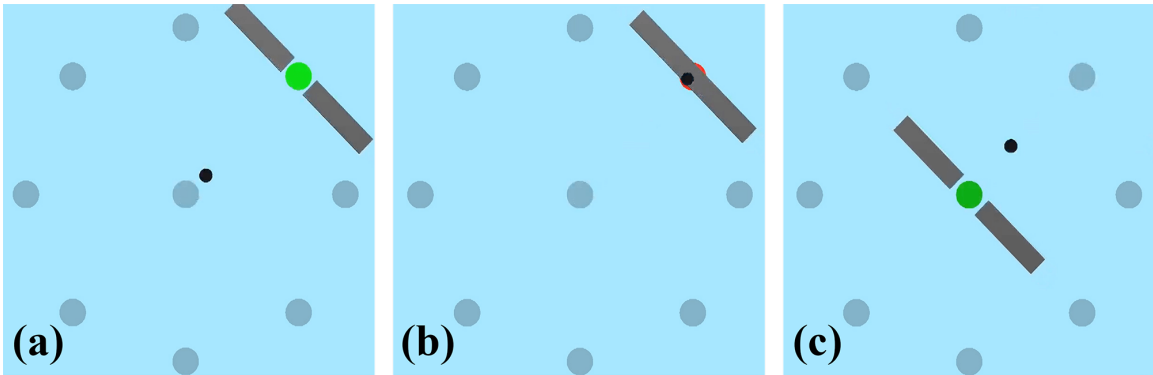


Figure 4.3 : The real-time visual display used during the task of subject study A. The small black dot is the subject's cursor and current position, and the large gray dots are the targets. The subject moves to a new target when it turns green, at a speed suggested by the closing of a rectangular gate around the target.

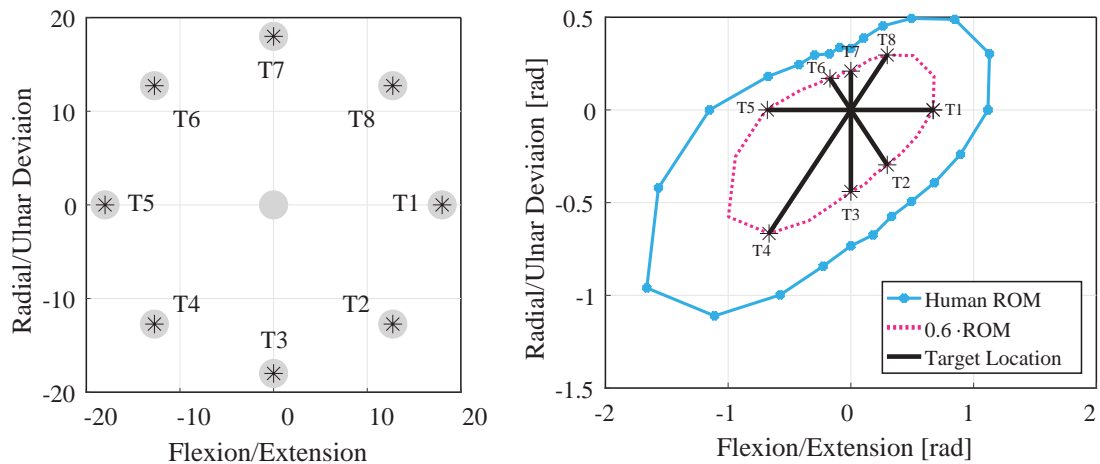


Figure 4.4 : The presented joint angle visualization (left) and the actual joint angle mapping (right) that was chosen to reflect a constant portion of the ROM. Target locations were chosen by reducing the average wrist ROM defined in [2] by 40% and distributing targets around the perimeter in  $45^\circ$  increments.

### Joint Angle Measurement

Anatomical wrist angles were measured with a six-camera Optitrack Flex V100R2 100 FPS motion capture system. Passive markers (3 mm and 11 mm) were used to create reference rigid bodies, one placed on the forearm, and another placed on the dorsal side of the hand (Fig. 4.5). The algorithm given in [63] was used to

estimate the anatomical wrist rotations. The algorithm takes the orientation of the two rigid bodies relative to the motion capture world frame and estimates axes of rotation based on calibrated single DOF movements. The orientation of the axis is obtained by minimizing the integral

$$\Delta\omega = \frac{1}{t} \int_0^t (R_1\omega_1 - R_2\omega_2)^2 dt \quad (4.1)$$

where  $t$  is the time of the movement,  $R_1$  and  $R_2$  are the orientation of the rigid bodies relative to the world frame, and  $\omega_1$  and  $\omega_2$  are the orientations of the axes relative to the rigid bodies. Taking the partial derivative of 4.1 with respect to  $\omega_1$  and  $\omega_2$  the linear system

$$\begin{bmatrix} I & -\int_0^t R_1^T R_2 dt \\ -\int_0^t R_2^T R_1 dt & 1 \end{bmatrix} \begin{bmatrix} \omega_1 \\ \omega_2 \end{bmatrix} = 0 \quad (4.2)$$

The eigenvalue of the matrix in 4.2 with the smallest magnitude corresponds to the axis orientation which minimizes the integral in 4.1. The other axis orientation is obtained by repeating the process for another movement. Taking the cross product of the resultant axes gives a third orthogonal axis, which is then crossed with an anatomic axis to give the orthogonal set of anatomically inspired axes used to determine wrist angles (see Fig. 4.6).

## Data Analysis

**Velocity Segmentation** Anatomical joint angle measurements were filtered and differentiated using a third-order Savitzky-Golay filter with a 21-sample (200ms) window [64]. Velocity data of the FE and RU axes were used to calculate the task space tangential velocity of each movement. This velocity data was first trimmed using a window larger than that of the expected movement time to account for variability in subject's movement timing. As in [46,62], these velocity profiles were then segmented

by only keeping velocity starting and ending with the condition  $|v(t^*)| > 0.05 \cdot |v_{max}|$  where  $v_{max}$  is the maximum velocity for the movement.

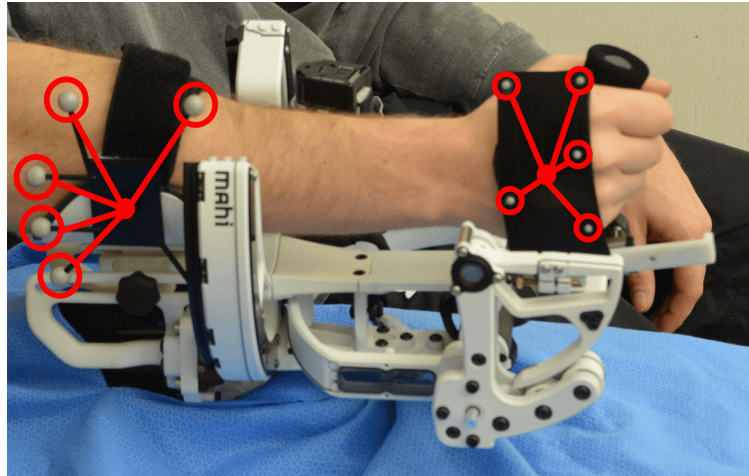


Figure 4.5 : Two rigid bodies (red) defined by the motion capture markers.

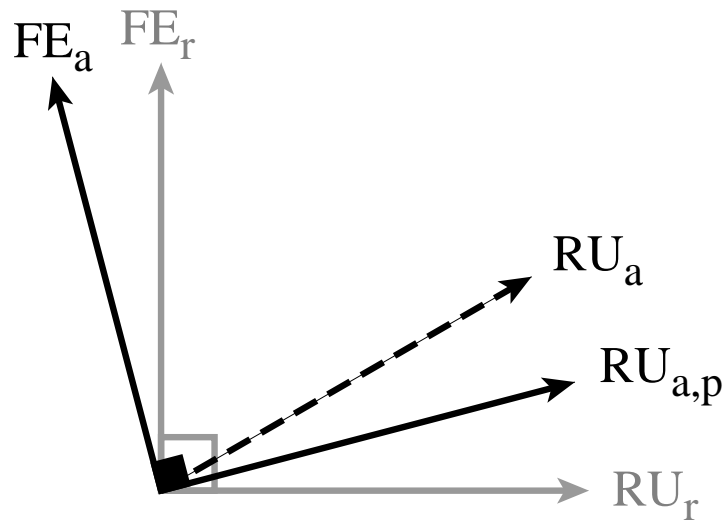


Figure 4.6 : Illustration of the 3D calibrated, anatomically inspired axes. Anatomical and robot axes are indicated with 'a' and 'r' subscripts, respectively, while the orthogonally imposed anatomical RU axis is indicated with 'a'. The axes used for joint measurement are indicated by the solid black lines.



**Movement Smoothness** From the segmented velocity, the movement smoothness correlation coefficient  $\rho$  [65] was calculated as

$$\rho = \frac{\Sigma[(v_s - \bar{v}_s)(v_{mj} - \bar{v}_{mj})]}{\sqrt{\Sigma(v_s - \bar{v}_s)^2 \Sigma(v_{mj} - \bar{v}_{mj})^2}} \quad (4.3)$$

where  $v_s$  is the subject's tangential velocity,  $\bar{v}$  is the mean velocity, and  $v_{mj}$  is the minimum jerk trajectory given by

$$v_{mj} = \Delta \left( \frac{30t^4}{T^5} - \frac{60t^3}{T^4} + \frac{30t^2}{T^3} \right). \quad (4.4)$$

where  $t$  is time,  $\Delta$  is distance traveled, and  $T$  is duration of the movement. The movement smoothness correlation coefficient takes values between 0 and 1, where a value of 1 would indicate perfect correlation with the minimum jerk trajectory, and a value of 0 would indicate no correlation. Occasionally, negative  $\rho$  values were calculated (implying negative correlation) and were set to zero, as in [65].

In addition to  $\rho$ , another movement smoothness metric, *spectral arc length* (SAL) [66], was calculated. The creators of SAL suggest that jerk-based smoothness metrics, like  $\rho$ , lack validity, consistency, sensitivity, or robustness. Particularly,  $\rho$  has been shown to be sensitive to noise and segmentation width. While  $\rho$  computes smoothness in the time domain, SAL uses a movement speed profile's Fourier magnitude spectrum to quantify movement smoothness in the frequency domain. Specifically, SAL is the negative arc length of the amplitude and frequency-normalized Fourier magnitude spectrum of the speed profile. The intuition behind the metric is that smoother movements should have more low-frequency components, while less smooth movements should consist of higher frequency components. The metric is defined as

$$\text{SAL} \triangleq - \int_0^{\omega_c} \sqrt{\left(\frac{1}{\omega_c}\right)^2 + \left(\frac{d\hat{V}(\omega)}{d\omega}\right)^2} d\omega \quad (4.5)$$

$$\hat{V}(\omega) \triangleq \frac{V(\omega)}{V(0)} \quad (4.6)$$

where  $V(\omega)$  is the Fourier magnitude of the speed profile  $v(t)$  and  $[0, \omega_c]$  is the frequency band of the movement. To calculate SAL, a MATLAB function provided by its creators was used with default settings. SAL takes on negative values, with less negative values indicating smoother movements. The original authors have shown that movements made by health subjects typically fall between  $-1.9$  and  $-2.0$ , while impaired subjects fall below  $-3.0$ . Preliminary stroke subject data from clinical trials conducted by MAHI Lab members at TIRR Memorial Herman hospital suggests that severely impaired subjects may have SAL values as low as  $-6.0$ .

#### 4.2.2 Results

Fig. 4.7 shows a representative plot of the task space movement paths generated by a single subject. Fig. 4.8 and Fig. 4.9 provide the mean normalized velocity profiles with standard deviation for the slow and fast trials, respectively. Fig. 4.10 and Fig. 4.11 provide the mean smoothness correlation coefficient  $\rho$  for all subjects, separated by target and condition, for the slow and fast sessions, respectively. Outbound and inbound data have been combined. Likewise, Fig. 4.12 and Fig. 4.13 show SAL for the slow and fast condition, with outbound and inbound data combined.

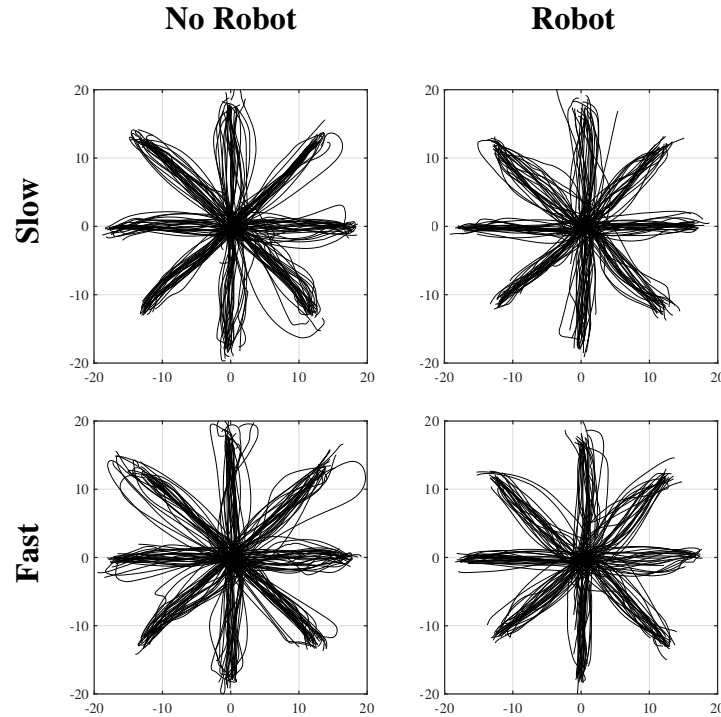


Figure 4.7 : Representative plots of the task space movement paths generated by a single subject. Units on the horizontal and vertical axes correspond with those in the visualization (see Fig. 4.4).

### 4.2.3 Discussion

The data highlights the differences between movements performed in the robot condition and the no-robot condition. For the the smoothness correlation coefficient  $\rho$ , the robot made a major impact. Movements made in the presence of the OpenWrist were considerably more correlated with the minimum jerk trajectory than those made in the no-robot condition for both the the slow and fast sessions. Two important observations can be made. First, targets 1 and 5 for the robot condition are generally the smoothest movements (based on the mean value) and also show the greatest increase over the no-robot condition. These targets corresponds with movements which

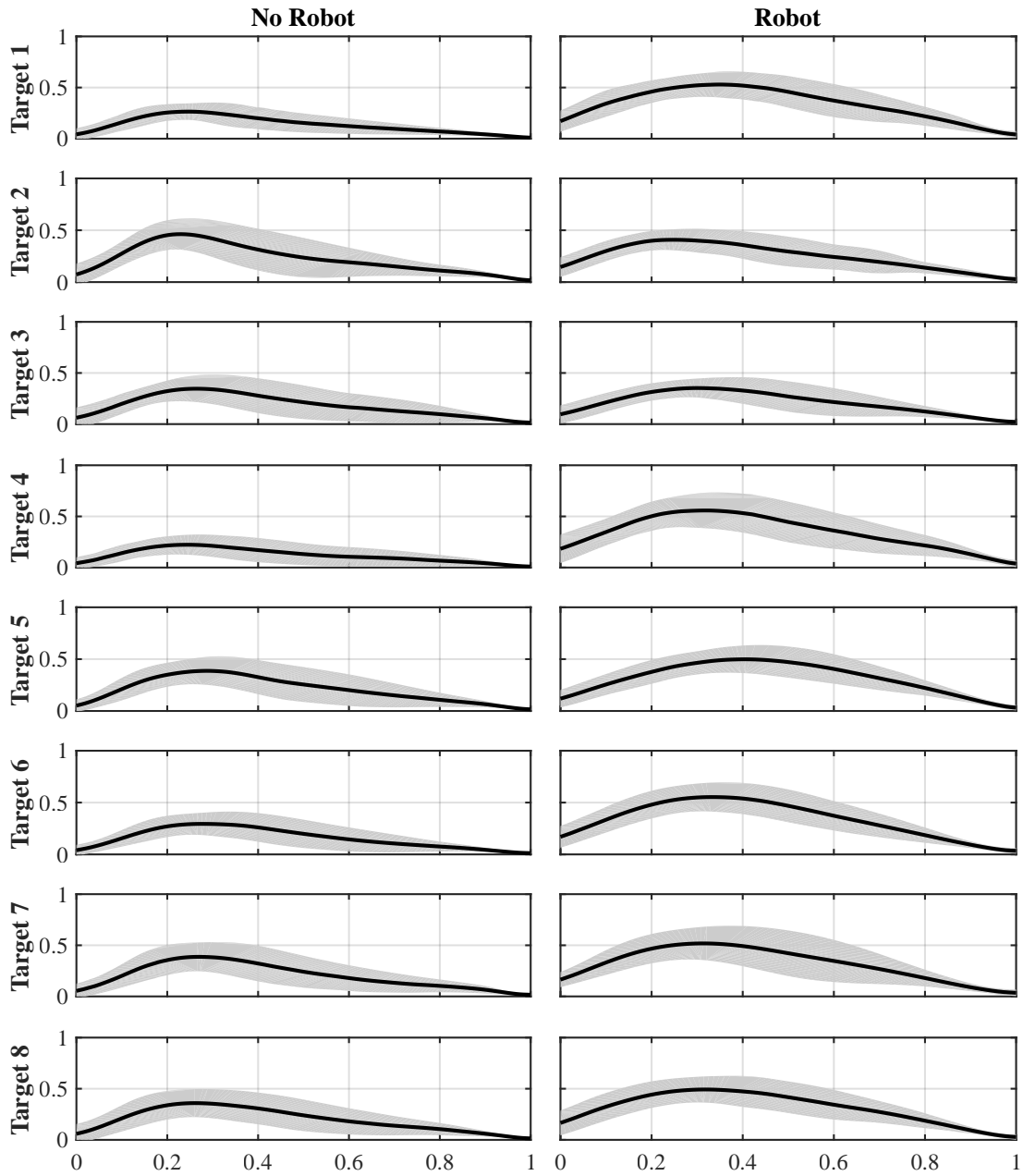


Figure 4.8 : Mean normalized velocity profiles with standard deviation for all subjects during the slow trials.

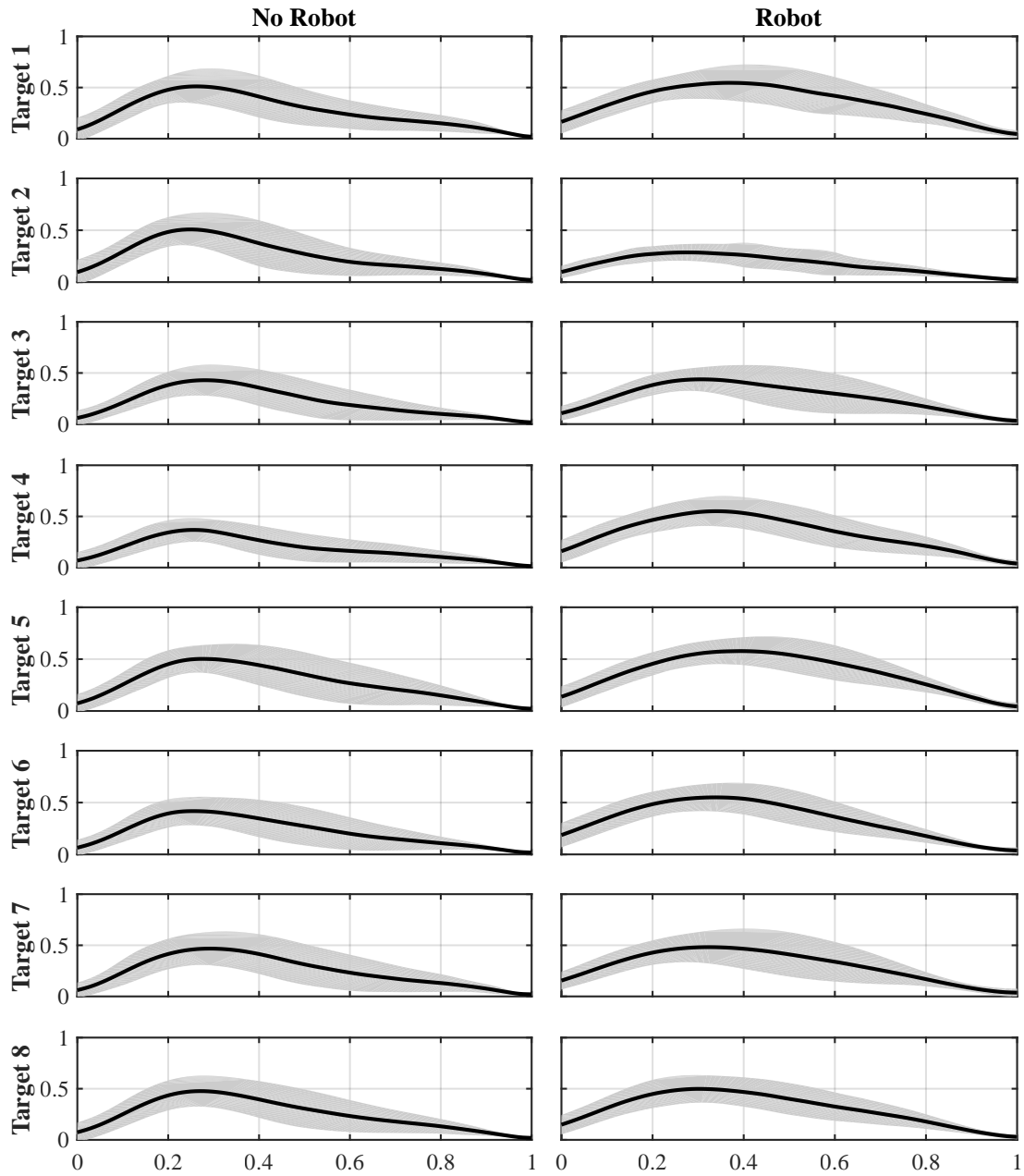


Figure 4.9 : Mean normalized velocity profiles with standard deviation for all subjects during the fast trials.

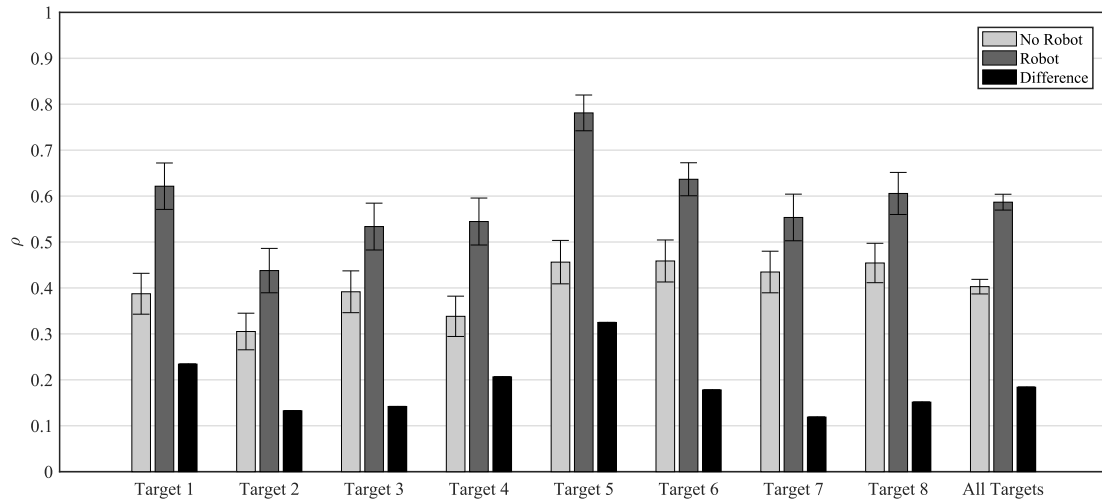


Figure 4.10 : The mean smoothness correlation coefficient,  $\rho$ , for all subjects during the slow trials. Difference is defined as  $\rho_{\text{robot}} - \rho_{\text{no robot}}$ . Error bars are for a 95% confidence interval (1.96 times the standard error).

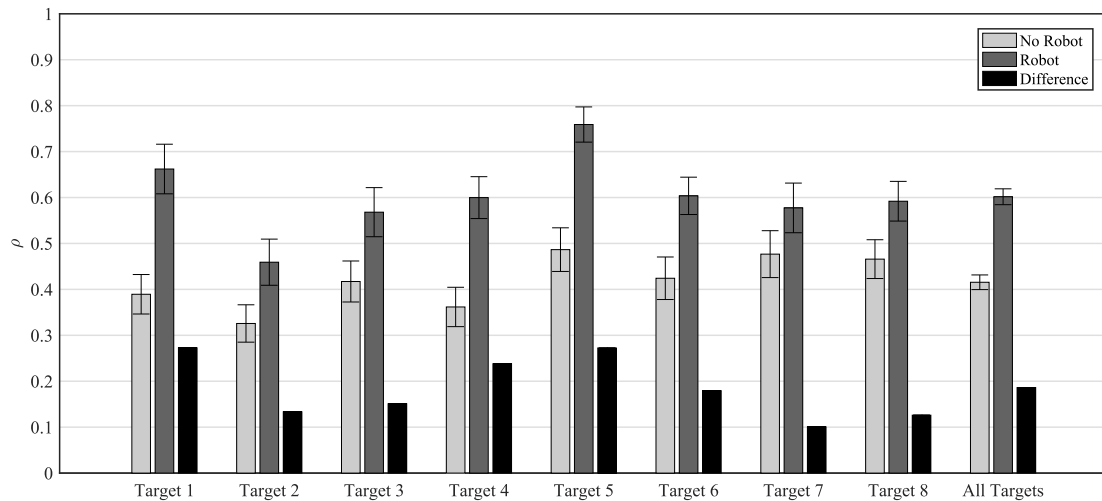


Figure 4.11 : The mean smoothness correlation coefficient,  $\rho$ , for all subjects during the fast trials. Difference is defined as  $\rho_{\text{robot}} - \rho_{\text{no robot}}$ . Error bars are for a 95% confidence interval (1.96 times the standard error).

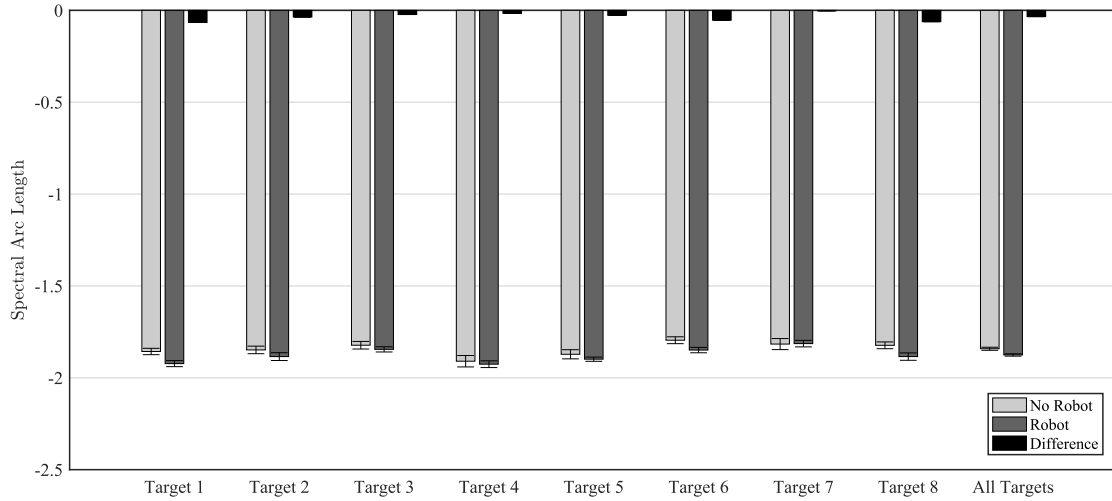


Figure 4.12 : Spectral arc length for all subjects during the slow trials. Difference is defined as  $SAL_{\text{robot}} - SAL_{\text{no robot}}$ . Error bars are for a 95% confidence interval (1.96 times the standard error).

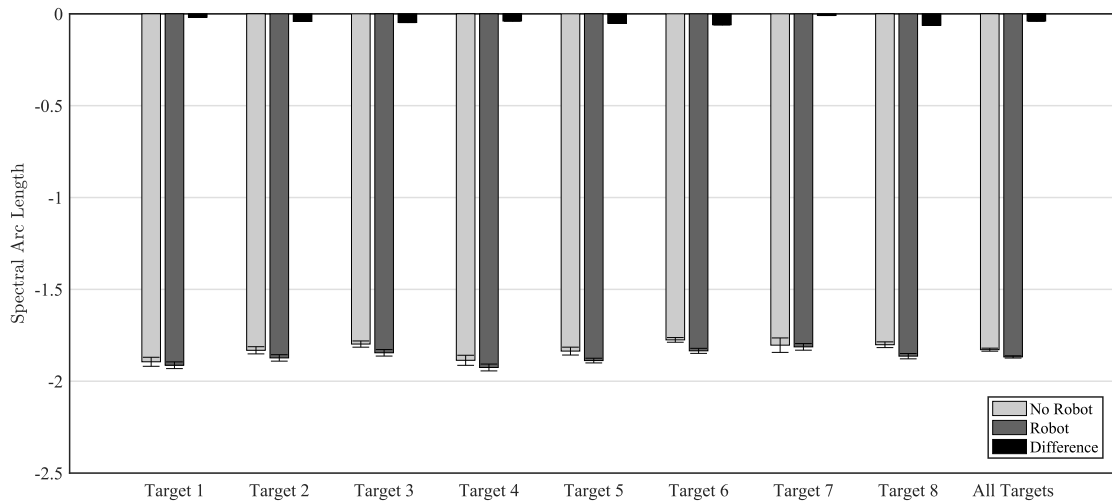


Figure 4.13 : Spectral arc length for all subjects during the fast trials. Difference is defined as  $SAL_{\text{robot}} - SAL_{\text{no robot}}$ . Error bars are for a 95% confidence interval (1.96 times the standard error).

required the most motion on the second robot joint. Second, targets 3 and 7, those which required the most motion on the third robot joint, are the least affected by the robot. Observing Fig. 4.8 and Fig. 4.9, it can be seen that the mean velocity profiles for the robot condition display curvature that is slightly more reminiscent of the minimum jerk profile (see Fig. 4.17 for example), with peak velocities occurring closer to the half-way mark. Two conclusions could be drawn from these observations. First, recall that joint 2's inertia is approximately 10x larger than joint 3's. It is possible that the increased inertial load acts as a mechanical low-pass filter, have a smoothing effect on the movement profile. This would agree with observations of wrist movements in [67], where inertial loads tended to aid movements in following a minimum jerk trajectory. The second possibility is that friction in the robot's third joint, which is higher due to its more complex cable routing mechanism, has a negative impact on smoothness. This may explain why targets 3 and 7 do not experience the same increase in smoothness as targets 1 and 5. This phenomenon is further investigate in Section 4.3. One other observation that can be made for  $\rho$  is the high degree of variability, denoted a relatively large confidence interval. This would agree with the statements made [66], regarding the deficiencies of jerk based smoothness measures.

The bar plots for SAL paint a different picture – movements performed in robot were not significantly different from movements performed outside of the robot. As expected, there is also significantly less variability in SAL compared to  $\rho$ . The values for SAL reported here, around -1.9 for most targets, agree with the values reported in [66] for healthy subjects. In most cases, the robot condition is only slightly more negative. Knowing that SAL can typically fall as low as -6 for stroke subjects, it seems reasonable to conclude the the robot did not have a detrimental affect on SAL. As such, the OpenWrist is validated as a measurement device when using this metric.



### 4.3 Subject Study B: The Effect of Robot Dynamics on Wrist Pointing Smoothness

The results of the pilot study and first subject study made it clear that robot dynamics, namely inertia and friction, had a direct impact on the movement smoothness correlation coefficient,  $\rho$ , in wrist pointing tasks. Although movements are generally robust to disturbances, certain perturbations might disrupt an individual's ability to produce these smooth movements. Whether a rehabilitation robot's inherent dynamics impact movement smoothness during pointing tasks has not yet been investigated. To address this, a second subject study was conducted. This subject study involved a similar pointing task as the first, but with robot, not anatomical, joint angles being recorded under four different operating conditions.

#### 4.3.1 Methods

##### Subjects

Seven subjects (2 female, 5 male), ages 21-27 years old participated in the experiment. All subjects were right hand dominant with no current injury or known history of neuromuscular injury in their wrist. Approval for the experiment was obtained through the Rice University Institutional Review Board.

##### Task Description

Subjects performed a wrist pointing task similar to subject study A, with joint angles recorded by the OpenWrist. Wrist pointing movements,  $25^\circ$  in amplitude, were made in the traditional anatomical axes (FE and RU) as well as two diagonal directions (collectively referred to as D), similar to those in the preliminary investigation. How-

ever, these axes were aligned at  $\pm 45^\circ$  from the horizontal axis in task space. Unlike the first subject study, the mapping in this study was uniform in all directions. Subjects performed wrist pointing movements in four different experiment blocks with a new randomized condition in each block. A visual display consisting of a small circular cursor which represented the subject's wrist angle, a large central circular target, and eight large outer circular targets on the perimeter, allowed the user to visualize their position in the 2D coordinate space  $\{\phi_{FE}, \phi_{RU}\}$ . Each block started with the subject's cursor on the center target awaiting the first randomly selected outer target to turn green, indicating the subject should move to that target. Each target remained green for 0.85 seconds before turning red, indicating the movement should be completed. Subjects were instructed to make the wrist pointing movements in a single slashing motion at a speed fast enough to comfortably reach the target before it turned red. The target remained red for 0.85 seconds, at which point the center target would turn green indicating the user to return to the neutral wrist position. This procedure was then repeated for other randomly selected outer targets. The time intervals were chosen so that the subject would move with purpose, but not so fast as to become tired. A total of 128 movements, 16 being to each of the eight targets, were performed per experimental block with (i.e. 32 each for FE and RU axes, and 64 for D axes). Subjects were allowed 30 s of practice with each condition before starting the block. The neutral orientation of the wrist was defined as the robot being in a neutral orientation while the subject grasped the handle.

To assist subjects in staying on the desired axis of movement, specifically for diagonal movements, a virtual tunnel was implemented (see Fig. 4.14). The virtual tunnel repelled movements into it, but did not provide any assistance along the desired axis. The virtual tunnel consisted of virtual walls on either side of the movement axis with

a virtual stiffness of  $30 \frac{\text{Nm}}{\text{rad}}$  and virtual damping of  $0.5 \frac{\text{Nm}\cdot\text{s}}{\text{rad}}$ . FE and RU movements were relatively easy for subjects to make straight movements; however, without the tunnel, making straight multi-DOF off axis movements was very difficult due to friction being felt in both directions simultaneously from the device. Implementing a virtual tunnel allowed subjects to focus on executing movements and not the disturbance forces which made it difficult to make straight and smooth movements to the diagonal targets. The virtual tunnel was desirable for our experiment since we were only interested in the wrist movement's velocity profiles.

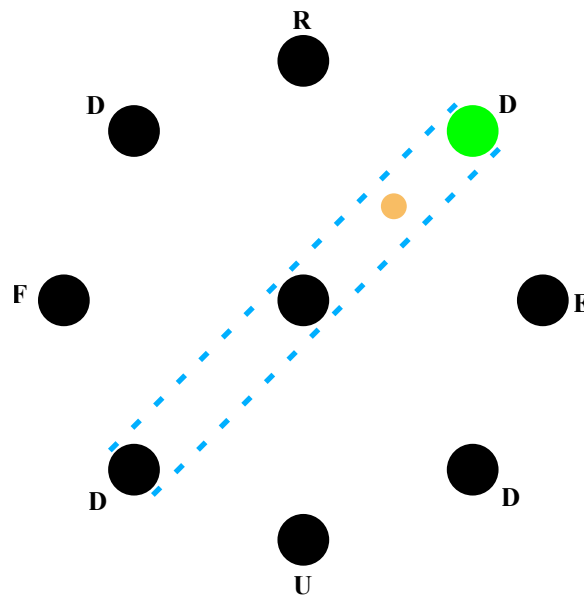


Figure 4.14 : The real-time visual display of the user's cursor (small orange circle) and nine targets shown to subjects during the experiment (note text and dashed lines shown here for reference only). In this trial, the diagonal target requiring an equal combination of radial deviation and extension has turned green, indicating a movement should be made to it. When a target becomes active, a virtual tunnel is implemented (light blue) to aid the user in making movements along the desired axis. The text next to the targets correspond to: extension (E), flexion (F), radial (R) deviation, ulnar (U) deviation, and diagonal (D).

## Conditions

The experiment consisted of four blocks with four conditions (C1, C2, C3, and C4) presented in a pseudo-random fashion to eliminate effects due to order of condition presentation. All conditions contained the virtual tunnel, but C1 and C2 did not contain any additional active interaction torques from the robot. In C1 the device was used as intended with the subject's wrist FE axis aligning with that of the robot's second joint axis and the subject's wrist RU axis aligning with that of the robot's third joint (see Fig. 4.15-a). In C2 subjects pronated their forearm 90° so that their wrist RU axis aligned with the robot's second joint axis, and FE axis aligned with that of the robot's third joint axis (see Fig. 4.15-b). This condition was explored since the robot's third joint contained much more static and Coulomb friction than the second joint (see Table. 3.6), allowing for the examination of the effects of the robot's dynamics on wrist motions for a given wrist movement direction. Note that measurements reported later as RU-C2 refer to the subject's RU movements being measured on and by the robot's FE joint and vice versa for subject FE movements.

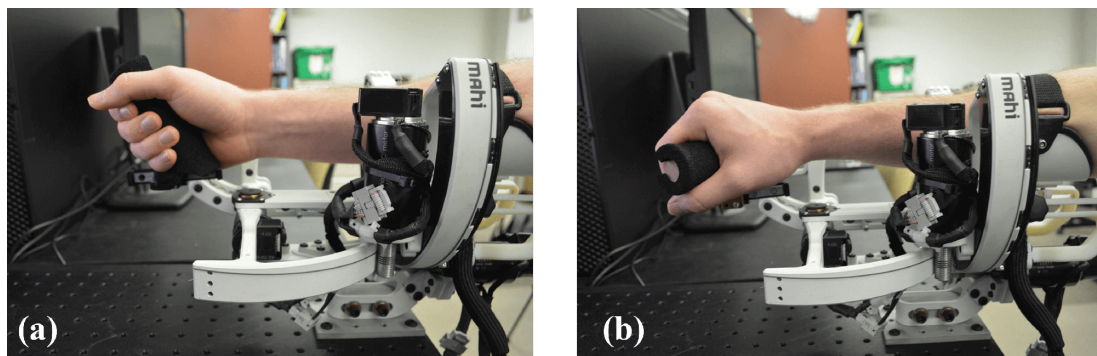


Figure 4.15 : (Left) Subject's neutral posture in conditions 1, 3 and 4 as determined by the intended use of the robot. (Right) Subject's neutral posture in condition 2 where wrist FE is aligned with joint 3, and RU is aligned with joint 2. A rotated grip was used in this condition.

In C3 and C4 subjects resumed normal forearm orientation as in C1, but the device now provided extra assistance or resistance in an effort to reduce (C3) or amplify (C4) perceived Coulomb friction, one of the main sources of interaction torque reflected to the user. It was hypothesized that reducing the effects of Coulomb friction would make movements smoother, especially those performed on the robot’s third joint. Conversely, it was expected that exaggerating Coulomb friction would make movements less smooth. Virtual Coulomb friction was applied separately to each joint using a continuous Coulomb friction model

$$f_{c,a} = f_c \tanh(k\dot{\theta}) \quad (4.7)$$

where  $f_{c,a}$  is the applied Coulomb friction,  $f_c$  the steady state Coulomb friction magnitude,  $k$  defines how quickly the  $\tanh$  function approaches steady state, and  $\dot{\theta}$  is the subject’s velocity on the given joint. In this experiment we used  $k = 0.8$  and  $f_c = 75\%$  of the device’s Coulomb friction values given in Table 3.6. In an effort to remove gravity as a factor, simple gravity compensation was implemented on the device’s RU joint, compensating for 75% of the device’s  $11.5 \text{ N} \cdot \text{mm}$  gravitational torque in the neutral orientation. It should be noted that the device felt significantly more transparent (especially on the device’s RU joint) with the compensatory control action in C3, and felt significantly worse with the added Coulomb friction during C4.

Table 4.1 : Experimental Conditions for Subject Study B.

	Virtual Tunnel	FE Aligned With	RU Aligned With	Friction Modification
C1	Yes	Joint 2	Joint 3	None
C2	Yes	Joint 3	Joint 2	None
C3	Yes	Joint 2	Joint 3	Compensated
C4	Yes	Joint 2	Joint 3	Amplified

## Data Analysis

**Velocity Segmentation** Joint velocities were taken from Quarc software, which estimates them by differentiating and passively filtering encoder positions. Movements were segmented in the same manner as subject study A – at the beginning and end of the movement when velocity crossed the 5% max movement velocity threshold.

**Movement Smoothness** As before in subject study A, the smoothness correlation coefficient  $\rho$  was calculated for each movement using 4.3 and 4.4.

**Statistical Analyses** Statistical comparisons were made using Welch’s *t*-test for all 18 possible comparisons of conditions within a given movement axis (FE, RU, and D). Since eighteen tests were performed, the  $\alpha_c$  levels were adjusted using the false discovery rate correction to account for the family-wise type I error inflation.

### 4.3.2 Results

Velocity data and corresponding movement smoothness, measured through the movement smoothness correlation coefficient  $\rho$ , are presented for all movement directions (FE, RU, and D), and conditions (C1, C2, C3, and C4). The data highlights the differences in movement variability and smoothness for the movement directions and conditions. A plot of the movement velocity profiles for wrist FE and RU movements for all four conditions can be seen in Fig. 4.16. Time and amplitude are normalized for visualization of variability in profiles, while the color of the plots highlights which robot axis the movements were made on. Additionally, the average peak time, time at maximum velocity, of each set of movements is shown on the plots to visualize how movements were skewed depending on condition and movement direction.

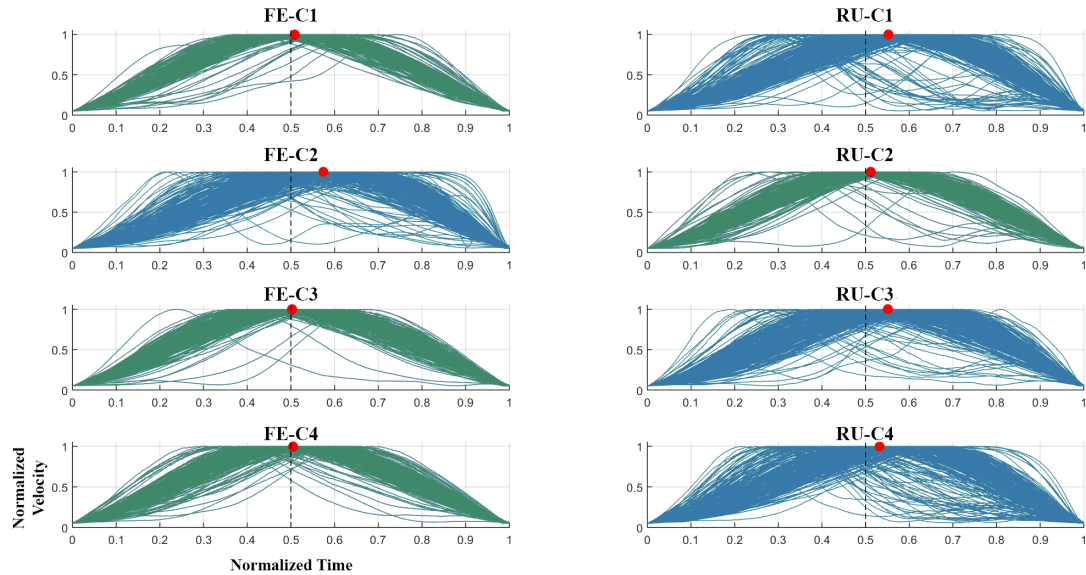


Figure 4.16 : Velocity profiles for FE and RU for all four conditions. For visualization, movements were normalized with respect to time and amplitude. Movements made on the robot’s second joint are in green, while movements made on the robot’s third joint are in blue. The red dots indicate the average peak time for a given movement direction and condition. For reference, a vertically dashed line is shown at  $t=0.5$  which is the peak time for the minimum jerk trajectory.

Representative velocity profiles for C1 and the minimum jerk trajectory (included for reference), can be seen in Fig. 4.17. This plot highlights the shape and skewness of individual velocity profiles. The representative profiles were selected such that  $\rho$  and peak time for the movement approximately matched that of the group mean for that axis and condition.

The group mean  $\rho$  values for each axis and condition are presented in Table 4.2. Comparison of group means for FE and RU movements with respect to robot axis (C1 and C2) can be seen through a barplot in Fig. 4.18(a). A barplot comparing conditions with human and robot axes traditionally aligned with no Coulomb Friction compensation, compensation, and amplification (C1, C3, and C4) for FE and RU can be seen in Fig. 4.18(b). Finally, a barplot comparing all conditions for diagonal

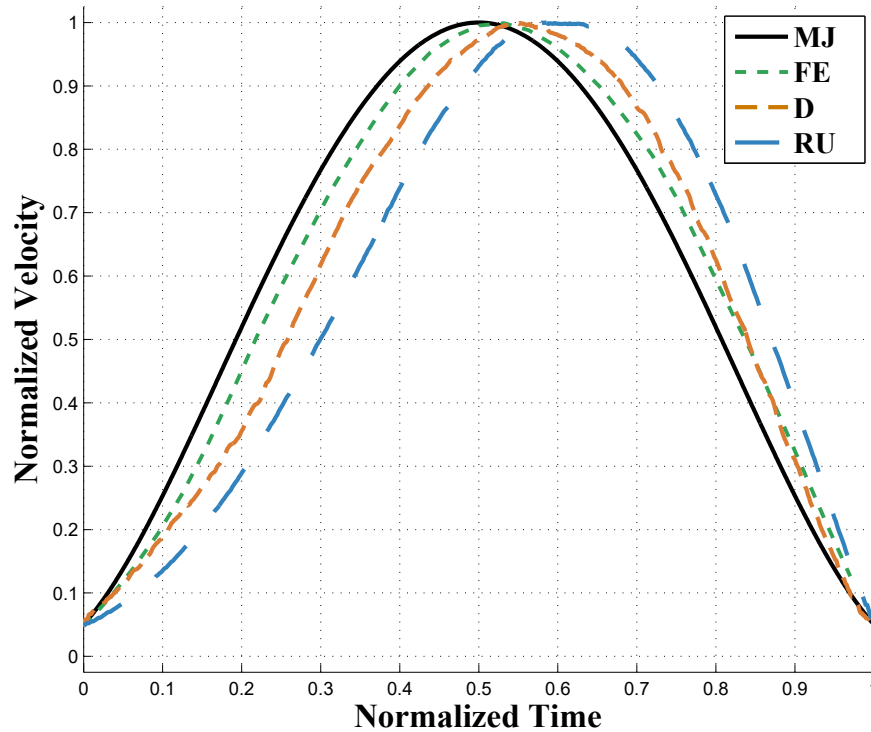


Figure 4.17 : Plot of the minimum jerk trajectory against representative velocity profiles from C1 for FE, RU, and D. Representative velocity profiles were selected with  $\rho$  and peak time values approximately that of the group mean. Time and amplitude were normalized for comparison purposes.

movements is presented in Fig. 4.19. An important note to make is that the values for  $\rho$  presented here should not be compared with those in Fig. 4.10 and Fig. 4.11 due to differences in joint angle measurement (motion capture based vs. encoder based), sampling frequency (100 Hz vs. 1000 Hz), and differentiation and filtering methods.

Eighteen  $t$ -tests were performed examining the effect of condition (C1, C2, C3, and C4) on  $\rho$ , along each axis. False discovery rate was applied to adjust the critical  $\alpha$  value from the 0.05 significance level. Significant differences were found in six of the eighteen comparisons. In comparison between conditions one (C1: human and robot aligned as intended, see Fig. 4.15) and two (C2: human axes rotated compared to



Table 4.2 : Group Mean  $\rho$  Values for Subject Study B.

	C1	C2	C3	C4
FE	0.971	0.865	0.971	0.964
RU	0.848	0.956	0.882	0.865
D	0.96	0.937	0.952	0.944

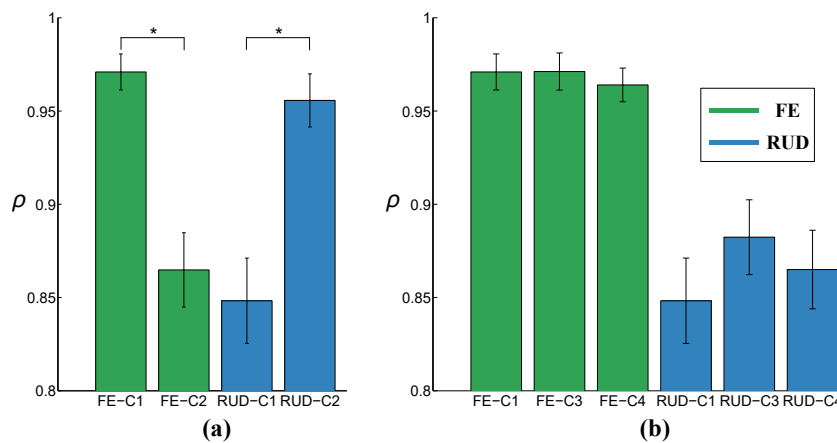


Figure 4.18 : Movement smoothness correlation coefficient  $\rho$  for all FE and RU conditions. Error bars are for a 95% confidence interval (1.96 times the standard error) of all movements for a given condition and movement axis. Statistical significance is indicated by \*. (a) Comparison of C1 and C2. (b) Comparison of C1, C3, and C4.

robot axes as intended, i.e. human RU wrist movements performed and recorded by the robot's FE axis, see Fig. 4.15), a significant ( $t(4.7) = 7.5, p = 0.002, \alpha_c = 0.008$ ) difference was found between FE-C1 and FE-C2, and between RU-C1 and RU-C2 ( $t(4.6) = 9.8, p = 0.001, \alpha_c = 0.006$ ). Comparisons involving conditions three (C3: human and robot axes aligned with Coulomb friction compensation) and four (C4: human and robot axes aligned with virtually added Coulomb friction) had significant differences between FE-C2 and FE-C3 ( $t(4.8) = 7, p = 0.002, \alpha_c = 0.01$ ), FE-C2 and FE-C4 ( $t(4.5) = 6.8, p = 0.003, \alpha_c = 0.014$ ), RU-C2 vs. RU-C3 ( $t(3.4) = 10.5, p = 0.006, \alpha_c = 0.02$ ), and RU-C2 and RU-C4 ( $t(4.5) = 11, p = 0.0009, \alpha_c = 0.003$ ).

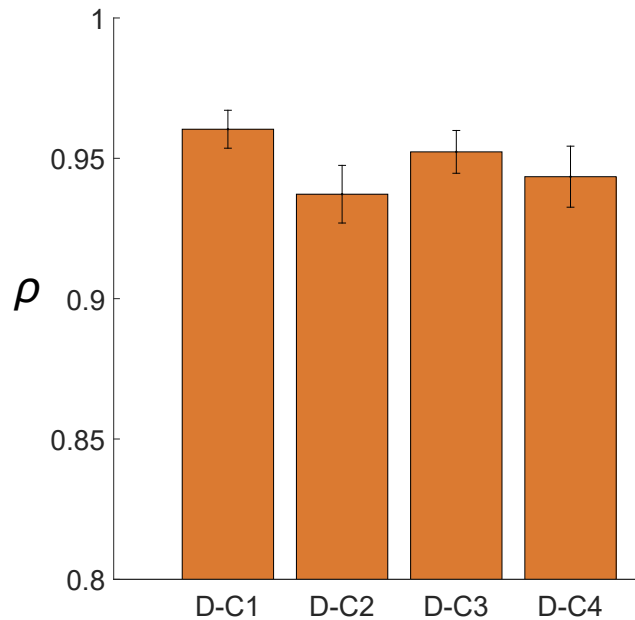


Figure 4.19 : Movement smoothness correlation coefficient  $\rho$  for all diagonal axes and conditions. Error bars are for a 95% confidence interval (1.96 times the standard error) of all movements for a given condition.

None of the other comparisons made were significant, and other than the comparison between D-C1 and D-C2 ( $p = 0.0496, \alpha_c = 0.019$ ), all other comparisons were not significant with  $p > 0.12$ .

### 4.3.3 Discussion

It was found that  $\rho$  is significantly different when the orientation of the hand is changed with respect to the robot joints. In general, movements on the robot's RU axis were less smooth than movements made on the robot's FE axis. The robot's third joint axis had more Coulomb friction than the second joint axis, but also substantially less inertia (see Table 3.6). Without performing C2, one might arrive at the incorrect conclusion that human RU movements made in the robot are less smooth than FE ones. However, by performing C2, the only difference between C1 and C2 is which

robot axis the human wrist axis was on, and thus this conclusion can no longer be made.

Since Coulomb friction in the third joint was much larger than the second joint, we hypothesized that compensating this friction might lead to smoother movements. Although the robot felt much more transparent during C3, and not very transparent during C4, this conclusion was rejected since there was no statistically significant difference between any of the diagonal conditions. Since movements were not different as a result of C3 or C4 for the diagonal movements, which were equally perturbed by the robot's second and third axes, we can conclude that the robot's second axis facilitates smoother movements than those on the robot's third axis.

The discrepancy found in  $\rho$  between FE or RU C1 and C2 is likely a result of non-linear phenomena related to static friction, which is impractical to compensate. Compared to the robot's second joint, the third axis requires a pulley routing mechanism which creates additional friction. However, we can also observe that movements on the robot's second axis are extremely smooth and could be a result of the device's inertia. The device's second axis inertia is significantly larger than that of the human wrist while the device's third axis inertia is comparable. This would agree with the observations of subject study A. As a result, we cannot conclude that movements on either axis are unaffected by the robot, but we can conclude that the robot does impact movement smoothness. Additionally, the fact that C3 or C4 did not impact any movement axis, means that Coulomb friction perturbations are not likely to impact the central nervous system's abilities to generate smooth movements. However, it is likely that the neural control mechanism for smooth trajectory generation could not adapt to static friction due to its erratic nature.

It is important to note that the values for inertia and friction here are representa-

tive of other wrist rehabilitation robots (see Table 3.6), which are generally regarded as highly transparent devices. However, it was found that although interaction torque is much lower than that producible from a healthy subject, even moderate interaction torques could impact an individual's ability to produce smooth movements. In this case, inertia of approximately 10x that of the wrist seemed to aid in generating very smooth movements while static friction, on the order of  $0.1 \text{ N} \cdot \text{mm}$ , resulted in less smooth movements. Where natural movement smoothness lies for wrist trajectories cannot be inferred from this study and is left as future work. Given the seemingly positive impact of inertia on movements, one might argue that actually the friction on the RU joint was not a negative impact, and while this is possible, it is not entirely likely since we found in the pilot study with the RW-S, which had larger friction in the RU joint, resulted in even less smooth movements being made on that joint.

Future work should explore inertial compensation of the joint to see if that has an impact on movement smoothness. Several studies have designed compensators for inertia [68, 69], although these are usually difficult to implement and can become non-passive. In general it seems feasible to compensate for up to 50% of a device's inertia. Additionally, designers might take these results into account and attempt to make lower inertia and lower friction joints than before. Another approach to this issue could be to use direct force control as in [68], but it is also unknown how force control would impact pointing movements.

Robotic devices have been used for several decades to study neural control during pointing movements. However, it does not appear that attention has been paid to how the robot impacts these movements. Robots certainly provide an excellent opportunity to study movements, especially when considering the high resolution and repeatability that can be obtained using them when compared with less obtrusive

means such as motion capture or inertial measurement units. However, we need to carefully consider the role robots might play in influencing natural movements, even when the device feels relatively transparent.

## Chapter 5

### Conclusions

Robot-augmented therapy is a clinically verified path forward to improving rehabilitation outcomes for several neuromuscular conditions such as CVA and SCI. To date, many devices for upper-extremity rehabilitation have been developed for both the wrist and hand, separately. However, few, if any, devices have been developed for coordinated hand-wrist therapy. This oversight fails to recognize the kinematic and dynamic linkings of the hand and wrist that arise from their interconnect musculature, as well as their position-dependent passive properties. To this end, a new coordinated hand-wrist exoskeleton, the READAPT, has been proposed, and the wrist module, the OpenWrist, has been developed.

The OpenWrist, leveraging over a decade of experience in upper-extremity exoskeleton development, has been designed to address all of the requirements previously outlined for coordinated hand-wrist exoskeletons. Torque output and ROM exceed requirements for ADL, and match or exceed reported values of most other existing devices, as shown in Table 2.4. Compared with its predecessor, the RiceWrist-S, a number of functional improvements have been introduced. The PS joint has been changed from an enclosed design to an open design, eliminating the need for users to insert their arm into the device, while an adjustable foam padded elbow support addresses ergonomic downfalls of previous devices. In a standalone wrist-only mode, the OpenWrist introduces a new angled grip that increases practical workspace by 51%. Small, but important additions such as integrated tensioning mechanisms and

a motion capture compatible coating further enhance its effectiveness in clinical and research settings

Characterization of the OpenWrist underscores the significance of the numerous design changes made. Compared with the RiceWrist-S, inertia reductions of 12% and 21% are achieved in the FE and RU joints, respectively, as a result of lower weight components and strategically placed actuators. Hybrid-ceramic ball bearings and improved capstan-cable windings contribute to decreases in maximum static friction by 47% in FE and 27% in RU. Kinetic friction values measured for the OpenWrist consume a maximum of only 6% of the continuous torque output in any joint. Closed-loop position bandwidth is increased over the RiceWrist-S across the board and either exceeds or is slightly less than the 5 Hz achievable by humans in uncontrolled motions.

Multiple subject studies involving healthy individuals indicate that spectral arc length, a commonly used movement smoothness metric for assessing motor skill recovery, is largely unaffected by the OpenWrist. As such, the OpenWrist is validated as an accurate assessment device for stroke and SCI. Furthermore, this thesis has shown that the movement smoothness correlation coefficient,  $\rho$ , is affected by robot dynamics, namely inertia and friction, and is likely not an accurate smoothness metric for assessment with rehabilitative robots.

Future work will involve the integration of the OpenWrist and the ReNue Maestro hand-exoskeleton, both mechanically and through software, in an effort to realize a fully operational iteration of the READAPT project. The coupling will result in one of, if not the first coordinated hand-wrist exoskeletal devices, opening several exciting avenues for future research. Additionally, the OpenWrist platform will continue to evolve, as the next version, the OpenWrist-Lite, is already under development.

## Appendix A

### OpenWrist Kinematic and Dynamic Equations

This appendix chapter provides the MATLAB code needed to generate the forward kinematics and dynamic equations of motion symbolically for the OpenWrist (see Sections 2.2 and 2.3 for more detail). The code makes use of a few generic robotics functions I previously wrote for class projects, and as such could be used for other robotic manipulators if desired.

The main script for generating the forward kinematics and equations of motions is provided first, followed by the required functions `DH2TF`, `NewtonEuler`, and `SeparateMVG`. The symbolic output of the matrix  $M$  and the vectors  $V$  and  $G$  is provided last in a format that can copied and pasted into most programming languages (you're welcome, future MAHI grad student).



```

% Evan Pezent | evanpezent.com | epezent@rice.edu
% 02/04/2017

% =====
% This script computes the OpenWrist dynamic equations symbolically using
% the Newton-Euler approach, and rearranges all terms in the form:
% Tau = M(Q)Q'' + V(Q,Q') + G(Q) + B.*Q' + Fk.*sign(Q')
% =====

%% Define Symbolic Symbols
syms tau1 q1 q1d q1dd m1 b1 fk1 ...
      tau2 q2 q2d q2dd m2 b2 fk2 ...
      tau3 q3 q3d q3dd m3 b3 fk3 ...
      Pc1x Pc1y Pc1z   Ic1xx Ic1xy Ic1xz Ic1yy Ic1yz Ic1zz ...
      Pc2x Pc2y Pc2z   Ic2xx Ic2xy Ic2xz Ic2yy Ic2yz Ic2zz ...
      Pc3x Pc3y Pc3z   Ic3xx Ic3xy Ic3xz Ic3yy Ic3yz Ic3zz ...
      g

Tau = [tau1; tau2; tau3];

Q = [q1;q2;q3];
Qd = [q1d;q2d;q3d];
Qdd = [q1dd;q2dd;q3dd];

B = [b1;b2;b3];
Fk = [fk1;fk2;fk3];

Pc1 = [Pc1x Pc1y Pc1z].';
Pc2 = [Pc2x Pc2y Pc2z].';
Pc3 = [Pc3x Pc3y Pc3z].';

Ic1 = [Ic1xx -Ic1xy -Ic1xz;
       -Ic1xy Ic1yy -Ic1yz;
       -Ic1xz -Ic1yz Ic1xx];

Ic2 = [Ic2xx -Ic2xy -Ic2xz;
       -Ic2xy Ic2yy -Ic2yz;
       -Ic2xz -Ic2yz Ic2xx];

Ic3 = [Ic3xx -Ic3xy -Ic3xz;
       -Ic3xy Ic3yy -Ic3yz;
       -Ic3xz -Ic3yz Ic3xx];

%% Forward Kinematics
DH_table = [0 0 0 q1;
            0 pi/2 0 q2-pi/2;
            0 pi/2 0 q3];

[~,T_array] = DH2TF(DH_table);

%% Newton-Euler Dynamics
m = [m1;m2;m3];
Pc = {Pc1 Pc2 Pc3};
Ic = {Ic1 Ic2 Ic3};
g0 = [0; g; 0];
MVG = NewtonEuler(m,Pc,Ic,T_array,Qd,Qdd,g0);
MVG = simplify(expand(MVG));

%% Separate MVG into M, V, and G
[M,V,G] = SeparateMVG(MVG,Qdd,g);

%% Get Equation of Motion
EOM = Tau == M*Qdd + V + G + B.*Qd + Fk.*sign(Qd);

```

```

% Evan Pezent | evanpezent.com | epezent@rice.edu
% 02/11/2016

function [T_end,T_array] = DH2TF(DH_table)
% =====
% Accepts an Nx4 matrix with rows of the form [a alpha d theta] which
% correspond to the DH parameters of subsequent frames. The first row
% should be frame 1, the second row frame 2, and so on so forth until the
% final frame i. Returns the transformation from frame N to 0, and an
% N-array of transformations each describing frame i relative to frame i-1,
% i.e. mapping i to i-1.
% =====
% Source: Introduction to Robotics: Mechanics and Control (3e) - Craig, J.
% Eqns: 3.6 (pg. 75)
% =====

T_array = cell(1,size(DH_table,1));
T_end = eye(4);

for ii = 1:size(DH_table,1)
    a = DH_table(ii,1);
    alpha = DH_table(ii,2);
    d = DH_table(ii,3);
    theta = DH_table(ii,4);
    sinTheta = sin(theta);
    cosTheta = cos(theta);
    sinAlpha = sin(alpha);
    cosAlpha = cos(alpha);
    T = [cosTheta -sinTheta 0 a;
         sinTheta*cosAlpha cosTheta*cosAlpha -sinAlpha -sinAlpha*d;
         sinTheta*sinAlpha cosTheta*sinAlpha cosAlpha cosAlpha*d;
         0 0 0 1];
    T_array{ii} = T;
    T_end = T_end*T;
end

end

```

```

% Evan Pezent | evanpezent.com | epezent@rice.edu
% 02/04/2017

function [Tau,w,wd,vd,vcd,F,N,f,n] = NewtonEuler(m,Pc,Ic,T_array,Qd,Qdd,g0)
% =====
% Computes the dynamic equations of motion for a rotational robotic
% manipulator using the iterative Newton-Euler formulation.
%
% m = [n x 1] vector of link masses
% Pc = n length cell array of [3 x 1] translations from {i} to {c_i}
% Ic = n length cell array of [3 x 3] inertia tensors take about {c_i}
% T_array = T_array as obtained from function DH2TF(DH_table)
% Qd = [n x 1] vector of joint angular velocities
% Qdd = [n x 1] vector of joint angular accelerations
% g0 = [3 x 1] gravity vector in {0}.
%
% where
%
% {i} is the frame attached to link i
% {c_i} is the frame at the COM of link i with the same orientation as {i}
% =====
% Source: Introduction to Robotics: Mechanics and Control (3e) - Craig, J.
% Eqns: 6.45 - 6.53 (pg. 176)
% =====

num = length(m);

% Pad vectors for notation consistency
m = [0; m];
Pc = [0 Pc];
Ic = [0 Ic];
Qd = [0; Qd];
Qdd = [0; Qdd];

% Local X vector
Z = [0; 0; 1];

% Frame 0 Variables
w{1} = [0 0 0].';
wd{1} = [0 0 0].';

% Gravity Orientation
% "The effect of gravity loading on the links can be included quite simply
% by setting vd0 = G, where G has the magnitude of the gravity vector but
% points in the opposite direction. This is equivalent to saying that the
% base of the robot is accelerating upward with 1 g acceleration. This
% fictitious upward acceleration causes exactly the same effect on the
% links as gravity would." - pg. 176
G = -g0;
vd{1} = G;

%% Outward Iterations
for i = 1:num % 0 -> n-1
    R      = T_array{i}(1:3,1:3).'; % ^{i+1}_i R
    P      = T_array{i}(1:3,4); % ^i P_{i+1}
    w{i+1} = R*w{i} + Qd(i+1)*Z; % 6.45
    wd{i+1} = R*wd{i} + cross(R*w{i},Qd(i+1)*Z) + Qdd(i+1)*Z; % 6.46
    vd{i+1} = R*(cross(wd{i},P) + cross(w{i},cross(w{i},P)) + vd{i}); % 6.47
    vcd{i+1} = cross(wd{i+1},Pc{i+1}) + cross(w{i+1},cross(w{i+1},Pc{i+1})) +
vd{i+1}; % 6.48
    F{i+1} = m(i+1)*vcd{i+1}; % 6.49
    N{i+1} = Ic{i+1}*wd{i+1} + cross(w{i+1},Ic{i+1}*w{i+1}); % 6.50
end

```

```

%% Inward Iterations
for i = num+1:-1:2 % n -> 1
    if i == num+1
        f{i} = F{i}; % 6.51
        n{i} = N{i} + cross(Pc{i},F{i}); % 6.52
    else
        R = T_array{i}(1:3,1:3);
        P = T_array{i}(1:3,4);
        f{i} = R*f{i+1} + F{i}; % 6.51
        n{i} = N{i} + R*n{i+1} + cross(Pc{i},F{i}) + cross(P,R*f{i+1}); % 6.52
    end
    Tau(i,1) = n{i}.*Z; % 6.53
end

%% Clean up elements related to 0th frame
Tau(1) = [];
w(:,1) = [];
wd(:,1) = [];
vd(:,1) = [];
vcd(:,1) = [];
F(:,1) = [];
N(:,1) = [];
f(:,1) = [];
n(:,1) = [];

end

```

```

% Evan Pezent | evanpezent.com | epezent@rice.edu
% 02/11/2016

function [M,V,G] = SeparateMVG(MVG,Qdd,g)
% =====
% Extracts the mass matrix M, the vector of centrifugal and Coriolis terms
% V, and the vector of gravity terms G from the clumped symbolic expression
% MVG. Qdd is the [n x 1] vector of joint accelerations and g is gravity.
% =====

n = length(MVG);

% Extract M
for i = 1:n
    mvg = MVG(i);
    for j = 1:n
        m_temp = char(collect(mvg,Qdd(j)));
        ind = strfind(m_temp,char(Qdd(j)));
        if length(ind) < 2
            m = m_temp(1:ind-2);
            M(i,j) = simplify(expand(evalin('base',m)));
        else
            error(['Could not collect ' char(Qdd(j)) '.'])
        end
    end
end

% Reduce MVG to VG
VG = simplify(expand(MVG - M*Qdd));
for i = 1:n
    vg = VG(i);
    g_temp = char(collect(vg,g));
    ind = strfind(g_temp,char(g));
    if length(ind) < 2
        g_i = g_temp(1:ind-2);
    else
        error(['Could not collect ' char(g) '.'])
    end
    G(i,1) = simplify(expand(evalin('base',g_i))*g);
end

% Reduce VG to V
V = simplify(expand(VG-G));

end

```

**M(1,1) =**

$$\begin{aligned} &Ic1xx + Ic3xx + Ic2yy + Pc1x^2*m1 + Pc1y^2*m1 + Pc2x^2*m2 + Pc3x^2*m3 + Pc2z^2*m2 + \\ &Pc3y^2*m3 + Ic2xx*cos(q2)^2 - Ic3xx*cos(q2)^2 - Ic2yy*cos(q2)^2 + Ic3yy*cos(q2)^2 + \\ &Ic2xy*sin(2*q2) + Ic3xx*cos(q2)^2*cos(q3)^2 - Ic3yy*cos(q2)^2*cos(q3)^2 - \\ &Pc2x^2*m2*cos(q2)^2 + Pc2y^2*m2*cos(q2)^2 - Pc3y^2*m3*cos(q2)^2 + \\ &Pc3z^2*m3*cos(q2)^2 - 2*Ic3xz*cos(q2)*cos(q3)*sin(q2) + \\ &2*Ic3yz*cos(q2)*sin(q2)*sin(q3) + 2*Ic3xy*cos(q2)^2*cos(q3)*sin(q3) + \\ &Pc2x*Pc2y*m2*sin(2*q2) - Pc3x^2*m3*cos(q2)^2*cos(q3)^2 + \\ &Pc3y^2*m3*cos(q2)^2*cos(q3)^2 + 2*Pc3y*Pc3z*m3*cos(q2)*sin(q2)*sin(q3) + \\ &2*Pc3x*Pc3y*m3*cos(q2)^2*cos(q3)*sin(q3) - 2*Pc3x*Pc3z*m3*cos(q2)*cos(q3)*sin(q2) \end{aligned}$$

**M(1,2) =**

$$\begin{aligned} &Ic2xz*cos(q2) - Ic3xy*cos(q2) - Ic2yz*sin(q2) + Ic3yz*cos(q3)*sin(q2) + \\ &Ic3xz*sin(q2)*sin(q3) + 2*Ic3xy*cos(q2)*cos(q3)^2 - Ic3xx*cos(q2)*cos(q3)*sin(q3) + \\ &Ic3yy*cos(q2)*cos(q3)*sin(q3) + Pc2x*Pc2z*m2*cos(q2) - Pc3x*Pc3y*m3*cos(q2) - \\ &Pc2y*Pc2z*m2*sin(q2) + Pc3x^2*m3*cos(q2)*cos(q3)*sin(q3) - \\ &Pc3y^2*m3*cos(q2)*cos(q3)*sin(q3) + Pc3y*Pc3z*m3*cos(q3)*sin(q2) + \\ &Pc3x*Pc3z*m3*sin(q2)*sin(q3) + 2*Pc3x*Pc3y*m3*cos(q2)*cos(q3)^2 \end{aligned}$$

**M(1,3) =**

$$\begin{aligned} &- m3*sin(q2)*Pc3x^2 + Pc3z*m3*cos(q2)*cos(q3)*Pc3x - m3*sin(q2)*Pc3y^2 - \\ &Pc3z*m3*cos(q2)*sin(q3)*Pc3y - Ic3xx*sin(q2) + Ic3xz*cos(q2)*cos(q3) - \\ &Ic3yz*cos(q2)*sin(q3) \end{aligned}$$

**M(2,1) =**

$$\begin{aligned} &Ic2xz*cos(q2) - Ic3xy*cos(q2) - Ic2yz*sin(q2) + Ic3yz*cos(q3)*sin(q2) + \\ &Ic3xz*sin(q2)*sin(q3) + 2*Ic3xy*cos(q2)*cos(q3)^2 - Ic3xx*cos(q2)*cos(q3)*sin(q3) + \\ &Ic3yy*cos(q2)*cos(q3)*sin(q3) + Pc2x*Pc2z*m2*cos(q2) - Pc3x*Pc3y*m3*cos(q2) - \\ &Pc2y*Pc2z*m2*sin(q2) + Pc3x^2*m3*cos(q2)*cos(q3)*sin(q3) - \\ &Pc3y^2*m3*cos(q2)*cos(q3)*sin(q3) + Pc3y*Pc3z*m3*cos(q3)*sin(q2) + \\ &Pc3x*Pc3z*m3*sin(q2)*sin(q3) + 2*Pc3x*Pc3y*m3*cos(q2)*cos(q3)^2 \end{aligned}$$

**M(2,2) =**

$$\begin{aligned} &Ic2xx + Ic3xx + Pc2x^2*m2 + Pc2y^2*m2 + Pc3y^2*m3 + Pc3z^2*m3 - Ic3xx*cos(q3)^2 + \\ &Ic3yy*cos(q3)^2 - Ic3xy*sin(2*q3) + Pc3x^2*m3*cos(q3)^2 - Pc3y^2*m3*cos(q3)^2 - \\ &Pc3x*Pc3y*m3*sin(2*q3) \end{aligned}$$

**M(2,3) =**

$$- Ic3yz*cos(q3) - Ic3xz*sin(q3) - Pc3y*Pc3z*m3*cos(q3) - Pc3x*Pc3z*m3*sin(q3)$$

**M(3,1) =**

$$\begin{aligned} &- m3*sin(q2)*Pc3x^2 + Pc3z*m3*cos(q2)*cos(q3)*Pc3x - m3*sin(q2)*Pc3y^2 - \\ &Pc3z*m3*cos(q2)*sin(q3)*Pc3y - Ic3xx*sin(q2) + Ic3xz*cos(q2)*cos(q3) - \\ &Ic3yz*cos(q2)*sin(q3) \end{aligned}$$

**M(3,2) =**

$$- Ic3yz*cos(q3) - Ic3xz*sin(q3) - Pc3y*Pc3z*m3*cos(q3) - Pc3x*Pc3z*m3*sin(q3)$$

**M(3,3) =**

$$m3*Pc3x^2 + m3*Pc3y^2 + Ic3xx$$

$\mathbf{v}(1,1) =$

$$\begin{aligned}
& \text{Ic3xy} * \text{q2d}^2 * \sin(\text{q2}) - \text{Ic2xz} * \text{q2d}^2 * \sin(\text{q2}) - \text{Ic2yz} * \text{q2d}^2 * \cos(\text{q2}) - 2 * \text{Ic2xy} * \text{q1d} * \text{q2d} + \\
& \text{Ic3yz} * \text{q2d}^2 * \cos(\text{q2}) * \cos(\text{q3}) - \text{Ic3yz} * \text{q3d}^2 * \cos(\text{q2}) * \cos(\text{q3}) + \\
& \text{Ic3xz} * \text{q2d}^2 * \cos(\text{q2}) * \sin(\text{q3}) - \text{Ic3xz} * \text{q3d}^2 * \cos(\text{q2}) * \sin(\text{q3}) + 2 * \text{Ic3xz} * \text{q1d} * \text{q2d} * \cos(\text{q3}) \\
& - \text{Ic3yy} * \text{q2d} * \text{q3d} * \cos(\text{q2}) - 2 * \text{Ic3yz} * \text{q1d} * \text{q2d} * \sin(\text{q3}) - 2 * \text{Ic3xy} * \text{q2d}^2 * \cos(\text{q3})^2 * \sin(\text{q2}) \\
& + 4 * \text{Ic2xy} * \text{q1d} * \text{q2d} * \cos(\text{q2})^2 - 2 * \text{Ic3xy} * \text{q1d} * \text{q3d} * \cos(\text{q2})^2 - \text{Ic2xx} * \text{q1d} * \text{q2d} * \sin(2 * \text{q2}) + \\
& \text{Ic3xx} * \text{q1d} * \text{q2d} * \sin(2 * \text{q2}) + \text{Ic2yy} * \text{q1d} * \text{q2d} * \sin(2 * \text{q2}) - \text{Ic3yy} * \text{q1d} * \text{q2d} * \sin(2 * \text{q2}) - \\
& \text{Pc2y} * \text{Pc2z} * \text{m2} * \text{q2d}^2 * \cos(\text{q2}) + \text{Ic3xx} * \text{q2d}^2 * \cos(\text{q3}) * \sin(\text{q2}) * \sin(\text{q3}) - \\
& \text{Ic3yy} * \text{q2d}^2 * \cos(\text{q3}) * \sin(\text{q2}) * \sin(\text{q3}) - \text{Pc2x} * \text{Pc2z} * \text{m2} * \text{q2d}^2 * \sin(\text{q2}) + \\
& \text{Pc3x} * \text{Pc3y} * \text{m3} * \text{q2d}^2 * \sin(\text{q2}) - 2 * \text{Pc3x}^2 * \text{m3} * \text{q2d} * \text{q3d} * \cos(\text{q2}) - 2 * \text{Pc2x} * \text{Pc2y} * \text{m2} * \text{q1d} * \text{q2d} - \\
& 2 * \text{Ic3xx} * \text{q2d} * \text{q3d} * \cos(\text{q2}) * \cos(\text{q3})^2 - 4 * \text{Ic3xz} * \text{q1d} * \text{q2d} * \cos(\text{q2})^2 * \cos(\text{q3}) + \\
& 2 * \text{Ic3yy} * \text{q2d} * \text{q3d} * \cos(\text{q2}) * \cos(\text{q3})^2 + \text{Pc2x}^2 * \text{m2} * \text{q1d} * \text{q2d} * \sin(2 * \text{q2}) - \\
& \text{Pc2y}^2 * \text{m2} * \text{q1d} * \text{q2d} * \sin(2 * \text{q2}) + \text{Pc3y}^2 * \text{m3} * \text{q1d} * \text{q2d} * \sin(2 * \text{q2}) - \\
& \text{Pc3z}^2 * \text{m3} * \text{q1d} * \text{q2d} * \sin(2 * \text{q2}) + 4 * \text{Ic3yz} * \text{q1d} * \text{q2d} * \cos(\text{q2})^2 * \sin(\text{q3}) + \\
& 4 * \text{Ic3xy} * \text{q1d} * \text{q3d} * \cos(\text{q2})^2 * \cos(\text{q3})^2 - 4 * \text{Ic3xy} * \text{q2d} * \text{q3d} * \cos(\text{q2}) * \cos(\text{q3}) * \sin(\text{q3}) + \\
& 2 * \text{Ic3yz} * \text{q1d} * \text{q3d} * \cos(\text{q2}) * \cos(\text{q3}) * \sin(\text{q2}) + 2 * \text{Pc3x} * \text{Pc3z} * \text{m3} * \text{q1d} * \text{q2d} * \cos(\text{q3}) + \\
& 2 * \text{Ic3xz} * \text{q1d} * \text{q3d} * \cos(\text{q2}) * \sin(\text{q2}) * \sin(\text{q3}) - 2 * \text{Pc3y} * \text{Pc3z} * \text{m3} * \text{q1d} * \text{q2d} * \sin(\text{q3}) - \\
& 2 * \text{Pc3x} * \text{Pc3y} * \text{m3} * \text{q2d}^2 * \cos(\text{q3})^2 * \sin(\text{q2}) + 2 * \text{Pc3x}^2 * \text{m3} * \text{q2d} * \text{q3d} * \cos(\text{q2}) * \cos(\text{q3})^2 - \\
& 2 * \text{Pc3y}^2 * \text{m3} * \text{q2d} * \text{q3d} * \cos(\text{q2}) * \cos(\text{q3})^2 - 2 * \text{Ic3xx} * \text{q1d} * \text{q2d} * \cos(\text{q2}) * \cos(\text{q3})^2 * \sin(\text{q2}) - \\
& 2 * \text{Ic3xx} * \text{q1d} * \text{q3d} * \cos(\text{q2})^2 * \cos(\text{q3}) * \sin(\text{q3}) + \\
& 2 * \text{Ic3yy} * \text{q1d} * \text{q2d} * \cos(\text{q2}) * \cos(\text{q3})^2 * \sin(\text{q2}) + \\
& 2 * \text{Ic3yy} * \text{q1d} * \text{q3d} * \cos(\text{q2})^2 * \cos(\text{q3}) * \sin(\text{q3}) + 4 * \text{Pc2x} * \text{Pc2y} * \text{m2} * \text{q1d} * \text{q2d} * \cos(\text{q2})^2 - \\
& 2 * \text{Pc3x} * \text{Pc3y} * \text{m3} * \text{q1d} * \text{q3d} * \cos(\text{q2})^2 + \text{Pc3y} * \text{Pc3z} * \text{m3} * \text{q2d}^2 * \cos(\text{q2}) * \cos(\text{q3}) - \\
& \text{Pc3y} * \text{Pc3z} * \text{m3} * \text{q3d}^2 * \cos(\text{q2}) * \cos(\text{q3}) - \text{Pc3x}^2 * \text{m3} * \text{q2d}^2 * \cos(\text{q3}) * \sin(\text{q2}) * \sin(\text{q3}) + \\
& \text{Pc3y}^2 * \text{m3} * \text{q2d}^2 * \cos(\text{q3}) * \sin(\text{q2}) * \sin(\text{q3}) + \text{Pc3x} * \text{Pc3z} * \text{m3} * \text{q2d}^2 * \cos(\text{q2}) * \sin(\text{q3}) - \\
& \text{Pc3x} * \text{Pc3z} * \text{m3} * \text{q3d}^2 * \cos(\text{q2}) * \sin(\text{q3}) + 2 * \text{Pc3x}^2 * \text{m3} * \text{q1d} * \text{q2d} * \cos(\text{q2}) * \cos(\text{q3})^2 * \sin(\text{q2}) - \\
& 2 * \text{Pc3y}^2 * \text{m3} * \text{q1d} * \text{q2d} * \cos(\text{q2}) * \cos(\text{q3})^2 * \sin(\text{q2}) + \\
& 2 * \text{Pc3x}^2 * \text{m3} * \text{q1d} * \text{q3d} * \cos(\text{q2})^2 * \cos(\text{q3}) * \sin(\text{q3}) - \\
& 2 * \text{Pc3y}^2 * \text{m3} * \text{q1d} * \text{q3d} * \cos(\text{q2})^2 * \cos(\text{q3}) * \sin(\text{q3}) - \\
& 4 * \text{Pc3x} * \text{Pc3z} * \text{m3} * \text{q1d} * \text{q2d} * \cos(\text{q2})^2 * \cos(\text{q3}) + 4 * \text{Pc3y} * \text{Pc3z} * \text{m3} * \text{q1d} * \text{q2d} * \cos(\text{q2})^2 * \sin(\text{q3}) \\
& + 4 * \text{Pc3x} * \text{Pc3y} * \text{m3} * \text{q1d} * \text{q3d} * \cos(\text{q2})^2 * \cos(\text{q3})^2 - \\
& 4 * \text{Ic3xy} * \text{q1d} * \text{q2d} * \cos(\text{q2}) * \cos(\text{q3}) * \sin(\text{q2}) * \sin(\text{q3}) - \\
& 4 * \text{Pc3x} * \text{Pc3y} * \text{m3} * \text{q2d} * \text{q3d} * \cos(\text{q2}) * \cos(\text{q3}) * \sin(\text{q3}) + \\
& 2 * \text{Pc3y} * \text{Pc3z} * \text{m3} * \text{q1d} * \text{q3d} * \cos(\text{q2}) * \cos(\text{q3}) * \sin(\text{q2}) + \\
& 2 * \text{Pc3x} * \text{Pc3z} * \text{m3} * \text{q1d} * \text{q3d} * \cos(\text{q2}) * \sin(\text{q2}) * \sin(\text{q3}) - \\
& 4 * \text{Pc3x} * \text{Pc3y} * \text{m3} * \text{q1d} * \text{q2d} * \cos(\text{q2}) * \cos(\text{q3}) * \sin(\text{q2}) * \sin(\text{q3})
\end{aligned}$$

**v(2,1) =**

$$\begin{aligned}
& Ic2xy*q1d^2 - Ic3xz*q1d^2*cos(q3) - Ic3xz*q3d^2*cos(q3) + Ic3yz*q1d^2*sin(q3) + \\
& Ic3yz*q3d^2*sin(q3) + 2*Ic3xy*q2d*q3d - 2*Ic2xy*q1d^2*cos(q2)^2 + \\
& (Ic2xx*q1d^2*sin(2*q2))/2 - (Ic3xx*q1d^2*sin(2*q2))/2 - (Ic2yy*q1d^2*sin(2*q2))/2 + \\
& (Ic3yy*q1d^2*sin(2*q2))/2 + Pc2x*Pc2y*m2*q1d^2 + 2*Ic3xx*q1d*q3d*cos(q2) - \\
& Ic3yy*q1d*q3d*cos(q2) + 2*Ic3xz*q1d^2*cos(q2)^2*cos(q3) - \\
& (Pc2x^2*m2*q1d^2*sin(2*q2))/2 + (Pc2y^2*m2*q1d^2*sin(2*q2))/2 - \\
& (Pc3y^2*m3*q1d^2*sin(2*q2))/2 + (Pc3z^2*m3*q1d^2*sin(2*q2))/2 - \\
& 2*Ic3yz*q1d^2*cos(q2)^2*sin(q3) - 4*Ic3xy*q2d*q3d*cos(q3)^2 + \\
& Ic3xx*q2d*q3d*sin(2*q3) - Ic3yy*q2d*q3d*sin(2*q3) - Pc3x*Pc3z*m3*q1d^2*cos(q3) - \\
& Pc3x*Pc3z*m3*q3d^2*cos(q3) + Pc3y*Pc3z*m3*q1d^2*sin(q3) + Pc3y*Pc3z*m3*q3d^2*sin(q3) \\
& + 2*Pc3y^2*m3*q1d*q3d*cos(q2) + 2*Ic3xz*q1d*q3d*cos(q3)*sin(q2) + \\
& 2*Pc3x*Pc3y*m3*q2d*q3d - 2*Ic3yz*q1d*q3d*sin(q2)*sin(q3) + \\
& Ic3xx*q1d^2*cos(q2)*cos(q3)^2*sin(q2) - Ic3yy*q1d^2*cos(q2)*cos(q3)^2*sin(q2) - \\
& 2*Pc2x*Pc2y*m2*q1d^2*cos(q2)^2 - 2*Ic3xx*q1d*q3d*cos(q2)*cos(q3)^2 + \\
& 2*Ic3yy*q1d*q3d*cos(q2)*cos(q3)^2 - Pc3x^2*m3*q2d*q3d*sin(2*q3) + \\
& Pc3y^2*m3*q2d*q3d*sin(2*q3) - 4*Ic3xy*q1d*q3d*cos(q2)*cos(q3)*sin(q3) - \\
& Pc3x^2*m3*q1d^2*cos(q2)*cos(q3)^2*sin(q2) + \\
& Pc3y^2*m3*q1d^2*cos(q2)*cos(q3)^2*sin(q2) + 2*Pc3x*Pc3z*m3*q1d^2*cos(q2)^2*cos(q3) - \\
& 2*Pc3y*Pc3z*m3*q1d^2*cos(q2)^2*sin(q3) + 2*Pc3x^2*m3*q1d*q3d*cos(q2)*cos(q3)^2 - \\
& 2*Pc3y^2*m3*q1d*q3d*cos(q2)*cos(q3)^2 - 4*Pc3x*Pc3y*m3*q2d*q3d*cos(q3)^2 + \\
& 2*Ic3xy*q1d^2*cos(q2)*cos(q3)*sin(q2)*sin(q3) + \\
& 2*Pc3x*Pc3z*m3*q1d*q3d*cos(q3)*sin(q2) - 2*Pc3y*Pc3z*m3*q1d*q3d*sin(q2)*sin(q3) + \\
& 2*Pc3x*Pc3y*m3*q1d^2*cos(q2)*cos(q3)*sin(q2)*sin(q3) - \\
& 4*Pc3x*Pc3y*m3*q1d*q3d*cos(q2)*cos(q3)*sin(q3)
\end{aligned}$$

**v(3,1) =**

$$\begin{aligned}
& Ic3xy*q1d^2*cos(q2)^2 - Ic3xy*q2d^2 + 2*Ic3xy*q2d^2*cos(q3)^2 - \\
& (Ic3xx*q2d^2*sin(2*q3))/2 + (Ic3yy*q2d^2*sin(2*q3))/2 - Pc3x*Pc3y*m3*q2d^2 - \\
& 2*Ic3xx*q1d*q2d*cos(q2) + Ic3yy*q1d*q2d*cos(q2) + (Pc3x^2*m3*q2d^2*sin(2*q3))/2 - \\
& (Pc3y^2*m3*q2d^2*sin(2*q3))/2 - 2*Ic3xy*q1d^2*cos(q2)^2*cos(q3)^2 - \\
& Ic3yz*q1d^2*cos(q2)*cos(q3)*sin(q2) - Ic3xz*q1d^2*cos(q2)*sin(q2)*sin(q3) - \\
& 2*Pc3y^2*m3*q1d*q2d*cos(q2) - 2*Ic3xz*q1d*q2d*cos(q3)*sin(q2) + \\
& 2*Ic3yz*q1d*q2d*sin(q2)*sin(q3) + Ic3xx*q1d^2*cos(q2)^2*cos(q3)*sin(q3) - \\
& Ic3yy*q1d^2*cos(q2)^2*cos(q3)*sin(q3) + Pc3x*Pc3y*m3*q1d^2*cos(q2)^2 + \\
& 2*Pc3x*Pc3y*m3*q2d^2*cos(q3)^2 + 2*Ic3xx*q1d*q2d*cos(q2)*cos(q3)^2 - \\
& 2*Ic3yy*q1d*q2d*cos(q2)*cos(q3)^2 + 4*Ic3xy*q1d*q2d*cos(q2)*cos(q3)*sin(q3) - \\
& Pc3x^2*m3*q1d^2*cos(q2)^2*cos(q3)*sin(q3) + \\
& Pc3y^2*m3*q1d^2*cos(q2)^2*cos(q3)*sin(q3) - 2*Pc3x^2*m3*q1d*q2d*cos(q2)*cos(q3)^2 + \\
& 2*Pc3y^2*m3*q1d*q2d*cos(q2)*cos(q3)^2 - 2*Pc3x*Pc3y*m3*q1d^2*cos(q2)^2*cos(q3)^2 - \\
& 2*Pc3x*Pc3z*m3*q1d*q2d*cos(q3)*sin(q2) + 2*Pc3y*Pc3z*m3*q1d*q2d*sin(q2)*sin(q3) - \\
& Pc3y*Pc3z*m3*q1d^2*cos(q2)*cos(q3)*sin(q2) - \\
& Pc3x*Pc3z*m3*q1d^2*cos(q2)*sin(q2)*sin(q3) + \\
& 4*Pc3x*Pc3y*m3*q1d*q2d*cos(q2)*cos(q3)*sin(q3)
\end{aligned}$$



**G(1,1) =**

$$-g*(Pc2z*m2*\sin(q1) - Pc1y*m1*\sin(q1) + Pc1x*m1*\cos(q1) + Pc2y*m2*\cos(q1)*\cos(q2) - Pc3z*m3*\cos(q1)*\cos(q2) + Pc2x*m2*\cos(q1)*\sin(q2) + Pc3y*m3*\cos(q3)*\sin(q1) + Pc3x*m3*\sin(q1)*\sin(q3) + Pc3x*m3*\cos(q1)*\cos(q3)*\sin(q2) - Pc3y*m3*\cos(q1)*\sin(q2)*\sin(q3))$$

**G(2,1) =**

$$-g*\sin(q1)*(Pc3z*m3*\sin(q2) - Pc2y*m2*\sin(q2) + Pc2x*m2*\cos(q2) + Pc3x*m3*\cos(q2)*\cos(q3) - Pc3y*m3*\cos(q2)*\sin(q3))$$

**G(3,1) =**

$$g*(Pc3x*m3*\cos(q1)*\cos(q3) - Pc3y*m3*\cos(q1)*\sin(q3) + Pc3y*m3*\cos(q3)*\sin(q1)*\sin(q2) + Pc3x*m3*\sin(q1)*\sin(q2)*\sin(q3))$$

## Bibliography

- [1] C. G. Rose, F. Sergi, Y. Yun, K. Madden, A. Deshpande, and M. K. O'Malley, "Characterization of a hand-wrist exoskeleton, readapt, via kinematic analysis of redundant pointing tasks," in *2015 IEEE International Conference on Rehabilitation Robotics (ICORR)*, pp. 205–210, Aug 2015.
- [2] J. J. Crisco, W. M. Heard, R. R. Rich, D. J. Paller, and S. W. Wolfe, "The mechanical axes of the wrist are oriented obliquely to the anatomical axes," *J Bone Joint Surg Am*, vol. 93, pp. 169–177, Jan 2011.
- [3] H. I. Krebs, N. Hogan, M. L. Aisen, and B. T. Volpe, "Robot-aided neurorehabilitation," *IEEE Transactions on Rehabilitation Engineering*, vol. 6, pp. 75–87, Mar 1998.
- [4] J. A. French, C. G. Rose, and M. K. OMalley, "System characterization of MAHI Exo-II: A robotic exoskeleton for upper extremity rehabilitation," in *ASME 2014 Dynamic Systems and Control Conference*, American Society of Mechanical Engineers, 2014.
- [5] A. U. Pehlivan, F. Sergi, A. Erwin, N. Yozbatiran, G. E. Francisco, and M. K. O. Malley, "Design and validation of the ricewrist-s exoskeleton for robotic rehabilitation after incomplete spinal cord injury," *Robotica*, vol. 32, pp. 1415–1431, 12 2014.
- [6] J. A. Martinez, P. Ng, S. Lu, M. S. Campagna, and O. Celik, "Design of wrist

- gimbal: A forearm and wrist exoskeleton for stroke rehabilitation,” in *2013 IEEE 13th International Conference on Rehabilitation Robotics (ICORR)*, pp. 1–6, June 2013.
- [7] L. Cappello, S. Contu, N. Elangovan, S. Khosravani, J. Konczak, and L. Masia, “Evaluation of wrist joint proprioception by means of a robotic device,” in *2014 11th International Conference on Ubiquitous Robots and Ambient Intelligence (URAI)*, pp. 531–534, Nov 2014.
- [8] A. U. Pehlivan, C. Rose, and M. K. O’Malley, “System characterization of ricewrist-s: A forearm-wrist exoskeleton for upper extremity rehabilitation,” in *2013 IEEE 13th International Conference on Rehabilitation Robotics (ICORR)*, pp. 1–6, June 2013.
- [9] D. Mozaffarian *et al.*, “Heart disease and stroke statistics—2016 update,” *Circulation*, 2015.
- [10] M. Berkowitz, *Spinal cord injury: An analysis of medical and social costs*. 1998.
- [11] J. Steeves, D. Lammertse, A. Curt, J. Fawcett, M. Tuszynski, J. Ditunno, P. Ellaway, M. Fehlings, J. Guest, N. Kleitman, P. Bartlett, A. Blight, A. Blight, V. Dietz, B. Dobkin, R. Grossman, D. Short, M. Nakamura, W. Coleman, M. Gavoria, and A. Privat, “Guidelines for the conduct of clinical trials for spinal cord injury (sci) as developed by the iccp panel: clinical trial outcome measures,” *SPINAL CORD*, vol. 45, pp. 206–221, 2007.
- [12] R. Riener, T. Nef, and G. Colombo, “Robot-aided neurorehabilitation of the upper extremities,” *Medical and Biological Engineering and Computing*, vol. 43, no. 1, pp. 2–10, 2005.

- [13] C. Bütefisch *et al.*, “Repetitive training of isolated movements improves the outcome of motor rehabilitation of the centrally paretic hand,” *Journal of the Neurological Sciences*, vol. 130, no. 1, pp. 59–68, 1995.
- [14] T. Nef, M. Mihelj, G. Kiefer, C. Perndl, R. Muller, and R. Riener, “Armin - exoskeleton for arm therapy in stroke patients,” in *2007 IEEE 10th International Conference on Rehabilitation Robotics*, pp. 68–74, June 2007.
- [15] D. J. Reinkensmeyer, L. E. Kahn, M. Averbuch, A. McKenna-Cole, B. D. Schmit, and W. Z. Rymer, “Understanding and treating arm movement impairment after chronic brain injury: Progress with the ARM guide,” *J. of Rehabil. Res. Dev.*, vol. 37, no. 6, pp. 653–662, 2000.
- [16] S. K. Charles, H. I. Krebs, B. T. Volpe, D. Lynch, and N. Hogan, “Wrist rehabilitation following stroke: initial clinical results,” in *9th International Conference on Rehabilitation Robotics, 2005. ICORR 2005.*, pp. 13–16, June 2005.
- [17] N. Yozbatiran, J. Berliner, C. Boake, M. O’Malley, Z. Kadivar, and G. Francisco, “Robotic training and clinical assessment of forearm and wrist movements after incomplete spinal cord injury: A case study,” in *Rehabilitation Robotics (ICORR), 2011 IEEE International Conference on*, pp. 1–4, IEEE, 2011.
- [18] N. Yozbatiran, J. Berliner, M. O’Malley, A. Pehlivan, Z. Kadivar, C. Boake, and G. E. Francisco, “Robotic training and clinical assessment of upper extremity movements after spinal cord injury; a single case report,” *Journal of Rehabilitation Medicine*, vol. 44, pp. 186–188, 01/2012 2012.
- [19] A. A. Blank, J. A. French, A. U. Pehlivan, and M. K. OMalley, “Current trends in robot-assisted upper-limb stroke rehabilitation: promoting patient engagement

- in therapy,” *Current Physical Medicine and Rehabilitation Reports*, vol. 2, no. 3, pp. 184–195, 2014.
- [20] A. Lo, P. Guarino, L. Richards, J. Haselkorn, G. Wittenberg, D. Federman, R. Ringer, T. Wagner, H. Krebs, B. Volpe, *et al.*, “Robot-assisted therapy for long-term upper-limb impairment after stroke,” *New England Journal of Medicine*, vol. 362, no. 19, pp. 1772–1783, 2010.
- [21] P. Lum, C. Burgar, M. Van der Loos, P. Shor, M. Majmundar, and R. Yap, “The mime robotic system for upper-limb neuro-rehabilitation: Results from a clinical trial in subacute stroke,” in *Rehabilitation Robotics, 2005. ICORR 2005. 9th International Conference on*, pp. 511–514, IEEE, 2005.
- [22] P. S. Lum, S. Godfrey, E. Brokaw, R. Holley, and D. Nichols, “Robotic approaches for rehabilitation of hand function after stroke,” *American J. of Physical Medicine & Rehabilitation*, vol. 91, no. 11, pp. S242–S254, 2012.
- [23] H. Krebs, B. T. Volpe, D. Williams, J. Celestino, S. K. Charles, D. Lynch, and N. Hogan, “Robot-aided neurorehabilitation: a robot for wrist rehabilitation,” *IEEE Transactions on Neural Systems and Rehabilitation Engineering*, vol. 15, pp. 327–35, Sept. 2007.
- [24] P. S. Lum, C. G. Burgar, M. V. D. Loos, P. C. Shor, M. Majmundar, and R. Yap, “MIME robotic device for upper-limb neurorehabilitation in subacute stroke subjects: A follow-up study,” *The Journal of Rehabilitation Research and Development*, vol. 43, no. 5, p. 631, 2006.
- [25] J. C. Perry, J. Rosen, and S. Burns, “Upper-limb powered exoskeleton design,” *IEEE/ASME Transactions on Mechatronics*, vol. 12, pp. 408–417, Aug 2007.

- [26] T. G. Sugar, J. He, E. J. Koeneman, J. B. Koeneman, R. Herman, H. Huang, R. S. Schultz, D. E. Herring, J. Wanberg, S. Balasubramanian, P. Swenson, and J. A. Ward, "Design and control of rupert: A device for robotic upper extremity repetitive therapy," *IEEE Transactions on Neural Systems and Rehabilitation Engineering*, vol. 15, pp. 336–346, Sept 2007.
- [27] A. U. Pehlivan, A. Pehlivan, O. Celik, and M. O'Malley, "Mechanical design of a distal arm exoskeleton for stroke and spinal cord injury rehabilitation," in *2011 IEEE International Conference on Rehabilitation Robotics*, pp. 1–5, June 2011.
- [28] M. K. O'Malley, A. Sledd, A. Gupta, V. Patoglu, J. Huegel, and C. Burgar, "The RiceWrist: a distal upper extremity rehabilitation robot for stroke therapy," in *Proceedings of IMECE 2006*, (Chicago, IL, USA), November 2006.
- [29] A. Gupta, M. K. O'Malley, V. Patoglu, and C. Burgar, "Design, control and performance of ricewrist: A force feedback wrist exoskeleton for rehabilitation and training," *The International Journal of Robotics Research*, vol. 27, no. 2, pp. 233–251, 2008.
- [30] A. U. Pehlivan, S. Lee, and M. K. O'Malley, "Mechanical design of ricewrist-s: A forearm-wrist exoskeleton for stroke and spinal cord injury rehabilitation," in *2012 4th IEEE RAS EMBS International Conference on Biomedical Robotics and Biomechatronics (BioRob)*, pp. 1573–1578, June 2012.
- [31] C. D. Takahashi, L. Der-Yeghiaian, V. Le, R. R. Motiwala, and S. C. Cramer, "Robot-based hand motor therapy after stroke," *Brain*, vol. 131, no. 2, p. 425, 2008.
- [32] P. Maciejasz, J. Eschweiler, K. Gerlach-Hahn, A. Jansen-Troy, and S. Leonhardt,

- “A survey on robotic devices for upper limb rehabilitation,” *Journal of NeuroEngineering and Rehabilitation*, vol. 11, no. 1, p. 3, 2014.
- [33] C. N. Schabowsky, S. B. Godfrey, R. J. Holley, and P. S. Lum, “Development and pilot testing of HEXORR: Hand EXOskeleton Rehabilitation Robot,” *Journal of Neuroengineering and Rehabilitation*, vol. 7, no. 36, pp. 1–16, 2010.
- [34] M. Bouzit, G. Burdea, G. Popescu, and R. Boian, “The Rutgers Master II-new design force-feedback glove,” *Mechatronics, IEEE/ASME Transactions on*, vol. 7, no. 2, pp. 256–263, 2002.
- [35] M. Cempini, M. Cortese, and N. Vitiello, “A Powered Finger-Thumb Wearable Hand Exoskeleton With Self-Aligning Joint Axes,” *IEEE/ASME Trans. on Mechatronics*, 2014. Early Access Online DOI: 10.1109/TMECH.2014.2315528.
- [36] A. Chiri, F. Giovacchini, N. Vitiello, E. Cattin, S. Roccella, F. Vecchi, and M. Carrozza, “HANDEXOS: Towards an exoskeleton device for the rehabilitation of the hand,” in *IEEE/RSJ International Conference on Intelligent Robots and Systems, 2009. IROS*, pp. 1106–1111, Oct. 2009.
- [37] H. Kawasaki, S. Ito, Y. Ishigure, Y. Nishimoto, T. Aoki, T. Mouri, H. Sakaeda, and M. Abe, “Development of a Hand Motion Assist Robot for Rehabilitation Therapy by Patient Self-Motion Control,” in *IEEE International Conference on Rehabilitation Robotics, ICORR*, pp. 234–240, 2007.
- [38] Z.-M. Li, “The influence of wrist position on individual finger forces during forceful grip,” *The J. of Hand Surgery*, vol. 27, no. 5, pp. 886–896, 2002.
- [39] A. D. Deshpande, N. Gialias, and Y. Matsuoka, “Contributions of intrinsic viscoelastic torques during planar index finger and wrist movements,” *Biomedical*

- Engineering, IEEE Transactions on*, vol. 59, no. 2, pp. 586–594, 2012.
- [40] P.-H. Kuo and A. D. Deshpande, “Contribution of passive properties of muscle-tendon units to the metacarpophalangeal joint torque of the index finger,” in *Biomedical Robotics and Biomechatronics (BioRob), IEEE RAS and EMBS Intl. Conf. on*, pp. 288–294, 2010.
- [41] J. S. Knutson, K. L. Kilgore, J. M. Mansour, and P. E. Crago, “Intrinsic and extrinsic contributions to the passive moment at the metacarpophalangeal joint,” *Journal of Biomechanics*, vol. 33, no. 12, pp. 1675–1681, 2000.
- [42] A. Esteki and J. Mansour, “An experimentally based nonlinear viscoelastic model of joint passive moment,” *Journal of Biomechanics*, vol. 29, no. 4, pp. 443–450, 1996.
- [43] A. Schiele and F. C. T. van der Helm, “Kinematic design to improve ergonomics in human machine interaction,” *IEEE Transactions on Neural Systems and Rehabilitation Engineering*, vol. 14, no. 4, pp. 456–469, 2006.
- [44] M. Esmaeili, K. Gamage, E. Tan, and D. Campolo, “Ergonomic considerations for anthropomorphic wrist exoskeletons: a simulation study on the effects of joint misalignment,” in *Intelligent Robots and Systems (IROS), 2011 IEEE/RSJ International Conference on*, pp. 4905–4910, IEEE, 2011.
- [45] V. Hayward and K. E. MacLean, “Do it yourself haptics: part I,” *Robotics & Automation Mag., IEEE*, vol. 14, no. 4, pp. 88–104, 2007.
- [46] A. U. Pehlivan, F. Sergi, and M. K. O’Malley, “A subject-adaptive controller for wrist robotic rehabilitation,” *IEEE/ASME Trans. Mechatronics*, vol. 20, no. 3, pp. 1338–1350, 2015.



- [47] P. Y. Y. Agarwal, J. Fox, K. Madden, and A. D. Deshpande, “Design, control and testing of a thumb exoskeleton with series elastic actuation,” *International Journal of Robotics Research*, 2017 *in press*.
- [48] K. D. Fitle, A. U. Pehlivan, and M. K. O’Malley, “A robotic exoskeleton for rehabilitation and assessment of the upper limb following incomplete spinal cord injury,” in *2015 IEEE International Conference on Robotics and Automation (ICRA)*, pp. 4960–4966, May 2015.
- [49] J. Gordon, M.-F. Ghilardi, S. E. Cooper, and C. Ghez, “Accuracy of planar reaching movements. II. Systematic extent errors resulting from inertial anisotropy,” *Exp. Brain Res.*, vol. 99, no. 1, pp. 112–130, 1993.
- [50] T. Flash and N. Hogan, “The coordination of arm movements: An experimentally confirmed mathematical model,” *J. Neurosci.*, vol. 5, no. 7, pp. 1688–1703, 1985.
- [51] P. Morasso, “Spatial control of arm movements,” *Exp. Brain Res.*, vol. 42, no. 2, pp. 223–227, 1981.
- [52] A. Erwin, E. Pezent, J. Bradley, and M. K. O’Malley, “The effect of robot dynamics on the smoothness of wrist pointing movements,” in *IEEE Int. Conf. Rehab. Robot. (ICORR)*, Submitted: 2017.
- [53] C. G. Rose, C. K. Kann, A. D. Deshpande, and M. K. O’Malley, “Estimating anatomical wrist joint motion with a robotic exoskeleton,” in *IEEE Int. Conf. Rehab. Robot. (ICORR)*, Submitted: 2017.
- [54] E. Pezent, C. G. Rose, A. D. Deshpande, and M. K. O’Malley, “Design and characterization of the OpenWrist: A robotic wrist exoskeleton for coordinated

- hand-wrist rehabilitation,” in *IEEE Int. Conf. Rehab. Robot. (ICORR)*, Submitted: 2017.
- [55] J. J. Craig, *Introduction to Robotics: Mechanics and Control (3rd Edition)*. Pearson, 2004.
- [56] H. Lipkin, “A note on denavit-hartenberg notation in robotics,” in *29th Mechanisms and Robotics Conference*, American Society of Mechanical Engineers, 2005.
- [57] C. G. Rose, “Hardware- versus human-centric assessment of rehabilitation robots,” Master’s thesis, Rice University, 2015.
- [58] J. W. Liang and B. F. Feeny, “Identifying coulomb and viscous friction from free-vibration decrements,” *Nonlinear Dynamics*, vol. 16, no. 4, pp. 337–347, 1998.
- [59] J. R. Celestino, “Characterization and control of a robot for wrist rehabilitation,” Master’s thesis, Massachusetts Institute of Technology, 2003.
- [60] M. Schroeder, “Synthesis of low-peak-factor signals and binary sequences with low autocorrelation (corresp.),” *IEEE Trans. Inf. Theor.*, vol. 16, pp. 85–89, Sept. 2006.
- [61] T. L. Brooks, “Telerobotic response requirements,” in *1990 IEEE International Conference on Systems, Man, and Cybernetics Conference Proceedings*, pp. 113–120, Ieee, 1990.
- [62] L. Vaisman, L. Dipietro, and H. I. Krebs, “A comparative analysis of speed profile models for wrist pointing movements,” *IEEE Trans. Neural Sys. Rehab.*

- Eng.*, vol. 21, no. 5, pp. 756–766, 2013.
- [63] E. Biryukova, A. Roby-Brami, A. Frolov, and M. Mokhtari, “Kinematics of human arm reconstructed from spatial tracking system recordings,” *Journal of biomechanics*, vol. 33, no. 8, pp. 985–995, 2000.
- [64] R. W. Schafer, “What is a Savitzky-Golay filter?[lecture notes],” *Signal Processing Magazine, IEEE*, vol. 28, no. 4, pp. 111–117, 2011.
- [65] O. Celik, M. K. O’Malley, C. Boake, H. S. Levin, N. Yozbatiran, and T. A. Reistetter, “Normalized movement quality measures for therapeutic robots strongly correlate with clinical motor impairment measures,” *IEEE Transactions on Neural Systems and Rehabilitation Engineering*, vol. 18, no. 4, pp. 433–444, 2010.
- [66] S. Balasubramanian, A. Melendez-Calderon, and E. Burdet, “A robust and sensitive metric for quantifying movement smoothness,” *IEEE Transactions on Biomedical Engineering*, vol. 59, pp. 2126–2136, Aug 2012.
- [67] R. Stein, F. Cody, and C. Capaday, “The trajectory of human wrist movements,” *J. Neurophys.*, vol. 59, no. 6, pp. 1814–1830, 1988.
- [68] N. L. Tagliamonte, M. Scorcio, D. Formica, D. Campolo, and E. Guglielmelli, “Effects of impedance reduction of a robot for wrist rehabilitation on human motor strategies in healthy subjects during pointing tasks,” *Advanced Robotics*, vol. 25, no. 5, pp. 537–562, 2011.
- [69] N. Colonnese and A. Okamura, “M-width: Stability and accuracy of haptic rendering of virtual mass,” *Robotics*, vol. 41, 2013.